Spinal Cord Diffusion Imaging

Imaging Challenges and Prognostic Value

Torben Schneider

A dissertation submitted in partial fullfillment of the requirements for the degree of

Doctor of Philosophy

of the

University College London

Department of Neuroinflammation
UCL Institute of Neurology

Declaration

I, Torben Schneider confirm that the work presented in this thesis is my own. Where information has been derived from other sources, I confirm that this has been indicated in the thesis.

London, United Kingdom, 12th December 2012

Torben Schneider, 12th December 2012

Abstract

The aim of this thesis is to explore the potential of quantitative imaging markers derived from diffusion-weighted MRI (DW MRI) in the spinal cord to characterise healthy white matter pathways and provide sensitivity to axonal damage, regeneration and collateral sprouting in spinal cord disease.

With new innovative treatment strategies emerging for spinal cord pathologies such as spinal cord injury and Multiple Sclerosis, there is a need for new *in-vivo* biomarkers that can be specific to structural and functional changes and their underlying mechanisms on a microscopic scale. DW MRI has the potential to quantifying those microstructural characteristics beyond the scale of conventional MRI.

In the first part of this dissertation I investigate Diffusion Tensor Imaging (DTI), which is the most established DW MRI analysis technique in clinical practice. In two studies we assess DTI in the context of spinal cord imaging. In the first experiment I show that DTI is sensitive to the presence of collateral fibres, e.g., at inter-vertebral level where peripheral nerves enter the spinal tract. In the second experiment I propose a new method for reducing partial volume effects on whole cord DTI measurements, which is specifically tailored for the imaging and analysis challenges in the cord.

The second part of this thesis comprises two studies of q-space imaging (QSI) in healthy controls. In theory, QSI offers a more comprehensive description of the diffusion process, but is challenging to set up on a clinical MRI scanner. I present here two QSI protocols, set up for two different scanners with different gradient hardware, receive coils and software limitations. For the first time we perform a systematic study of QSI that assesses the reproducibility and specificity to different white pathways *in-vivo* in the cervical cord within a group of healthy volunteers. Both studies show superior reproducibility of QSI over conventional analysis, although the results of using QSI parameters to distinguish individual white matter tracts in the cord were inconclusive.

The third part of this thesis describes a new imaging method protocol based on the ActiveAx optimisation framework. It uses a complex multi-compartment model, which relates DW MRI data to microstructural parameters like axon diameter and density. I design a new orientation aware method based ActiveAx, which incorporates the known fibre structure of the spinal cord. In a first step I validate the approach in in a post-mortem cervical spinal cord sample of a velveteen monkey. I then demonstrate clinical feasibility and good reproducibility of the new protocol for *in-vivo* human studies, using the corpus callosum as a preliminary model system for structures with unidirectional fibre architecture. Finally I present first estimation results of axon diameter and density of the cervical spinal cord *in-vivo* in a healthy control that agree with the findings in the *ex-vivo* monkey spinal cord sample.

Es ist nicht genug, zu wissen, man muß auch anwenden;
es ist nicht genug, zu wollen, man muß auch tun.

— Johann Wolfgang von Goethe

Acknowledgements

Firstly, I would like to express my immense gratitude to my supervisors Claudia Wheeler-Kingshott and Daniel Alexander who gave me the opportunity to study with two of the world-leading research groups. Both have been the best supervisors anyone could wish for. I'm very grateful for all the guidance and help I received from them throughout my PhD and I consider myself both very lucky and very honoured, being their student. I'm also very gratefully towards the International Spinal Research Trust who funded this PhD project.

Furthermore, I would like to thank Dr. Patrick Freund, not only for the fruitful collaboration, but also for being a great friend and motivator. I also wish to express my sincere thanks to David Thomas, Olga Ciccarelli and Carolina Kachramanoglou for providing me with data to work with after our 1.5T scanner had broken down and the new 3T scanner was not installed yet. Many thanks also to Tim Dyrby and Henrik Lundell for inviting me to Denmark and giving me the opportunity to test my protocols on their scanner and samples.

I would like to thank my friend Laura Panagiotaki for her constant support and valuable help in all the aspects of PhD life. I would also like to thank Gemma Nedjati-Gilani for all her advice and support. Many thanks also to Bhavana Solanky and Becky Samson for being great office mates, having been often the only human contacts to the outside world, particularly when another ISMRM deadline was near.

I also would like to thank all the people in the Microstructure Imaging Group and the Department of Neuroinflammation all the support, but also for being great company in and out of the office.

A very special thanks goes to my dear friends Franziska Teichert and Frank Penczek for being always there for me for a BBQ or the occasional German fire punch. Finally, I would like to express my deepest gratitude to my loving parents Birgit and Jürgen. I'm infinitely grateful for their encouragement and continuous support for all my life. Last, but not least, I thank Chrystèle for joining me on all the way since I arrived in England and for being such a wonderful and inspiring influence on my life ever since.

Contents

List of Figures

List of Tables

Acronyms

Δ	diffusion time
δ	diffusion gradient pulse duration
λ_1	axial diffusivity
$\vec{g}$	diffusion gradient direction
$\|G\|$	diffusion gradient strength
AD	axial diffusivity
ADC	apparent diffusion coefficient
CC	corpus callosum
CHARMED	Composite Hindered and Restricted Model of Diffusion
CNS	central nervous system
COM	centre-of-mass
COV	coefficient of variation
CPMG	Carr-Purcell-Meiboom-Gill
CRLB	Cramer-Rao lower bound
CSF	cerebro-spinal fluid
CST	corticospinal tract
dPDF	diffusion probability density function
dPGSE	double refocussed pulsed gradient spin echo
DT	Diffusion Tensor
DTI	Diffusion Tensor Imaging
DWI	Diffusion Weighted Imaging
EC	extra-cellular
EPI	Echo-Planar Imaging
FA	fractional anisotropy

FID . . . . . Free Induction Decay

FIM . . . . . Fisher information matrix (FIM)

FLAIR . . . . . fluid-attenuated inversion recovery

FOV . . . . . field-of-view

FWHM . . . . . full width of half maximum

GM . . . . . gray matter

GPD . . . . . Gaussian phase distribution

HARDI . . . . . high-angular-diffusion-imaging

IC . . . . . intra-cellular

ICC . . . . . intraclass correlation coefficient

MAD . . . . . mean axon diameter

MC . . . . . Monte Carlo

MCMC . . . . . Markov chain Monte Carlo

MD . . . . . mean diffusivity

MMWMD . . . . . minimal model of white matter diffusion

MRI . . . . . Magnetic Resonance Imaging

MS . . . . . Multiple Sclerosis

NMO . . . . . neuromyelitis optica

NMR . . . . . Nuclear Magnetic Resonance

OI . . . . . orientation invariant

PGSE . . . . . pulsed gradient spin echo

PNS . . . . . peripheral nerve stimulation

PVA . . . . . partial volume average

QSI . . . . . **q**-space imaging

RD . . . . . radial diffusivity

RF . . . . . radio-frequency

RMSD . . . . . root-mean-squared-displacement

ROI . . . . . region of interest

SC . . . . . spinal cord

SCA . . . . . spinal cord area

SCI . . . . . spinal cord injury

SE . . . . . spin echo

SF . . . . . single fibre

SGP . . . . . short gradient pulse

SNR . . . . . signal-to-noise ratio

T2w T2-weighted

TE . . . . . echo time

TR . . . . . repetition time

WM . . . . . white matter

ZOOM . . . . . Zonally oblique multislice

1

Introduction

The spinal cord is a vital part of the human central nervous system (CNS), relaying information to and from the brain and controlling the motor function in the rest of the body. Damage to the spinal cord tissue will compromise signal transmission and can cause severe neurological symptoms, often resulting in a loss of mobility or feeling. Spinal cord injury (SCI) is often caused by trauma, i.e. a mechanical injury of the cord tissue during an accident, a fall, etc. However, SCI can also have non-traumatic causes such as tumours, infectious diseases or degenerative pathologies of the CNS, like Multiple Sclerosis (MS).

The introduction of Magnetic Resonance Imaging (MRI) to the clinical practise has vastly improved the diagnosis and treatment monitoring of SCI as it offers a non-invasive way to assess anatomical changes in the spinal cord after injury. While routine MRI scans are aiding the detection of macroscopic changes in the cord, they have a limited prognostic value because of their qualitative nature and because of their lack of specificity in terms of underlying microstructure changes.

The sensitivity of Diffusion Weighted Imaging (DWI) to the diffusion of water molecules in the tissue in vivo has been exploited for more than 20 years to characterise the white matter tissue structure of the brain. Thanks to technological advances such as multi-channel coils for parallel imaging methods and 3T scanners, the past couple of years have made the application of DWI in the SC more feasible. As a result, diffusion imaging techniques are emerging as useful clinical methods for visualization and quantification of spinal cord damage. Despite encouraging initial results, much work still needs to be done to bring DWI in the cord to clinical practise. Specifically there is the need for *in-vivo* imaging biomarkers for human SC examinations, which are sensitive to underlying tissue changes and which are capable of quantifying structural and functional pathologies.

1.1 Problem statement

Despite some development work on DWI for SC, the following problems remain unresolved:

1. Current state-of-the-art DWI analysis methods, such as Diffusion Tensor Imaging (DTI), are unspecific to individual microstructural changes and therefore only have limited value in the evaluation of treatment and recovery in spinal cord pathology. Research on more advanced DWI techniques usually focusses only on brain imaging and is often not directly applicable to the SC in the same manner.

2. DWI acquisition itself is well established in the brain, but much less so in the SC. The SC is a more challenging structure to study because of several problems: the breathing motion, the artefacts arising from the surrounding bones, the pulsation of the cerebro-spinal fluid (CSF) and last but not least its limited size that requires high resolution.

The key motivation of this work is to overcome the challenges listed above by optimising the whole process from the acquisition design to the analysis methods, based on known SC tissue properties and to develop imaging biomarkers that can provide insight in underlying mechanisms of tissue damage and functional recovery.

1.2 Aims

1. Investigate existing DWI methods and identify suitable metrics for SC characterisation.
2. Optimise existing acquisition protocols and analysis methods to improve sensitivity to SC pathologies.
3. Design new DWI imaging protocols and white matter models and derive new imaging biomarkers specifically for a better quantification of SC microstructure properties.

1.3 Summary of contributions

The work presented in this dissertation is divided in three parts, comprising 8 different experiments in total. Each part contributes towards the aims described above as follows:

Part I shows two studies that use the clinically established DTI method.

Chapter 3 devises a novel imaging protocol to visualise and quantify the presence of collateral sprouting fibres at different levels of the SC. This experiment contributes towards project aims 1 and 2 as we investigate two different DWI metrics from existing literature and focus on the optimisation of the acquisition protocol.

In Chapter 4 we develop a novel post-processing method to cope with partial volume effects on average whole cord area DTI metrics. This experiment contribute towards project aim 2, as we aim to improve reliability and reduce inter-subject variability for DTI acquisitions and measurements that are widely used in clinical studies.

Part II presents two studies which implement the less commonly used **q**-space imaging (QSI) method in the cord. The aim is to test whether is is possible to distinguish different parts of the healthy human cord by their QSI parameters. The two experiments contributes towards project aim 1 as they

test the use of QSI metrics for the investigation of SC microstructure. The experiments also contribute to project aim 3 as they look for the first time into QSI parallel to the major fibre direction as an additional imaging marker.

Chapter 5 presents data that was analysed retroactively on already acquired QSI-data. This dataset data revealed interesting results, but was put into question by technical limitations of the acquisition and analysis method.

Chapter 6 presents our efforts to reproduce the results of Chapter 5 on our newly installed 3T scanner, which allowed us more control over the scan parameters than before.

Part III shows our work towards project aim 3 by developing DWI protocols that allow direct estimation of axon diameter and density of SC white matter tissue. We present a new method (SF) as an extension of the "ActiveImaging" framework initially proposed by Alexander [3], which we modify to be able to exploit the characteristic a-priori known single major fibre orientation in structures like the SC. To aid the initial development we use in some experiments the corpus callosum as a model system of highly coherent white matter structures, similar to the SC organisation.

Chapter 7 presents a first implementation of the SF method. We use synthetic dataset from computer simulations to evaluate our method and compare it with Alexander's original method. Furthermore we show results of a first real-world implementation of our method applied to *ex-vivo* monkey spinal cord.

Chapter 8 introduces several improvements to our first SF implementation and presents a first implementation of the SF method *in-vivo* on a standard clinical scanner on two healthy volunteers.

Chapter 9 brings together our efforts to improve image quality and DWI acquisition protocols. We devise a novel imaging and analysis pipeline for SF-ActiveImaging and assess its scan/rescan reproducibility in the human corpus-callosum. Furthermore, we also present a first application of SF to healthy *in-vivo* human cord in one subject.

2

Background

2.1 Anatomy of the spinal cord

This section will give a brief overview of the macroscopic and microscopic organisation of the spinal cord (SC) (see [30, 66, 156] for more details).

The SC is the part of the central nervous system (CNS) that connects the brain and peripheral nervous system. It controls the voluntary movement of limbs and trunk, receives sensory information from these regions and monitors and coordinates the internal organ function in the thorax, abdomen and pelvis.

The SC is divided into different segments, according to the surrounding vertebrae. The cervical cord is divided in 7 segments (C1–C7), followed by the thoracical, lumbar and sacral cord segments [66, 156].

The SC is protected by the vertebral column and is located inside the vertebral canal. In cross-section, the cord can be divided in two regions: (i) the peripheral region containing neuronal white matter tracts, and (ii) the grey, butterfly-shaped central region made up of nerve cell bodies (see Figure 2.1). This gray matter (GM) is centred around the central canal, containing cerebrospinal fluid (CSF).

2.1.1 Organisation of the spinal cord

The white matter (WM) of the SC consists mostly of longitudinally oriented axons and glial cells. White matter axons are organized hierarchically grouped in bundles, tracts and pathways. Bundles of neighbouring white matter axons that share similar features are called fibre bundles. A tract is formed by fibre bundles with same origin, course, termination and function. Multiple tracts with the same function form a pathway.

Ascending tracts

Figure 2.1 illustrates the location of the major ascending pathways in the SC. These sensory tracts, arise either from cells of spinal ganglia in the white matter of the SC or from intrinsic neurons within the gray matter that receive primary sensory input. The dorsal column holds the largest ascending tracts and are associated with tactile, pressure, and kinesthetic sense connecting with sensory areas of the cerebral cortex. Fibres of the spinothalamic tracts ascend in the lateral ventral part of the cord and convey signals related to pain and thermal sense. The anterior spinothalamic tract ascends more anteriorly in the SC; conveying impulses related to light touch. At brain level the two spinothalamic tracts tend to merge and cannot be distinguished as separate entities. Anterior and posterior spinocerebellar tracts are involved in automatic muscle tone reg-

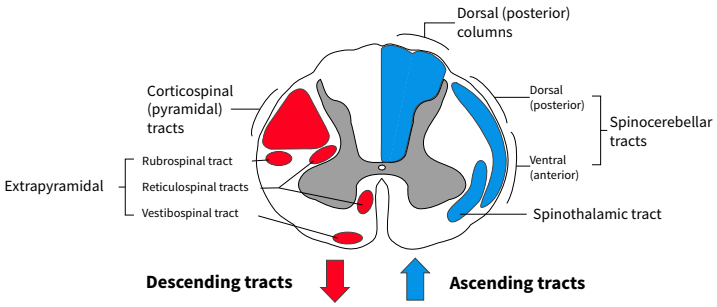

Figure 2.1: *Illustration of the major ascending and descending fibre pathways of the SC (adapted from* `http://en.wikipedia.org/wiki/Spinal_cord`*).*

ulation. These tracts ascend peripherally in the dorsal and ventral margins of the cord.

Descending tracts

Tracts descending to the SC as illustrated in Figure 2.1 are concerned with modulation of ascending sensory signals and are associated with voluntary motor function such as muscle tone and reflexes. The largest and most important, the corticospinal tract (CST), originates in broad regions of the cerebral cortex and descends in the lateral dorsal part of the SC white matter. Smaller descending tracts like the rubrospinal tract, the vestibulospinal tract, and the reticulospinal tract originate in small and diffuse regions of the midbrain, pons, and medulla and descend ventrally and laterally.

Microstructural organisation

A neural cell, or Neuron, possesses a cell body and two typically two types of extending structures: axons and dendrites. The dendrites carry afferent signals to the cell, while axons relay efferent signals. the typical size of the axon lies in the range of 1–10μm [20, 157]. Larger axons are usually surrounded by layers of myelin, which acts as an isolator for the electrical transmission of signals and allows for higher transmission speeds than unmyelinated axons. The structure of the axon is supported by longitudinal micro-filaments[20].

In the cord, the gray matter comprises the neuronal cell bodies and dendritic structures while the white matter mainly holds the axonal fibre bundles. The majority of white matter fibre bundles run parallel to the long axis of the cord. Peripheral nerves enter the spinal cord through the neuroanatomy, connecting to the gray matter[30].

2.2 Principles of MRI

Magnetic Resonance Imaging (MRI) is a non-invasive imaging method widely used in medicine. MRI is free of gamma-radiation (unlike e.g. X-ray methods), which makes it one of the major tools for application in neuroimaging. MRI can describe tissue in terms of many different properties such as relaxation,

density, and diffusion. Specifically, in this thesis our main interest is in the sensitivity of MRI to the motion of water molecules to infer information about the microscopic tissue morphology. A full account of MRI theory is beyond the scope of this chapter and can be found elsewhere [21, 102]. However, a brief overview about the principles of magnetic resonance and MRI is given below.

2.2.1 Magnetic resonance

Nuclear magnetic resonance is a phenomenon that occurs when an element with a non-zero magnetic moment (possessing an odd number of protons or neutrons) interacts with an external magnetic field. Hydrogen (^{1}H) is such an element, and is most commonly used in MRI due to its abundance in the human body. When such an element is placed in a magnetic field, its nuclear spin will begin to precess with a frequency governed by the equation:

$$\omega = \gamma \cdot \mathbf{B}_0 \tag{2.1}$$

where ω is the Larmor frequency, γ is the nucleus specific gyromagnetic ratio, and $\mathbf{B}_0$ is the magnetic field strength. In equilibrium, the nuclear spins rotate around the axis of the magnetic field $\mathbf{B}_0$ and their magnetic moment is aligned with the $\mathbf{B}_0$ field.

When a radio-frequency (RF) pulse is applied perpendicular to the $\mathbf{B}_0$ field, with a frequency equal to the Larmor frequency (i.e. the resonance frequency) the magnetic proton spins tilt towards the transverse plane and precess around the axis of the $\mathbf{B}_0$ field. The precession induces a voltage in the magnetic field of the receiver coil and produces a measurable signal. It is often more convenient present the nuclear spins in a reference frame rotating at the Larmor frequency ω about the $\mathbf{B}_0$ axis. In this rotating frame of reference, the bulk magnetisation is stationary and the RF pulse results in a tip from its equilibrium position toward the transverse plane by the angle α. A 90° pulse flips the magnetisation into the transverse plane and a 180° pulse inverts the bulk magnetisation.

Immediately after the excitation, the spins are completely in phase (coherent). After excitation, relaxation take place with a loss of phase coherence and a subsequent relaxation back to equilibrium. The signal induced in the receiver coil after excitation is referred to as the Free Induction Decay (FID) signal. Figure 2.2 illustrates the excitation and relaxation process.

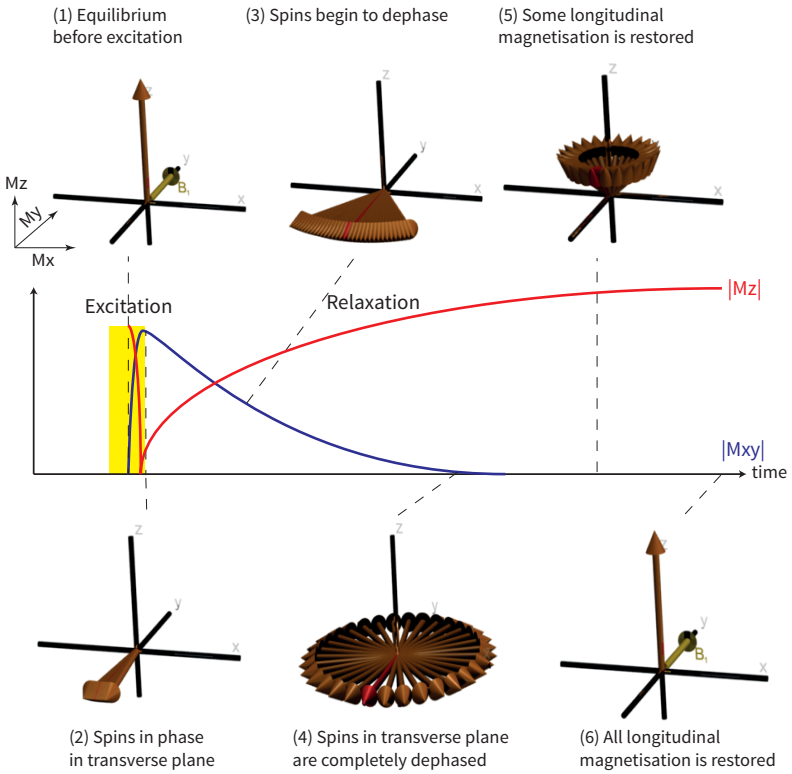

Figure 2.2: *Simplified illustration of spins during different steps of the FID signal formation after a 90° RF pulse is applied. Arrows represent the net magnetisation vectors of spin ensembles in the rotating frame of reference. Some figures were created using the SpinBench software [116].*

Together with the density of nuclear spins, the relevant time constants T1 and T2/T2* characterise the relaxation phenomena and are the principal source of contrast used in MRI. In the case of a 90° excitation pulse, these time constants are defined as below:

T1: is the longitudinal relaxation time, which describes how long it takes for the net magnetisation to return to the longitudinal equilibrium. Formally, the T1 constant relates to the longitudinal component of the magnetisation M_z at time t after 90° excitation by the formula:

$$M_z(t) = M_0 \cdot (1 - \exp(-t/T1)), \tag{2.2}$$

with M_0 being the total magnetisation, which is proportional to the total number of excited spins,

T2: is the transverse relaxation time, i.e. it describes the time it takes for the FID signal to decay due to randomly fluctuating internal magnetic fields caused by spin-spin interactions in the substance. This causes the spins to get out of phase and the transverse magnetization (and induced signal) is lost exponentially. Formally, the signal development of the transverse magnetisation $M_{xy}(t)$ at time t after 90° excitation is described by:

$$M_{xy}(t) = M_0 \cdot \exp(-t/T2), \tag{2.3}$$

In a non-ideal magnetic field, transverse magnetisation is also lost due to inhomogeneities in the $\mathbf{B}_0$ field, causing additional signal loss. In this case we distinguish between the T2 effect as the spin-spin interactions alone, and the T2* effect, as the signal loss due both spin-spin relaxation and $\mathbf{B}_0$ inhomogeneities.

The transverse magnetization decays more rapidly than it takes for the magnetisation to return to the longitudinal equilibrium. Both T1 and T2 are dependent on the magnetic field strength, but more importantly they are also specific to the macromolecular environment of the protons and therefore are specific for different types of tissue, e.g. for different tissue types within the live human brain (GM T1/T2 = 2000/100 ms, WM T1/T2 = 1100/70 ms at 3T magnetic field strength [140]).

2.2.2 Spin-echo sequence

The spin echo (SE) sequence is the central pulse sequence that is used in all experiments we present in this dissertation. Figure 2.3 illustrates the layout and signal development of the SE experiment. The SE sequence starts with a 90°(P90) excitation pulse that flips magnetization in the transverse plane, followed by a 180°RF pulse (P180) after time TE/2 and the signal readout after another TE/2, producing an echo at time TE. The P180 inversion pulse will reverse the demagnetization by field inhomogeneities so that the contrast is mainly driven by spin-spin relaxation constant T2 and the proton density M_0. When TR is sufficiently large for the longitudinal magnetisation to recover fully, the obtained signal is only dependent on proton density and on T2. When TE is chosen appropriately (i.e. usually in the range of tens of milliseconds for in-vivo head or cord images), the T2 signal decay is the main source of contrast the signal is called T2-weighted (T2w).

2.2.3 Gradients and Image formation

A magnetic gradient field $\mathbf{G}$ is a small spatially varying magnetic field, which is superimposed on the static magnetic field $\mathbf{B}_0$ and alters the spin frequency at a given position x as follows:

$$\omega(x) = \omega_0 + \gamma \cdot \mathbf{G}(x) \tag{2.4}$$

Gradient fields are fundamental to many aspects of MR, e.g., to generate a signal response (the so-called gradient echo) or to spatially encode the signal to allow the formation of an image, on which we concentrate here. Specifically we discuss here the 2D slice encoded SE imaging sequence, which combines the principles of spin-echo formation as demonstrated in Section 2.2.2 with spatial encoding gradients.

Figure 2.4 illustrates such a simple imaging SE pulse imaging sequence. First, the slice selection gradient $\mathbf{G}_{slice}$ is applied during the excitation RF pulse, which results in only the excitation of protons that precess with frequencies within the range of the excitation RF pulse.

The two gradients $\mathbf{G}_{read}$ and $\mathbf{G}_{phase}$ are orthogonal to $\mathbf{G}_{slice}$ and provide the spatial encoding within the excited slice. The phase encoding gradient $\mathbf{G}_{phase}$

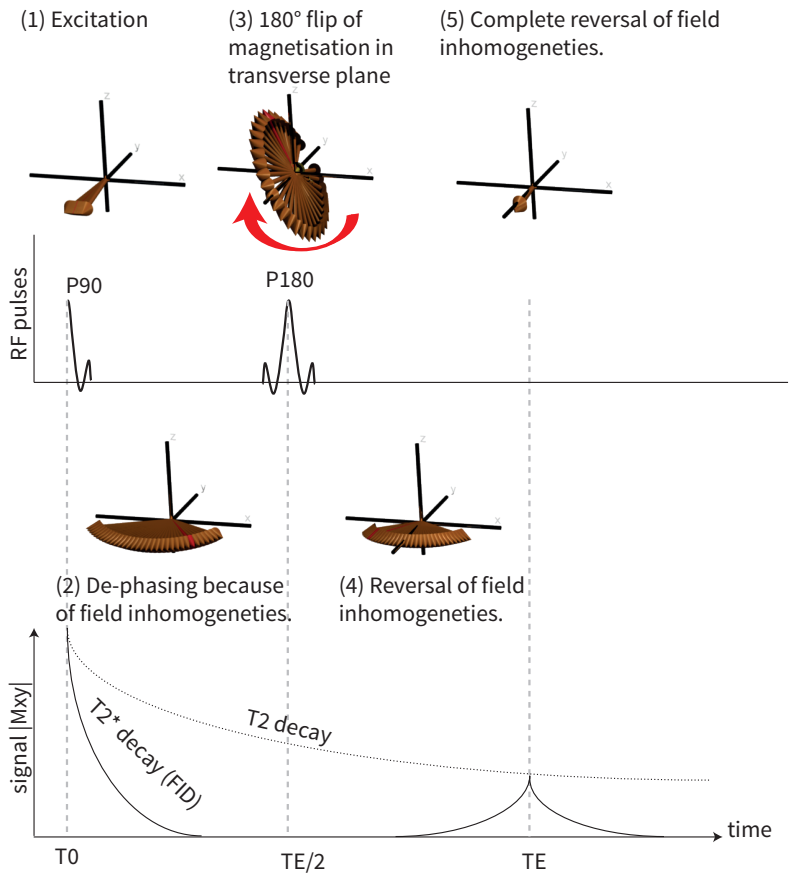

Figure 2.3: *Simplified illustration of spins during different steps of the FID signal formation after a 90° RF pulse is applied. Some figures were created using the SpinBench software [116].*

adds a phase shift to the spin frequency of the slice-selected magnetization, which encodes location in the direction. During the spin echo at TE, the $\mathbf{G}_{read}$ gradient is applied, making the resonant frequency of the nuclear magnetization vary with its location in the read-out direction. The signal is sampled k_x times (typically between 128 and 512 k_x samples are taken). After waiting the repetition time (TR) for the longitudinal magnetisation to restore, the whole sequence is repeated with a different phase-encoding gradient. After k_y phase encoding steps, the object of interest is completely spatially encoded by means of frequency and phase. Typically also between 128 and 512 k_y encoding steps are acquired. This 2-dimensional $k_x \times k_y$ frequency matrix is then reconstructed into an image using the Fourier Transform [94, 150].

In the sequence described above, each line of k-space is acquired individually, which makes the scan time per image impractical for larger k-space matrices. In clinical reality, the image preparation is often combined with fast imaging techniques that allow the acquisition of several lines of k-space at once[99, 141]. In clinical diffusion MRI, single-shot Echo-Planar Imaging (EPI) is by far the most common technique used for acquisition, as it allows acquisition of the full k-space matrix in one 'shot'.

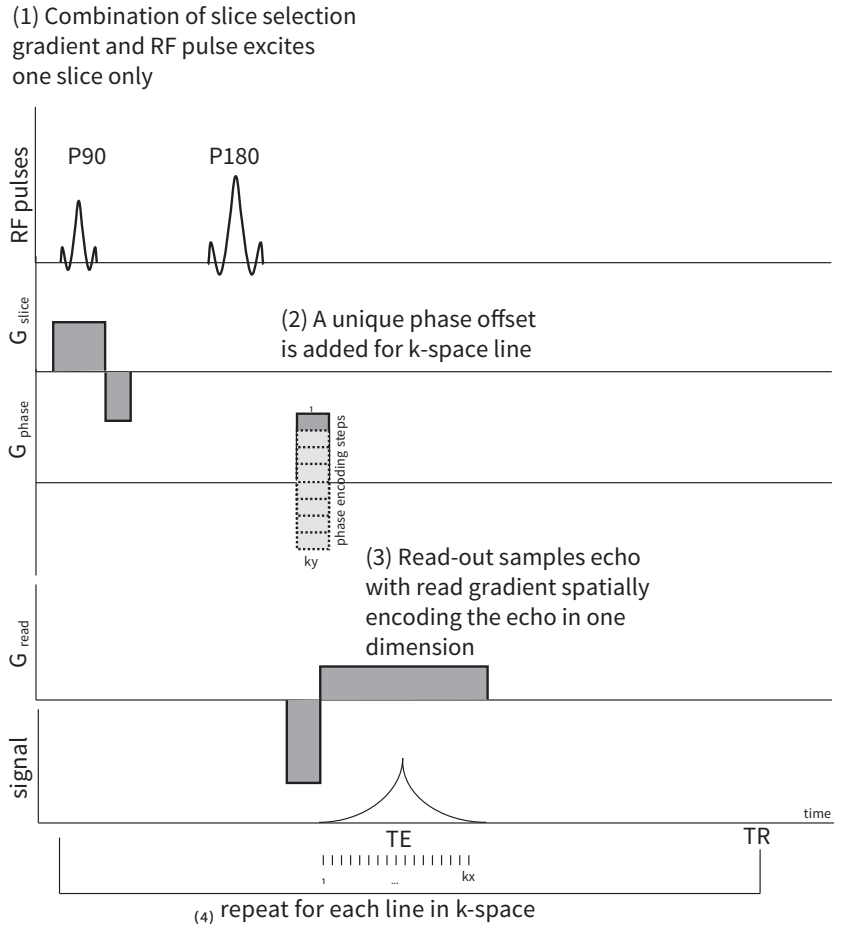

Figure 2.4: *Spatial encoding by different gradient pulses during a 2D spin echo sequence.*

2.2.4 Small field of view imaging

Imaging the spinal cord presents many challenges, mainly due to its small size and surrounding tissue like CSF and bone. On the other hand, to image the cord below the the neck, conventional imaging methods require a rather large field-of-view (FOV) to avoid aliasing artefacts [21, 102]. Small FOV methods allow to image a smaller volume and minimise the aliasing artefacts by avoiding to encode the surrounding tissue[52]. Such methods are well suited for the application to SC, as they reduce the necessary encoding steps and allow for the high spatial resolution that is required for imaging of the cord.

In this thesis we use a small FOV modification of the SE sequence called Zonally oblique multislice (ZOOM) imaging, which was introduced by Wheeler-Kingshott et al. [159], Wheeler-Kingshott et al. [160]. The central idea is to perform the encoding gradients for the excitation pulse P90 and refocussing pulse P180 at an angle α instead of parallel as in conventional SE. This way, only spins within the intersection of P90 and P180 are refocussed, effectively suppressing the unwanted signal outside the small FOV. A disadvantage of the technique is that, dependent on the applied angle α between P90

and P180, spins within the adjacent region of the FOV are also excited, which makes the continuous acquisition of adjacent slices within one TR difficult.

2.3 Principles of Diffusion MRI

Diffusion MRI captures the average diffusion of water molecules, which probes the structure of the biological tissue at scales much smaller than the imaging resolution. The diffusion of water molecules is Brownian under normal unhindered conditions, but in fibrous structures, such as white matter, water molecules tend to diffuse preferably along the fibers. Due to this physical phenomenon, diffusion MRI is able to obtain information about the neural architecture *in-vivo*. In the following section we will briefly review the principles of diffusion and its effect on the MRI signal.

2.3.1 Brownian motion

At a microscopic scale, water molecules freely move and collide with each other in a homogeneous medium according to Brownian motion [24]. At a macroscopic scale, this phenomenon yields a diffusion process. In the simplest case of pure molecular motion in the absence of any impeding barriers, the diffusion process can simply be characterised by the diffusion coefficient d [55]. In an isotropic and homogeneous medium, the mean displacement after a given time t is simply related to the diffusion coefficient d by Einstein's formula, which in 3-d space, is:

$$d = 6 \cdot \langle R^2 \rangle \cdot t \tag{2.5}$$

where, $\langle \dots \rangle$ denotes the ensemble average and $R = r - r_0$ is the displacement between the original position r_0 of a particle and the position r after the diffusion time t.

2.3.2 Free, hindered and restricted diffusion in biological tissue

In the simplest case, free diffusion (or unrestricted diffusion) is exactly described by the pure Brownian motion of water, i.e. molecules diffusing freely in all directions in the absence of any boundaries. In reality, free diffusion is rarely encountered in a biological tissue sample. Instead, the presence of restricting barriers, such as cell walls, membranes or axonal myelin sheaths impede the motion of the water molecules and alters their displacement pattern. In this case, the diffusion pattern is not only influenced by the diffusivity of the medium but more importantly informs about the characteristics of the surrounding environment on the scale of the mean displacement.

The observed effects on the diffusion MR signal can be quite diverse, depending on the type and location of barriers within the sample. Figure 2.5 illustrates different diffusion environments and their effect on the root-mean-squared-displacement (RMSD) of molecules. It is helpful to further distinguish two different motion patterns in the presence of barriers as restricted and hindered diffusion. Restricted diffusion is seen when the movement of water molecules

is confined in closed spaces, such as impermeable cells wall. Those molecules experience restricted diffusion in that the molecules cannot displace farther than the confines of the cell. In hindered diffusion, the water movement of molecules is impeded however not confined within a limited space. Hindered diffusion best describes water motion in the space between densely packed cells or axons. The aim of diffusion MRI is to characterise the diffusion motion and thus infer some characteristics of the tissue non-invasively.

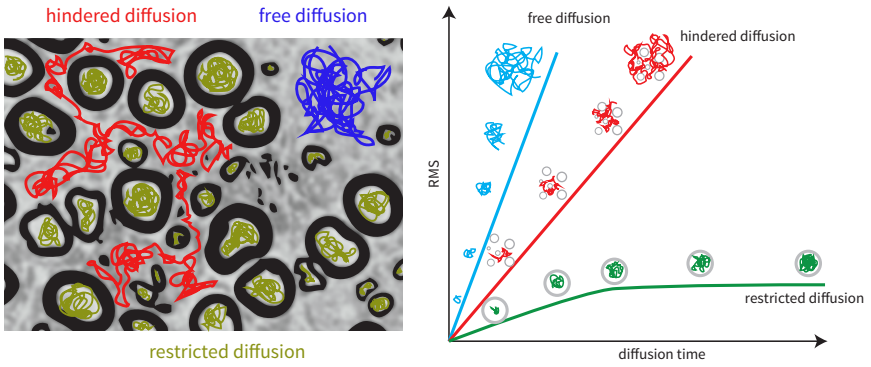

(a) Illustration of molecular movement in different tissue environments

(b) Root-mean-squared displacement over prolonged diffusion time for different tissue environments.

Figure 2.5: *Free, hindered and restricted, diffusion patterns and root-mean-squared displacement over different diffusion times.*

2.3.3 The Stejskal-Tanner PGSE experiment

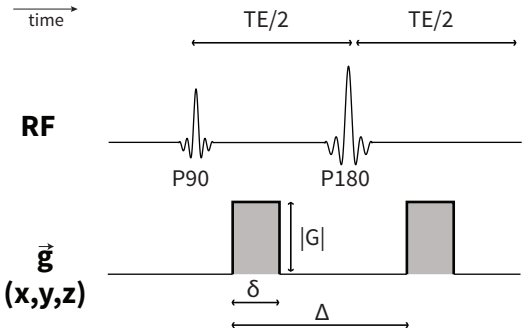

Figure 2.6: *Pulse sequence diagram of PGSE sequence. Image encoding gradients are omitted for clarity.*

The MRI signal can be made sensitive to the movement of the water molecules within the tissue, providing contrast about their molecular displacement on a sub-voxel scale. By far the most commonly used method for diffusion MRI is the pulsed gradient spin echo (PGSE) sequence, introduced by Stejskal et al. [142]. The PGSE sequence, as shown in Figure 2.6, is based on the standard SE sequence with an additional pair of identical diffusion weighting gradients, which make the sequence sensitive to the diffusion of water molecules.

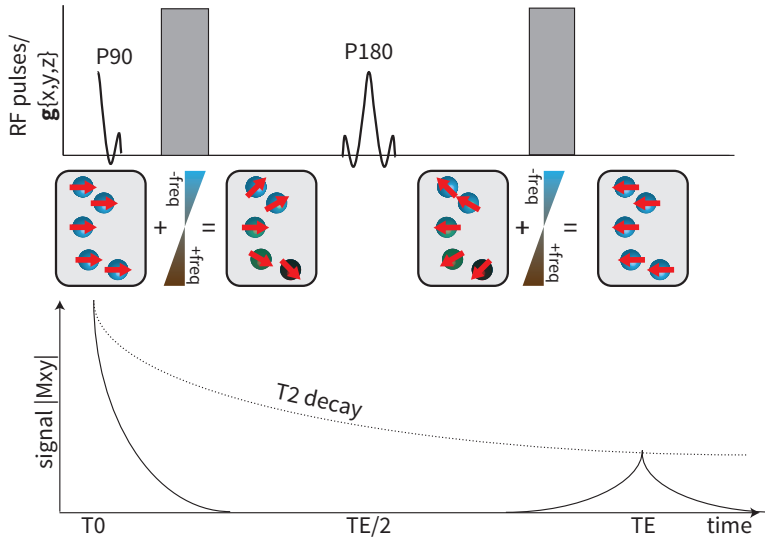

(a) Spin phase distribution in case of no molecular motion. The phase dispersion introduced by the first diffusion gradient is completely reversed by the second diffusion gradient.

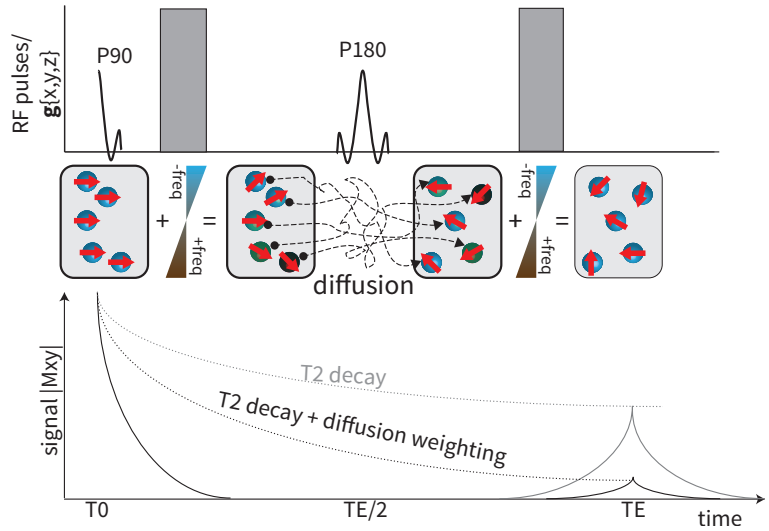

(b) Spin phase distribution in case of diffusing molecules during the diffusion time Δ. Because of motion, the individual molecules experience different phase offsets at the first and second diffusion gradients. As a result, there remains some phase incoherence after the second diffusion gradient, which culminates into an attenuation of the total spin echo response.

Figure 2.7: *Cartoon of the principle of diffusion encoding in the PGSE experiment. The diagrams present the spin development over the course of the sequence in the case of: (a) no diffusion or (b) diffusing molecules.*

Figure 2.7 illustrates the principle of diffusion encoding using the PGSE sequence. The first diffusion gradient adds a phase offset dependent on each molecule's position. If the molecule's position doesn't change, the second diffusion gradient will reverse the phase offset (illustrated in Figure 2.7a). However, in the case of motion due to diffusion, the individual positions will differ between the first and second diffusion gradient, resulting in a reduced signal amplitude (illustrated in Figure 2.7b). The degree of signal loss is dependent on the rate of diffusion in the tissue but is also controlled by the parameters of the PGSE sequence, namely:

- the diffusion gradient strength ($|G|$) and diffusion gradient direction ($\vec{g}$),
- the diffusion gradient pulse duration (δ),
- the diffusion time (Δ) between both gradient pulses.

In the literature the combination of those PGSE parameters is often summarised in terms of the diffusion weighting factor b-value [92], which is defined as:

$$b = \gamma^2 |G|^2 \delta^2 (\Delta - \frac{\delta}{3}), \tag{2.6}$$

where γ is the gyromagnetic ratio. The theoretical background of the b-value formula will be explained in Section 2.4.6.

Eddy current distortions: A common problem in diffusion imaging is image distortion caused by eddy currents that are induced in the gradient system by switching the strong diffusion encoding gradients. When the diffusion gradient pulses are switched on and off, the induced eddy currents set up magnetic field gradients that may persist after the primary gradients are switched off. Such residual gradient fields can combine with the imaging gradient pulses such that the actual gradients experienced in the imaged objects are not exactly the same as those that were programmed to encode the image. If this error is not taken into account, it produces geometric distortion in the final reconstructed images.

A possible solution to eddy current artefacts is to modify the standard single spin-echo pulse sequence to nullify eddy current effects. Most common is the so-called double refocussed pulsed gradient spin echo (dPGSE) sequence[127] (shown in Figure 2.8), which relies on replacing the mono-polar gradients in the single PGSE sequence by two pairs of gradients with opposing polarity. Providing the duration of the eddy current fields is much longer than the duration of the gradients, the opposite eddy current fields tend to cancel out. By applying diffusion gradients with a shorter duration, the cancellation of long-term eddy currents can be achieved, enabling the minimization of the eddy currents on the image encoding.

The dPGSE is arguably one of the most effective way of minimising eddy currents at the time of signal generation. However, the dPGSE can not always be used as not all MRI scanner manufacturers supply it by default. Further concerns include potential signal-to-noise loss, and more severe B_1 inhomogeneity effects due to the presence of an extra 180° RF-pulse. As an alternative,

the diffusion weighted images can be corrected for eddy current distortions retrospectively, e.g. by employing affine image registration to align all Diffusion Weighted Imaging (DWI) data, using a non-diffusion weighted image as the target[128].

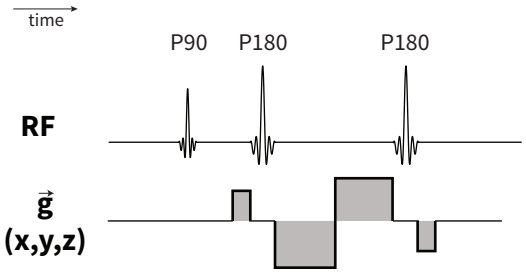

Figure 2.8: *Diagram of the double refocussed PGSE sequence. Image encoding gradients are omitted for clarity.*

2.4 Analysis of Diffusion MRI Data

Like T1- and T2-weighted MRI, diffusion MRI can be used as a qualitative imaging method, e.g., it is widely used in the early diagnosis of stroke [106, 155]. Moreover, diffusion MRI has also proven to be a very powerful tool in the quantitative assessment of tissue properties through parameter maps. However, this type of analysis demands a systematic approach toward the acquisition of signal samples, especially in view of the inherently low SNR and large number of acquisition protocol parameters of diffusion MRI.

Most commonly, diffusion MRI is processed in terms of a model-based analysis, i.e. using a mathematical description of the diffusion signal that can be referred back to the tissue properties. We can break down the model-based analysis pipeline into its main building blocks:

Acquisition: The set of actual diffusion MR measurements. Any quantitative analysis of the diffusion MRI signal usually needs many samples of different PGSE parameters, e.g. many different gradient encoding directions and/or $|G|$,δ, Δ combinations. We formally define such a combined set of n singular PGSE acquisitions as a protocol ($\mathcal{P}$):

$$\mathcal{P} = \{(\vec{g}_1, |G|_1, \delta_1, \Delta_1), \cdots, (\vec{g}_n, |G|_n, \delta_n, \Delta_n)\}, \tag{2.7}$$

or alternatively using the shortcut term b as defined in Equation 2.6:

$$\mathcal{P} = \{(\vec{g}_1, b_1), \cdots, (\vec{g}_n, b_n)\}.$$

Several other terms are are found in the literature that to describe certain aspects of an acquisition protocol. We summarise the most commonly used terms in the following paragraph.

A diffusion gradient scheme usually describes a set of diffusion gradient directions only without specifying PGSE pulse parameters or b-values. The term high-angular-diffusion-imaging (HARDI) describes a special case of gradient scheme with a high number diffusion directions (>60), which are uniformly sampled over the unit sphere[147, 149]. A *shell* in the context of diffusion MRI refers to a protocol or subset of a protocol with several different gradient directions acquired at the same b-value.

Different analysis methods have different requirements on the acquisition protocol. While it suffices for some methods to acquire few samples of the PGSE parameter space, other methods require one or more HARDI shells with different b-values and/or many different $(\vec{g}, |G|, \delta, \Delta)$ combinations.

Diffusion model: The diffusion model is a mathematical approximation of the diffusion process. The diffusion model is usually controlled by a set of feature parameters Φ, which can be (directly or indirectly) related back to the sample environment of the diffusion process. The diffusion model is usually associated closely with a mathematical formulation $S(\Phi; \mathcal{P}_i)$ of the predicted diffusion MR signal for a given acquisition $\mathcal{P}_i \in \mathcal{P}$ and set of diffusion model parameters Φ.

Fitting: The fitting procedure links the observed signals from the acquisition to the diffusion model. The aim is to infer properties from the acquired data, which ideally provide insight in certain characteristics of interest of the underlying sample. In most cases, a forward-modelling approach is applied, i.e., the acquired signal is fitted via a signal model $S(\Phi; \mathcal{P}_i)$ that has been determined *a-priori* to find the particular Φ that explains the acquired data best.

In the remainder of this section we will discuss some of the most common models and analysis methods, with particular focus on the techniques that were used in this dissertation.

2.4.1 Short gradient approximation and the q-space formalism

If we assume the diffusion gradient pulse δ to be sufficiently short, multiple times smaller than the diffusion time Δ, any motion of water molecules during the diffusion encoding gradient time can be neglected. In the so-called short gradient pulse (SGP) regime ($\delta \ll \Delta$), the diffusion echo attenuation S for a specific PGSE acquisition can be expressed as the integral of the net phase shifts over all water over all molecule positions (r) weighted by the conditional probability $P(r|r')$ of the molecule's movement from position r to r'[29]:

$$S(|G|, \delta, \Delta) = \iint P(r)P(r|r', \Delta) \exp[-i \cdot \gamma\delta|G| \cdot (r' - r))]dr'dr. \tag{2.8}$$

We can now describe ensemble molecule motion pattern over one voxel by the average diffusion probability density function (dPDF) (often referred to as the average propagator[75]) as the average probability of all particles moving the distance R independent of their starting position:

$$\overline{P}(R, t) = \int P(r)P(r|r + R, t)dr. \tag{2.9}$$

When Equation 2.9 is substituted in the signal Equation 2.8, we obtain:

$$S(|G|, \delta, \Delta) = \int \overline{P}(R, \Delta) \exp[-i \cdot \gamma \delta |G| \cdot R] dR, \tag{2.10}$$

If we further introduce the **q**-value (or wavenumber) as

$$\mathbf{q} = \frac{\gamma \mathbf{G} \delta}{2\pi}, \tag{2.11}$$

the signal equation can be written as:

$$S(q, \Delta) = \int \overline{P}(R, \Delta) \exp[2\pi i \cdot q \cdot R] dR. \tag{2.12}$$

It is easy to see that Equation 2.12 presents a simple Fourier relationship between the signal S and the dPDF. This relationship can be exploited in q-space analysis, where the diffusion signal is measured with many different q-values at a certain fixed diffusion time. The inverse Fourier transformation of the measured signal directly gives the dPDF at a fixed diffusion time Δ without the need to impose any constraints on its shape.

2.4.2 Q-space imaging

The combination of q-space analysis with MR imaging methods is called **q**-space imaging (QSI)[7, 29]. QSI provides the full displacement probability profile in each voxel of the imaged volume. However, the visualization and interpretation of the full displacement profile in each voxel is complicated and therefore impracticable for clinical application. Instead, it is more common to derive summary statistics from the dPDF that describe specific features of the displacement profile. The most widely used parameters are:

- zero displacement probability (P0)
- full width of half maximum (FWHM)
- kurtosis (K)

Figure 2.9 illustrates the QSI analysis performed steps and gives examples of P0, FWHM and K parameter maps in the spinal cord.

The P0 and FWHM parameter describe the height and width of the displacement profile. Generally, high P0 and low FWHM can be interpreted as indicators of increased impedance of diffusive motion; low P0 and wide FWHM are related to more free (or less hindered) diffusion. The FWHM is of particular theoretical interest as it can be directly related to the size of the restricted compartment in simple geometries via the autocorrelation function when diffusion is completely restricted [38, 85]. Sometimes the RMSD of Einstein's formula (see Equation 2.5) is reported instead of FWHM. A simple conversion factor between FWHM and RMSD was suggested by Cory et al. [38] as:

$$\text{RMSD} = 1.443 \cdot \text{FWHM}, \tag{2.13}$$

although the equality is only true if the diffusion profile is truly Gaussian, but not for restricted diffusion.

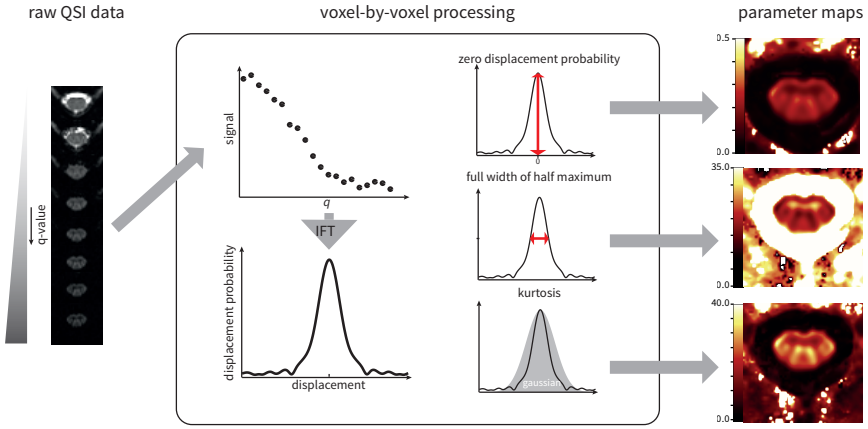

Figure 2.9: *QSI analysis pipeline and example parameter maps.*

The kurtosis parameter, here defined as the excess kurtosis [76], describes how much a distribution differs from the normal distribution. Kurtosis is defined as the standardised fourth central moment of a distribution minus 3 (to make the kurtosis of the normal distribution equal to zero). For a finite sample of n datapoints the kurtosis K is computed as:

$$K = \frac{\frac{1}{n}\sum_{i=1}^{n}(x_i - \overline{x})^4}{\left(\frac{1}{n}\sum_{i=1}^{n}(x_i - \overline{x})^2\right)^2} - 3 \tag{2.14}$$

with $\bar{x}$ being the sample mean. A high kurtosis distribution has a narrower peak and long, fat tail compared to a normal distribution. A low kurtosis distribution has a more rounded peak and a shorter, thinner tail. In the context of diffusion analysis, the kurtosis parameter can be used to quantify how much the dPDF differs from a Gaussian displacement distribution [70]. High K values can therefore be interpreted as an indicator of restricted diffusion in a sample.

Limitations of QSI

QSI parameters measured in nervous tissue are often interpreted as a direct indicator of axonal architecture, such as the mean axon diameter (MAD). Early studies have demonstrated that q-space analysis can indeed provide exact estimates of the geometry in simple samples, e.g. yeast cells [38] or blood cells [85]. However, experiments on real nervous tissue have shown that the interpretation of q-space parameters in axonal tissue is more complicated [7, 8, 17, 80]. Assaf et al. [7] suggested that the displacement profile of nervous tissue can be expressed as a combination of at least two compartments exhibiting hindered and restricted diffusion. A recent study of QSI in the *in-vivo* human brain by Nilsson et al. [109] confirmed that the FWHM perpendicular to white matter fibres did not change with diffusion time, while parallel FWHM increased linearly with the square root of diffusion time. This suggests the presence of restricted diffusion across WM tracts and non-restricted diffusion along WM tracts respectively (see Figure 2.5). It is sometimes assumed that hindered and

restricted diffusion correspond to two different compartments: intra-cellular (IC) and extra-cellular (EC) water, although there is an ongoing debate over the interpretation of these results (see e.g. [82, 107]).

Since q-space analysis provides the average displacement probability over the whole voxel, the q-space measurement is affected by both IC and EC compartments as well as by the amount of exchange between the two. As a result, the dPDF may be broader than the actual MAD would suggest, due to the addition of displacements from hindered diffusion in the EC compartments. Other factors such as the distribution of sizes and variety of shapes further complicate the interpretation of q-space parameters to infer the real axon diameter distributions.

2.4.3 Apparent diffusion coefficient

In the absence of any diffusion impeding barriers, the dPDF takes the form of a simple Gaussian probability distribution, which is only dependent on the diffusion time t and the diffusion coefficient d:

$$P(\mathbf{r}_0, \mathbf{r}, \Delta) = \frac{1}{\sqrt{(4\pi dt)^3}} \exp\Big(- \frac{|\mathbf{r} - \mathbf{r}_0|^2}{4dt} \Big). \tag{2.15}$$

This closed form solution for the dPDF can be substituted in the general q-space formalism given in Equation 2.12, simplifying it to:

$$S(s_0, d; \delta, \Delta, G) = s_0 \cdot \exp(-(2\pi\gamma\delta)^2 \Delta \cdot d), \tag{2.16}$$

with model parameters being the diffusion coefficient d and the baseline signal s_0, i.e., the non-diffusion weighted T2w signal. It is often more convenient to rewrite above equation terms of the b-value as:

$$S(s_0, d; b) = s_0 \cdot \exp(-b \cdot d), \tag{2.17}$$

with $b \approx -(2\pi\gamma\delta)^2\Delta$ under the SGP assumption of $\delta \ll \Delta$.

In true free diffusion, d is simply the diffusion coefficient of the medium and the signal equation above is exact. However, in real biological tissue, virtually all molecules will have interacted with their environment within the timescale of a typical diffusion MR experiment. In this case the above expression is just an approximation of the underlying true dPDF and d above is not only related to the diffusivity of the medium but also informs about the diffusion impedance caused by molecules interacting with the environment. To highlight the difference to the classical definition of the diffusion coefficient, we refer to d as the apparent diffusion coefficient (ADC).

The model parameters s_0 and the ADC are tissue dependent and can be estimated by acquiring a minimum of two diffusion weighted images with different b-value (usually $b = 0$ and $b = 800 - 1200 mm/s^2$ for *in-vivo* nervous tissue). Typically a simple log-transformation of Equation 2.18 is used to obtain a linear equation:

$$log(S(s_0, ADC; \mathcal{P}_i)) = log(s_0) - (b \cdot ADC), \tag{2.18}$$

for each measurement $\mathcal{P}_i$ of the acquisition protocol $\mathcal{P}$. The linear equation system can then be solved efficiently, e.g. using a least squares approach, to obtain maps of s_0 and ADC values.

2.4.4 Diffusion Tensor

In ordered tissue like white matter diffusion is directional, i.e., the ADC will depend on the direction $\vec{g}$ of the applied gradient. To reflect the directionality, Equation 2.18 can be extended from the scalar representation of the diffusion coefficient d to reflect the complete 3-dimensional diffusion co-variance matrix [18], obtaining the Diffusion Tensor (DT) formulation:

$$S(\mathbf{D}; b, \vec{g}) = S_0 \exp(-b\vec{g}^T \mathbf{D}\vec{g}) \text{ with } \mathbf{D} = \begin{bmatrix} d_{xx} & d_{xy} & d_{xz} \\ d_{xy} & d_{yy} & d_{yz} \\ d_{xz} & d_{yz} & d_{zz} \end{bmatrix}. \tag{2.19}$$

As before, the parameters of the DT model are the s_0 non-diffusion weighted signal baseline and the diffusivity d, now being a positive symmetric 3×3 co-variance matrix. The parameters can be estimated in a similar fashion to the ADC model using the log-transformation of the signal and a system of linear equations. In addition to the ADC model, the accurate estimation of all the directional DT components requires a minimum of 6 different diffusion weighted measurements with non-coplanar gradient directions. However, we usually acquire more signals to overdetermine the solution, add noise control and increase directional resolution [72].

By an Eigen decomposition of the DT we obtain the three eigenvectors $\vec{v}_1, \vec{v}_3, \vec{v}_3$ and their corresponding eigenvalues $\lambda_1 \geq \lambda_2 \geq \lambda_3$. The first eigenvector can be interpreted as the principal diffusion directions with λ_1 being the principal diffusivity. Usually λ_1 is also referred to as the axial diffusivity (AD) as it corresponds with the diffusivity parallel to white matter axons [19]. Other commonly used DTmetrics are:

- The mean diffusivity (MD), computed as:

$$MD = \frac{\mathrm{Tr}(D)}{3} = \frac{\lambda_1 + \lambda_2 + \lambda_3}{3}. \tag{2.20}$$

- The fractional anisotropy (FA) that represents the degree of diffusion anisotropy in each voxel. FA increases with directional dependence of particle displacements and is greatest when diffusion is highly directional. FA is computed by

$$FA = \sqrt{\frac{3}{2}} \frac{\sqrt{(\lambda_1 - MD)^2 + (\lambda_2 - MD)^2 + (\lambda_3 - MD)^2}}{\sqrt{\lambda_1^2 + \lambda_2^2 + \lambda_3^2}} \tag{2.21}$$

- The radial diffusivity (RD) is the average diffusivity perpendicular to the major diffusion direction:

$$RD = \frac{\lambda_2 + \lambda_3}{2}. \tag{2.22}$$

It should be noted that the interpretation of AD and RD as parallel and perpendicular diffusivities only holds true in the case of a single fibre population within the image voxel, but breaks down in the case of more complex fibre configurations such as crossing or bending fibres. Furthermore, in case of WM pathological processes the DT shape can undergo significant changes, which makes the notion of ”axial” and ”radial” diffusivities misleading if not interpreted carefully [158].

2.4.5 Limitations of the SGP approximation

Unlike modern Nuclear Magnetic Resonance (NMR) spectrometers and preclinical small bore scanners, most clinical MRI systems are only equipped with limited maximal gradient strength (usually 40-60 mT/m). On these systems the necessary high q-values, e.g., needed for q-space analysis cannot be achieved without prolonged diffusion gradient pulse durations. Mitra [104] showed that the effective molecule displacement measured with a finite diffusion pulse δ is equivalent to the distance between the centre-of-mass (COM) of the molecule trajectories occurring while the diffusion gradients are applied. If the SGP condition $\delta \ll \Delta$ is fulfilled, the observed distance between the COMs of the trajectories is approximately the same as the true displacement of the molecule. However, if δ is long, molecules movement will occur during the diffusion gradient pulses and only the displacement between the COMs will be observed. As illustrated in Figure 2.10, in the case of restricted diffusion, this increase in gradient pulse duration will cause the underestimation of the true displacement. When implementing QSI protocols on a clinical scanner, one has to be wary of the effect of the finite gradient pulse duration and its implications. Usually, clinical studies of QSI have to violate the SGP condition to achieve sufficiently high q-values. As expected from the COM effect, this causes an artifactual reduction of the RMSD. This has been confirmed in simulation [90, 93] and various experimental studies in phantoms [12, 91], excised tissue [17, 97] and even in *in-vivo* human scans [109]. As a consequence, the estimated displacement profile has to be interpreted with caution as it will not reflect the true displacement in the tissue. The SGP violation is a fundamental problem in the above models and can only be avoided with an increase of the maximum gradient strength.

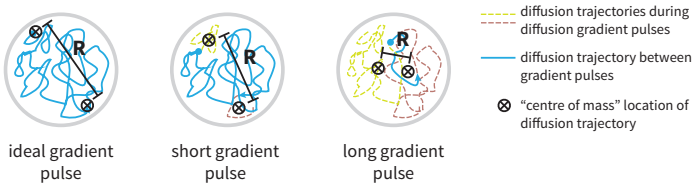

Figure 2.10: *Illustration of the centre-of-mass effect on the apparent molecules displacement for different gradient pulse durations.*

Some experimental clinical scanners are already equipped with gradient systems capable of generating up to 300mT/m [145]. However, those dedicated systems are usually designed for a specific research project and the general availability of those strong whole body gradients in the future is doubtful

due to their high costs. Economic feasibility aside, the use of higher gradient strengths and shorter pulse width also increases the risk of peripheral nerve stimulation (PNS) and might cause more discomfort for the subjects.

2.4.6 Gaussian phase approximation

As discussed above, the SGP approximation is often impossible to fulfil on typical clinical scanners. An alternative model of the diffusion process is given by the Gaussian phase distribution (GPD) approximation. In contrast to the SGP, the GPD offers a description of the diffusion MR signal in the presence of finite δ under the assumption that the phases of the spins due to the magnetic field gradients are Gaussian distributed.

In the SGP approximation we use the probability density function of spin displacements, whereas the GPD approximation considers the distribution function of spin phases $P(\phi, \Delta)$ at the echo time TE having phase ϕ. The total signal in terms of $P(\phi, \Delta)$ is

$$S(\delta, \Delta, \mathbf{G}) = \int P(\phi, \Delta) \cos \phi d\phi. \tag{2.23}$$

For molecules undergoing free diffusion, characterised by a single diffusion coefficient d, P is Gaussian so that the signal can be expressed by the following formula (see Price [125] for details):

$$S(\delta, \Delta, \mathbf{G}) = \exp\Big(-\gamma^2 |\mathbf{G}|^2 \delta^2 (\Delta - \delta/3) d \Big). \tag{2.24}$$

This equation provides the theoretical underpinning of the definition of the popular b-value introduced in Equation 2.6. Please note in the case of free diffusion the SGP approximation becomes a special case of the GPD approximation:

$$S(d; \delta, \Delta, \mathbf{G}) = S_0 \exp(-\gamma^2 |\mathbf{G}|^2 \delta^2 (\Delta - \delta/3) d) \tag{2.25}$$

$$\Leftrightarrow S(d; \delta, \Delta, \mathbf{G}) = S_0 \exp(-\gamma^2 |\mathbf{G}|^2 \delta^2 \Delta d) \qquad \text{if } \frac{\delta}{\Delta} \to 0 \tag{2.26}$$

2.4.7 Models of restriction

The above analytic models are all based on the assumption that the diffusion pattern can be described well with a diffusion process. However, many studies have shown that those models inadequately describe restricted diffusion, which is observed, e.g. in coherent white matter tracts. Over the years, various analytic solutions have presented for simple restricting geometries such spheres, parallel planes under either SGP or GPD approximation [15, 28, 93].

The cylinder geometry is particularly well suited to approximate diffusion within mylelinated axons, where diffusion is mainly restricted perpendicular and unrestricted parallel to the myelin barriers. We present here the analytic solutions for the diffusion MR signal in cylinders from PGSE with finite gradient pulses under the GPD assumption. The following analytic solution for the diffusion signal from particles diffusing within the cylinder of radius R was independently proposed by Stepišnik [143] and Van Gelderen et al. [151]:

$$\ln S = -2\gamma^2 \mathbf{G}^2 \sum_{m=1}^{\infty} \frac{2da_m^2\delta - 2 + 2e^{-da_m^2\delta} + 2e^{-da_m^2\Delta} - e^{-da_m^2(\Delta-\delta)} - e^{-da_m^2(\Delta+\delta)}}{d^2 a_m^6 (R^2 a_m^2 - 1)} \tag{2.27}$$

where a_m is the mth root of equation $J_1'(a_m R) = 0$ and J_1' is the derivative of the Bessel function of the first kind, order one.

2.4.8 Compartment models

Using a-priori information about the microstructure of the investigated sample, the diffusion signal can be approximated by a combination of these simple geometric compartments. Each of the n different compartments possesses the model parameters Φ_i from which the signal S_i is computed. Each compartment is assigned a volume fraction f_i with $0 \leq f_i \leq 1$ for all $1 \leq i \leq n$. For an acquisition protocol $\mathcal{P}$, the signal model under the combined model parameter set $\Phi = \Phi_1 \cup \ldots \cup \Phi_n$ is then given by:

$$S(\Phi; \mathcal{P}) = \sum_{i=0}^{n} f_i \cdot S_i(\phi_i; \mathcal{P}). \tag{2.28}$$

Bi-exponential model

One of the simplest compartment models is the bi-exponential model, expressing diffusion as the summation of two separate mono-exponential decay curves (see Equation 2.18) with two different diffusion coefficients (usually named the slow component, ADC_s and fast component, ADC_f):

$$S(f_s, f_f, ADC_s, ADC_f; b) = f_s \exp(-b \cdot ADC_s) + f_f \exp(-b \cdot ADC_f). \tag{2.29}$$

Experiments by Clark et al. [32] in *in-vivo* brain data demonstrate good agreement between measurements and fitted signal curves over a range of b-values. However, the biophysical interpretation of the two compartments is still in debate and the relation between the compartments and the microstructural properties of white matter remains unclear.

2.4.9 Geometric multi-compartment models of nervous tissue

Stanisz' model Stanisz et al. [139] were the first to propose a model that reflects the underlying micro-anatomy of nervous tissue. They introduced a model of restricted diffusion in bovine optic nerve using a three-compartment model approach. In their model, prolate ellipsoids represented axons, spheres represented glial cells and Gaussian diffusion was assumed in a homogeneous extra-cellular medium surrounded by partially permeable membranes. Experimental data was in agreement with the signal predicted by their model and showed significant departure of the DWI signal from the simple Gaussian model. However, the complexity of this models requires very high quality measurements, typically only achievable in NMR spectroscopy rather than MRI.

The CHARMED model Assaf et al. [6] developed the Composite Hindered and Restricted Model of Diffusion (CHARMED) model of cylindrical axons with gamma distributed radii to estimate axon diameter distributions in white matter tissue. The CHARMED model assumes two compartments, representing diffusion in intra-axonal and extra-axonal space. The intra-axonal compartment is modeled by parallel cylinders, with the size of radii following a

gamma-distribution. The extra-cellular compartment is modeled by a DT with the principal diffusion direction $\vec{v}_1$ aligned with the long cylinder axis. Alexander [3] validated the model in in-vitro optic and sciatic nerve samples and estimated parameters show good correlation with corresponding histology. In later work, Barazany et al. [16] extended the CHARMED model by an isotropic diffusion compartment to account for partial volume effects and contributions from areas of CSF. They apply their model to image axon size distributions in the corpus callosum of live rat brain. However, in both experiments, scan times are long and the high 7T magnetic field and maximum $|G|$ (400 mT/m) are impossible to achieve on human scanners, typically operating at 1.5-3T with maximum $|G|$ between 30-60 mT/m.

Alexander's minimal model of white matter diffusion Alexander et al. [4] uses a model similar to CHARMED to demonstrate measurements of axon diameter and density in excised monkey brain and live human brain on a standard clinical scanner with multi shell HARDI. The minimal model of white matter diffusion (MMWMD) introduces several modifications to the CHARMED models [44]. The most distinguishing difference to CHARMED is that the distribution of cylinder radii is replaced by a fixed cylinder radius. The MMWMD expresses diffusion in a white matter voxel as a combination of water particles trapped inside three different compartments:

1. Intra-axonal water experiencing diffusion restricted inside cylindrical axons with equal radius R [143, 151]

2. Extra-axonal water that is hindered due to the presence of adjacent axons. Diffusion is approximated by a diffusion tensor, with parallel diffusion coefficent $d_{\parallel}$ in the direction of the cylinders and symmetric diffusion $d_{\perp}$ in the perpendicular directions.

3. Water that experiences unhindered diffusion, e.g., in the CSF, modeled by an isotropic Gaussian distribution of displacements with diffusion coefficient d_I.

4. Non-diffusing water, e.g., trapped in membranes (no parameters).

He reduced the number of free model parameters by expressing $d_{\perp}$ using the tortuosity approximation proposed by Szafer et al. [144].

Model taxotomy The examples presented above only present a very small subset of possible compartment models that can be obtained by combining the different possible decriptions of diffusion. The selection of the best suited model is complicated; on the one hand complex models such as CHARMED might better characterise the underlying tissue than e.g. the diffusion tensor. On the other hand, increasing model complexity can lead to overfitting and false parameter estimation. Panagiotaki et al. [118] approached this model selection problem systematically, comparing a large number of different compartment models. They propose a taxonomy of one-, two- and three-compartment models including the models described above. In this taxotomy

the three compartments represent restricted, hindered and isotropic diffusion respectively. In detail the studied compartments were:

Restricted diffusion: is described by a Stick (cylinder with zero radius) , or a non-zero radius Cylinder either with a single radius or gamma-distributed radii

Hindered diffusion: is either represented as a Tensor (full DT), Zeppelin (cylindrically symmetric DT) or Ball (isotropic DT).

Isotropic diffusion: is described by Dot (stationary molecules), Sphere (isotropically restricted) or Cylinders with isotropically distributed directions either as Astro-sticks (zero radius) or Astro-Cylinders (non-zero radius).

A total of 47 different combinations of these compartments were tested using a very comprehensive dataset comprising many different combinations of, δ, Δ and $|G|$ acquired in the corpus callosum (CC) of fixed rat brain. They compared and ranked the models using the Bayesian Information Criterion, which rewards the goodness of fit between the data and predicted signal but also penalises a model's complexity. They concluded that three- and two-compartment models including non-zero diameter Cylinder compartments explain the data well while DTI performs worse. A recent similar study of *in-vivo* CC [54] confirmed these findings although the hardware limitations of the clinical MR system give rise to preference of simpler models of restriction such as the Stick.

2.4.10 Active Imaging

More complex models usually require DWI acquisitions with several different diffusion weightings at various diffusion times. For example Barazany et al. [16] perform approx. 900 different combinations of $0 \leq |\vec{g}| \leq 300mT/m$, $0 \leq \delta \leq 30ms$ and $0 \leq \Delta \leq 30ms$ to estimate the axon diameter distribution of live rat brain. This extensive sampling of the PGSE parameter space requires long acquisition times (between hours and days) and is not feasible for *in-vivo* clinical scanning.

The principle of the "Active Imaging" protocol optimisation framework of [3] is to find the protocol $\mathcal{P}$, that allows the most accurate estimation of the tissue model parameters under given hardware and time constraints. The Fisher information matrix (FIM) (FIM) provides a lower bound on the inverse covariance matrix of parameter estimates, i.e., the $\mathcal{P}$ that maximizes the FIM will maximize the precision of those estimates. Alexander uses the Cramer-Rao lower bound (CRLB) as the optimality criterion [111], which is defined as the trace of the inverse FIM of protocol $\mathcal{P}$ and tissue model parameters ϕ:

$$D(\phi, \mathcal{P}) = \mathrm{Tr}[(\mathbf{J}^T \Omega \mathbf{J})^{-1}], \tag{2.30}$$

where $\mathbf{J}$ is the $N \times \mathrm{size}(\phi)$ Jacobian matrix with the ijst element defined as:

$$\partial S(\vec{g}_i, \delta_i, \Delta_i)/\partial \phi_j. \tag{2.31}$$

Intuitively, the CRLB defines a lower bound on the variance of the fitted model parameters ϕ for a given protocol $\mathcal{P}$. In the original approach Ω is the identity matrix, i.e. all measurements are assigned equal importance.

Alexander [3] then uses a stochastic optimization algorithm [165] that returns $\mathcal{P}'$ with minimal D among all possible $\mathcal{P}$ with respect to the given scanner hardware limits. The optimisation framework was used in Alexander et al. [4] to estimate the parameters of the MMWMD, described in section 2.4.9 using a standard clinical Philips 3T scanner with maximum $|G|$ of $60mT/m$ and a maximum scan time of one hour (total number of acquisitions $N = 360$). To achieve estimates independent of fibre orientation, the N acquisitions are divided in M sets of different PGSE settings with gradient directions in each set being fixed and uniformly distributed over the sphere as in [36]. They performed *in-vivo* scans of the corpus callosum and compared their axon diameter and density indices with high resolution scans of *ex-vivo* monkey brain and previously published histology studies. They found that the trends in diameter and density agreed with both *ex-vivo* scans and histology, although the axon diameter was over-estimated. This is mainly an effect of limited gradient strength as has been shown in [44].

It should be noted that this method by design produces protocols that minimise the variance in parameter estimates, but it does not account for any potential bias between the estimates and real tissue parameters. Therefore, this approach crucially depends on the careful selection of both the tissue model and a realistic set of model parameters a-priori to the optimisation process [3, 4].

2.4.11 Limitations of geometric compartment models

All the compartment model approaches discussed above are based strongly on assumption made about the structure of tissue to be imaged and are crucially dependent on the validity of the a-priori knowledge that goes into the design of the model and acquisition. But of course, neural tissue is much more complex than what can be captured in those relatively simple biophysical models and the situation is even further complicated when the biophysical models are applied to pathological conditions, in which the tissue configuration might have changed dramatically.

Ideally, biophysical models should therefore be validated against independent gold-standard techniques to understand the relationship between the model parameters and real tissue parameters. However, obtaining reliable and highly detailed information regarding the microstructure in living tissue is practically impossible and typically one has to rely on cross validation with other methods such as numerical simulations or data from animal models and excised post-mortem tissue.

While all those methods can help to understand certain aspects of the model, they also suffer from their own imperfections, which makes any model validation a fundamentally challenging problem. Monte-Carlo simulations of the diffusion signal are the most cost-effective way to test arbitrary acquisition protocols in a variety of geometric configurations[62]. They are very versatile and

can easily be tuned to produce a large range of healthy and diseased microstructure representations (see e.g. [63, 108]). However, the simulated structure is still based on a simple geometric approximation of tissue and can't offer an accurate representation of live tissue. Animal models and post-mortem tissue provide a much better approximation of the live human tissue configuration. However, those methods are also much more costly and harder to control for a specific range of microstructure parameters or pathologies. Furthermore, the effect of tissue fixation also influences tissue microstructure and might skew model parameters in an unpredictable fashion[45, 133].

In essence, it is important to administer caution when fitted model parameters are to be interpreted in a clinical context. It is recommended to regard the outcome of any of the biophysical models, such as axon diameter, density or compartment volume fractions, as abstract and imperfect indices that reflect certain aspects of the underlying tissue, instead of misinterpreting them as direct measurements of those properties.

2.5 Diffusion MRI in healthy and diseased spinal cord

Although diffusion MRI in the spinal cord has been studied for over 10 years, its clinical application is still relatively unexplored compared to the brain. This is mostly due to the technical challenges caused by its small structure and problematic imaging conditions, including breathing and cardiac motion and susceptibility artefacts arising from surrounding bony tissue. However, over the last few years, new developments in imaging and post-processing methods have enabled an increasing number of studies of healthy and diseased spinal cord. In this section we will report the diffusion properties of spinal cord tissue as they were observed in previous studies. Furthermore we summarise tissue changes that arise from tissue damage and their effects on DWI-derived parameters. This section will focus on parameters derived under the assumption of Gaussian diffusion, i.e. using ADC or Diffusion Tensor Imaging (DTI) parameters, as those are by far the most established techniques used in SC diffusion imaging.

2.5.1 Diffusion MRI in healthy spinal cord

Water diffusivity in the WM is highly anisotropic, i.e. diffusion occurs preferentially in a particular direction. In highly coherent structures such as the spinal cord WM, diffusion anisotropy is usually seen as caused by restricted diffusion by the axon membrane, myelin sheath, neurofilaments and microtubules, resulting in reduced transverse diffusivity (or RD) compared to the longitudinal diffusivity (or AD) along the WM tracts. The estimated apparent diffusion coefficients in the human spinal cord typically range from $1.0 \times 10^{-3} mm^2/s$ to $2.3 \times 10^{-3} mm^2/s$ along the WM fibres and between $0.1 \times 10^{-3} mm^2/s$ to $1.0 \times 10^{-3} mm^2/s$ across. The range of ADCs found in the cord are highly dependent on the specific microstructure of the tissue under investigation, but also depend on pulse sequence parameters such as diffusion

time and echo time (TE). Despite differences in pulse sequences, a mean ADC in the human cervical spinal cord of approximately $1.0 \times 10^{-3} mm^2/s$ has been reported by several groups [46, 160].

A study by Schwartz et al. [130] showed a significant correlation between cellular morphological parameters and the ADC using combined histological analyses and high resolution *ex-vivo* DTI. Furthermore, AD has been shown to be inversely correlated with both neurofilament and microtubule density as demonstrated in the rat optic nerve[81], implying hindered diffusion caused by neurofilaments and microtubules longitudinal to the axon orientation.

2.5.2 Diffusion MRI in spinal cord injury

Trauma to the spinal cord, and changes occurring during healing, result in alterations of tissue microstructure that are measurable via DWI. The time-course of the disease is broadly staged in three distinct phases: acute, sub-acute and chronic. The remainder of this section will describe each phase in more detail.

Acute phase: In the acute stages of spinal cord injury (SCI), the mechanical disruption of neural tissue structure results in immediate death of cells in the region of the injury. The cell death and disruption of the cell membranes results in axons that are spaced further apart. As a result water molecules can diffuse larger distances before barriers are encountered, which can be detected by increased ADC in animal studies [40, 56], with diffusivity as high as double the diffusion measurements in healthy cord. In addition, edema also occurs in the first moments of traumatic SCI primarily resulting from mechanical disruption of axon cell membranes and damage to local blood vessels [14, 101]. DTI in acute spinal trauma often exhibits a decrease in AD, resulting in an overall decrease in diffusion anisotropy in the lesion sites during the period of severe edema and hemorrhage [56]. This decrease in the AD has been largely attributed to metabolic dysfunction as opposed to specific changes in axon morphology [129].

Sub-acute phase: Following the initial response to spinal trauma there is infiltration of inflammatory cells from both the CNS and periphery. It is unclear how the influx of reactive cell types influences diffusion measurements in the injured spinal cord. Reactive cells, such as glia, produce collagenous scar tissue that is expected to have a relatively high impact on tissue diffusivity. Schwartz et al. [131] demonstrated that the principal DTI eigenvector orientation shows sensitivity to glial cell orientations, although only if they are in sufficient numbers to significantly affect the overall orientation of the particular voxel microstructure. Furthermore, in the subacute stage of SCI, the presence of a large number numbers of astrocytes, microglia, and macrophages is also assumed to decrease the extracellular volume, which could decrease the overall apparent diffusion coefficient, counteracting the initial increase associated with edema. In addition to tissue changes directly at the site of injury, there is also Wallerian degeneration, i.e. degeneration of axons distant from the site of injury

[157], which causes changes in diffusivity even at locations away from the traumatic injury. Axon degeneration first manifests as disintegration of the myelin sheath and cytoskeletal proteins including microtubules and neurofilaments, eventually followed by complete anterograde degeneration. Experimental data suggest extensive retrograde degeneration in the sub-acute phase of SCI [27, 74, 117], resulting from both apoptosis and necrosis [39].

During the degeneration process, RD is typically elevated [40]. The primary explanation for the increase in RD lies in the tissue structural changes that occur during degeneration along with direct effects on the intra- and extracellular space. Anterograde degeneration results in rapid degeneration of both the axonal membrane and myelin sheath, decreasing the number and extent of transverse diffusion boundaries. This is expected to contribute to a higher diffusion coefficient perpendicular to the fibre bundles. Retrograde degeneration also shows a similar, but slightly larger, increase in RD in experimental animal models [40], which is most likely due to axon swelling and the subsequent increase in intracellular space[14].

Chronic phase: Even in the late phase of SCI, defined months to years after the initial injury, differences in tissue morphology in chronic injury are still likely to impact on DWI measurements. Although most of the degenerative processes are stabilized by the chronic stage, there is evidence to suggest degeneration even long after the injury. For example, progressive demyelination can occur even during chronic injury [23, 26]. Remyelination, if it occurs, results in significantly decreased myelin sheath thickness [23, 26, 64, 146] and thus alters the white matter structure in chronic injury. Furthermore, a preferential loss of large diameter axons can also occur in chronic injury[23] resulting in a dominance of small, unmyelinated axons in damaged axonal tracts. Finally, significant atrophy of the spinal cord also occurs in late stages of spinal cord injury[48, 57, 96] causing the remaining axons to be compressed and tightly packed. These structural changes are all expected to contribute to differences in water diffusivity in chronic injury.

Studies of experimental animal models have shown that a decrease in RD and increase in AD are both indicators of the pathological processes in chronic SCI [25, 53, 78, 79, 137, 170] and suggest axonal degeneration and progressive demyelination rostral to the trauma of the cord in the chronic stage of the disease. In humans, diffusion characteristics in chronic injury have not yet been so thoroughly explored. However preliminary evidence of gross morphological changes and atrophy have been illustrated using DTI [34, 47] (see also our own study in Appendix A).

2.5.3 Non-gaussian diffusion in the spinal cord

To date, the application of non-gaussian models of diffusion in the cord is limited almost exclusively to post-mortem tissue and experimental animal models. QSI was first used by Assaf et al. [7] to study the maturation of excised spinal cord. Their results showed that restricted diffusion in the WM increased dramatically with age, while GM changed very little by comparison. Biton et al.

[22] was first to apply QSI to the SC of pigs suffering from myelin deficiencies. They found that regions that were identified as demyelinating lesions in histology correlated very well with areas of increased full width of half maximum (FWHM) in the QSI datasets. While the application of QSI on experimental MRI systems has proven a useful technique, its application *in-vivo* on clinical scanners is hampered by the demand for long scan times and insufficient available gradient strength. Despite these limiting factors, Farrell et al. [50] recently demonstrated the first successful *in-vivo* application of a QSI-like acquisition in a small group of Multiple Sclerosis (MS) patients, despite violating the SGP in their protocol.

2.6 Summary

We have discussed ways of inferring microstructual information from DWI, ranging from simple methods such as ADC or DTI to sophisticated multi-compartment modelling. ADC and DTI are easy to obtain but the simplistic underlying assumptions of Gaussian dPDF is often inaccurate. As a result, different microstructural changes in pathologies can have the same effect on those metrics and therefore cannot be told apart by DTI alone. At least in theory, QSI has the potential to overcome this limitation but requires both very strong diffusion gradients and long acquisition times. Furthermore, QSI derived parameters dPDF measures only relate indirectly to white matter structure and must be carefully interpreted if the SGP is violated.

Using more advanced diffusion models, incorporating anatomical a-priori information about the different compartments of the investigated tissue can overcome the limitations of the simplistic DTI model but at the same time allow more flexibility than QSI. However, *in-vivo* scans are limited in in maximum scan time and hardware capabilities. Under these conditions, finding the optimal set of acquisition parameters is not trivial. The optimisation framework of Alexander can be used to find the DWI protocol that is best suited to estimate the model parameters of interest while it respects the limitations of the clinical setup.

The techniques presented here have the potential to provide information about the location and severity of an injury that might prove useful in the diagnosis and prognosis of a spinal injury. Further, DWI measures could be used as an indicator of neural degeneration and healing. Because of the changes in tissue structure during inflammation and healing, DWI measures are likely to depend on the stage of injury, varying from the acute to chronic stages. While a large range of DWI techniques beyond Gaussian diffusion and DTI are available in the brain to study specific aspects of the microstructural organisation such as axon diameter and axon density, those techniques are still virtually unexplored in the spinal cord. The study of non-gaussian diffusion metrics and more specific geometric models could prove to be a crucial step to better quantify the microscropic changes in SCI to inform better treatment strategies.

Part I

DTI studies

3

Preliminary investigation of position dependency of radial diffusivity in the cervical spinal cord

In this experiment we investigate whether Diffusion Tensor Imaging (DTI) derived parameters are sensitive to the presence of collateral fibres and can be related to the axial position of the acquired slice in the spinal cord (SC).

As this was my first experience of MRI, this project helped me to become familiar with the anatomy of the SC and obtain hands-on experience with DTI and its associated challenges in the SC. Although the number of control subjects is small, the experience gained in the set-up of this study has significantly helped the design of subsequent experiments and development of new methods as will be seen in the next chapter.

3.1 Motivation

The majority of Diffusion Weighted Imaging (DWI) studies have mainly focused on the longitudinal fibres of the SC and relatively little is known about the value of DTI for the assessment of the connective collateral fibres. These fibres rise at an angle with the white matter (WM) longitudinal tracts and enter the SC gray matter (GM). They interconnect with other areas of the SC through the central GM and form part of many functional connections within the SC [30]. Recently Mamata et al. [98] demonstrated that the second DTI eigenvector is corresponding to sprouting collateral fibres. In this study we focus on DTI of the SC *in-vivo* in healthy volunteers with particular interest in the diffusivity changes caused by the presence of the collateral fibres. We aim to investigate whether these DTI parameters are specific to nerve root anatomy and therefore have the potential to be used in spinal cord injury (SCI) to assess the integrity of the axonal connections.

3.2 Methods

Our primary focus in this study was to develop a reliable and reproducible DTI pipeline incorporating acquisition, post-processing and analysis steps. In the following we explore several factors, such as slice positioning, number of signal averages, and partial volume effects, that potentially have an effect on the outcome of the DTI analysis.

3.2.1 Positioning of DTI scans

Accuracy and reproducibility in slice positioning for the DWI acquisitions is crucial to discriminate differences in diffusion parameters between subjects. Since for this study we wanted to position our slices with respect to the neu-

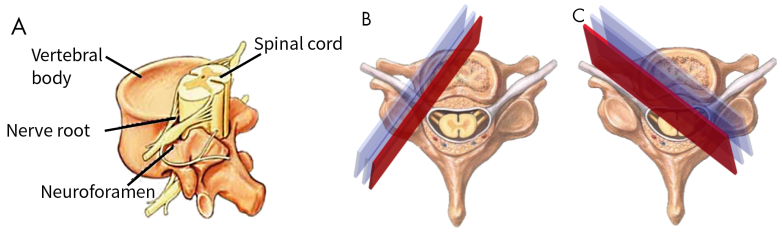

Figure 3.1: *Illustration of location of the neuroforamen and spinal nerve roots (A) and the positioning of oblique sagittal slices for nerve root visualisation (B,C). The red coloured slices illustrate the ideal positioning of the oblique scans. (B) The position of the first sagittal scan is intersecting the neuroforamen, (C) The second scan is aligned parallel to the spinal nerve root. Images adapted from Marchiano [100].*

ral foramina, a good visualization of the spinal nerve root is needed. However, finding the exact position of the nerve root is difficult on conventional axial or sagittal MRI scans. We use two sagittal oblique structural T2-weighted MRI scans to accurately reveal the location of the neuroforamen, similar to Goodman et al. [60]. Based on a standard axial scan of the cervical SC, we prescribed a sagittal scan that is approximately parallel to the spinal nerve leaving the neuroforamen (see Figure 3.1B). To visualize the SC and spinal nerve root a second sagittal oblique scan perpendicular to the first one is acquired. This scan is aligned so that at least one slice is parallel to the nerve root (see Figure 3.1C).

The first oblique scan is then used to position axial scans so that one slice intersects with the spinal nerve. Figure 3.2 presents two scans acquired with this positioning. In Figure 3.2A one can clearly appreciate the neuroforamina between C4 and C7. Furthermore, in Figure 3.2B the spinal nerve root leaving the SC can be seen. Based on these scans we are able to accurately position the DWI scans with respect to the root anatomy. We assume that the diffusion parameters differ mostly between P1 and P2, i.e. the positions shown in Figure 3.2C, where P1 coincides with the level of the spinal nerve root leaving the SC and P2 with the vertebral body.

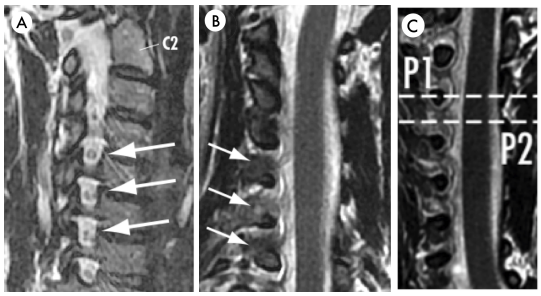

Figure 3.2: *Example slices of the two sagittal T2w oblique scans from one example subject. (A) The first sagittal oblique scan showing the neuroforamina of C4–C7 (white arrows). (B) The second oblique scan visualizing the spinal cord with the spinal nerve roots connected though the the neuroforamen (white arrows) (C) Positioning of the two DW axial scans based on the location of the spinal nerve roots.*

Table 3.1: *Gradient directions for DTI acquisition. Lines marked with ∗ are used for $ADC_\perp$ reconstruction.*

	*	*	*			*	*		*		*	*
g_x	0	0	1	0	1	0	-1	0	1	-1	-1	0
g_y	0	0	1	1	0	0	-1	1	-1	0	1	0
g_z	0	0	0	1	1	0	0	-1	0	1	0	0

3.2.2 Data acquisition

Diffusion-weighted scans are acquired on a 1.5T Signa scanner (General Electric Company, Milwaukee, WIS) using a four-channel phased-array spine coil. A cardiac-gated single shot Zonally oblique multislice (ZOOM) Echo-Planar Imaging (EPI) sequence [42] was set up with the following imaging parameters: repetition time (TR) = 5RRs, echo time (TE)= 95.5ms, voxel size = 1×1×5$mm^3$and an image matrix of 64×64 with a field-of-view (FOV) of 13×13mm^2. After acquisition, all magnitude images are linearly interpolated to a 128×128 matrix on a slice-by-slice basis resulting in an in-plane resolution of 0.5×0.5 mm^2.

We acquire 8 distributed diffusion weighted directions (see Table 3.1) interleaved with 4 non-diffusion weighted directions. A b-factor of 1000 s/mm^2 was chosen for optimal Diffusion Tensor (DT) reconstruction as recommended in Jones et al. [72] for white matter fibres. We focus attention on a single-slice acquisition to make sure that the signal from the slice is completely recovered after each shot, given that, when using the ZOOM sequence, T1 relaxation can affect the signal intensity of subsequent slices in multiple-slice acquisition. Also, by positioning one single slice, it is possible to acquire a SC image orthogonally to the main SC fibre direction. To increase signal-to-noise ratio (SNR), we initially repeat each scan on each subject 22 times to determine the optimal number of averages needed. Subsequent scans on the same subject are repeated 15 times (see next section).

3.2.3 Data analysis

Registration: Due to the relatively long scan time (30 – 40 minutes for 15 signal averages) the subject's position in the scanner is very likely to be affected by motion during the scan. However, registration of SC diffusion data is challenging for several reasons. First of all, diffusion-weighted images typically suffer from low SNR and low tissue contrast especially in the SC. Furthermore, in contrast to the brain, distortion artifacts from surrounding tissue and breathing motion make it difficult to identify reliable anatomical landmarks in the b=0 images. Moreover, longitudinal symmetry of the SC makes it impossible to correct for motion in this direction. Because of all these confounding factors, we use a restrictive motion model that only corrects for in-plane translation and assumes no movement in longitudinal foot-head direction. We divide data acquired within and between repetitions in different blocks with respect

to the interleaved b=0 acquisitions. Each block starts with one b=0 image and contains all DW images up to the next b=0 acquisition. We then co-register two subsequent b=0 images using the VTK CISG registration toolkit [65]. The resulting transformation is then applied to all the images in one block. After registration, we average all scans with corresponding diffusion weighting from subsequent repetitions and all the b=0 acquisitions individually and perform the diffusion parameter estimation on the averaged dataset as described below.

DTI analysis: DT reconstruction is performed using the open-source Camino tookit [37] and maps of the fractional anisotropy (FA) and radial diffusivity (RD) are calculated from the DT. In addition we use an alternative method of measuring diffusivity in the axial plane ($ADC_{\perp}$) from only the 4 co-planar acquisitions with diffusion gradients perpendicular to the SC as described by Fasano et al. [51]. The used diffusion directions are marked "*" in Table 3.1). All calculations are implemented in MATLAB (Mathworks, Natick, MA). We include the $ADC_{\perp}$ method as it requires no measurements parallel to the fibre. Therefore the number of scans needed for reliable measurements is significantly reduced compared to a DTI acquisition, which can be extremely beneficial for future studies of SCI patients.

ROI analysis: FA, RD and $ADC_{\perp}$ are quantified over the whole SC at each position. We semi-automatically segment the cord area on the average b=0 image of each slice using ImageJ[1] and the YAWI2D[2] segmentation plug-in. Due to the small size of the cord and the limits in image resolution, the segmented area will inevitably contain contributions from the surrounding cerebro-spinal fluid (CSF). Previous studies have shown that this partial volume significantly affects estimated diffusion parameters [2, 122]. To minimize this effect, we applied a binary erosion filter on the regions of interest (ROIs). This removes pixels at the edge of the ROI and thus allows removing voxels with CSF contribution from the ROI analysis. Hereby the thickness of the removed edge is dependent on the size of the structure element that is used for the erosion filtering. Figure 3.3 illustrates the effect of the size of the structure element on the estimated diffusion parameters in one subject. It can be seen that in the initial segmentation, FA is underestimated and diffusivity measurements are overestimated respectively because of the isotropic free diffusion that is present in the voxels with CSF contribution. A structure element of size 2 proves to be sufficient to eliminate the partial volume effect and all measurements reach a stable plateau.

Signal averaging: It is well known that in the low SNR regime the diffusion indices are very prone to estimation errors (see e.g. [71, 89, 123]). Thus, for reproducible measurements we need to acquire a sufficient number of averages in each scan. To determine the optimal number of averages for each subject we repeat the diffusion measurements at both slice positions 22 times each

1 www.imagej.com
2 yawi3d.sourceforge.net

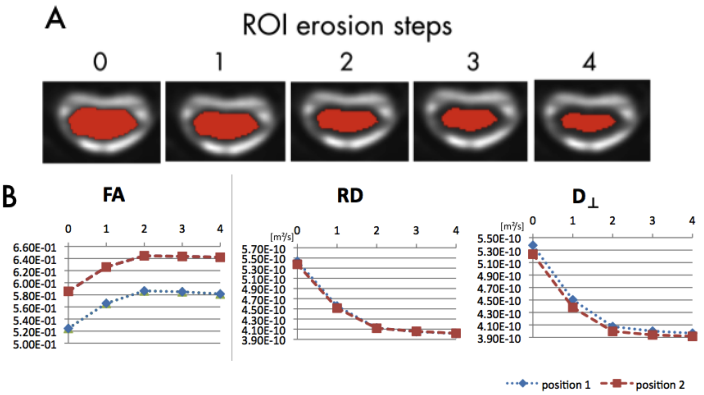

Figure 3.3: *Effect of erosion of the ROI on measured parameters in one representative subject. (A) Illustration of the initial segmented ROI in one slice and the ROIs after erosion with structure elements of size 1-4. (B) Mean FA, RD and ADC$_\perp$ observed in the eroded ROIs.*

(overall scan time was approx. 1h). We then calculate the diffusion indices described above using a subset of the first N repeated measurements with N increasing from 1 to 22. A plot of mean diffusion indices over the SC against the number of averages is presented in Figure 3.4 for one representative subject. A significant bias can be observed in all diffusion indices when less than 10 averages are used. After 15 repetitions none of the parameter estimates show noticable improvements, so we choose the number of averages to be 15 in all subsequent scans.

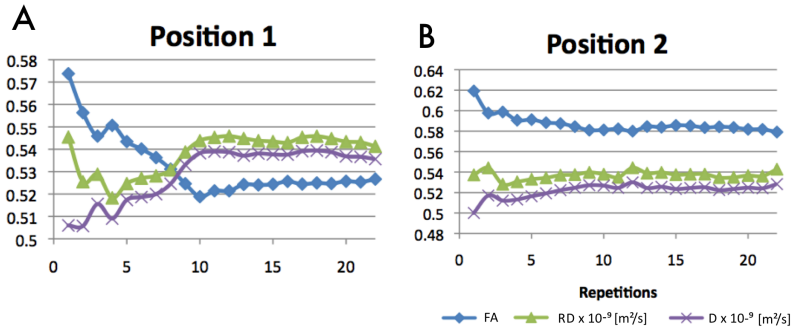

Figure 3.4: *Plot of diffusion indices FA, RD and ADC$_\perp$ against number of averages. (A) shows the averaged diffusion parameter at nerve-root level (B) shows mean parameters at the level of the body.*

3.2.4 Pilot study

A pilot study was carried out on 4 healthy female subjects. For each subject, parameter maps of FA, RD and ADC$_\perp$ were calculated as described above. We also calculated colour-coded maps of $\vec{v}_1, \vec{v}_2, \vec{v}_3$ for each scan. To assess intra-subject scan/rescan reproducibility, the scans were repeated with the same parameters after 5–7 days. Reproducibility of parameters was assessed by com-

Table 3.2: *COV of estimated parameters in all 4 subjects at both positions calculated from scan/re-scan experiment.*

	FA		RD		$ADC_{\perp}$	
	P1	P2	P1	P2	P1	P2
Subject 1	0.3%	9.9%	3.6%	8.0%	5.2%	8.5%
Subject 2	11.9%	1.0%	6.6%	4.2%	7.7%	3.6%
Subject 3	3.8%	2.9%	2.9%	5.7%	3.8%	3.3%
Subject 4	4.7%	8.1%	1.2%	3.4%	2.4%	2.4%

puting the coefficient of variation (COV) that is defined as the ratio of the standard deviation σ and the mean μ.

3.3 Results and Discussion

3.3.1 Scan/rescan reproducibility

Table 3.2 shows the COV of all measured parameters in all four subjects. It can be seen that our careful approach towards positioning and analyzing the data allows good reproducibility (COV < 10% in all but one case) in the scan/rescan experiment among all subjects. Furthermore, it should be noted that parameter variation seems to be slightly elevated in the $ADC_{\perp}$ parameter compared to RD.

3.3.2 Single subject position dependency of measured parameters

Figure 3.5 compares the measured diffusion parameters between the two investigated positions in all subjects. FA, RD and $ADC_{\perp}$ are closely dependent, i.e. when FA is low, RD and $ADC_{\perp}$ values are high and increasing FA corresponds to lower RD and $ADC_{\perp}$ in both positions. This implies that parallel diffusivity in the nerve fibres is position independent and therefore changes of FA between SC levels can be explained by different diffusivities perpendicular to the SC axis. Furthermore, it can be seen that the two methods of measuring diffusivity cross-sectionally give similar values in all subjects through the entire section of the cord, apart from minor differences in their standard deviation. This can be explained by the lower number of only 4 diffusion measurements that are used to reconstruct $ADC_{\perp}$, compared to the 8 diffusion directions used for full DT reconstruction.

3.3.3 Between subjects comparison of position dependency of parameters

Although in individual subjects we can see differences between position 1 and 2 with little variation in parameters between scan and rescan, we find that these trends are not consistent between subjects. In subject 1 and subject 3 we observe lower RD/$ADC_{\perp}$ and higher FA at nerve root level compared to the vertebral body (see Figure 3.5). Subject 2 shows an opposite trend at spinal

root level with higher FA and lower RD/ADC$_\perp$ respectively. In subject 4 there appear to be no differences between the two positions. It is unclear whether these differences between subjects can simply be explained by normal variation due to physiological noise or if they can be attributed to different fibre architecture in each individual. However, these differences between subjects also become apparent in the direction of the second eigenvector. In fact, it has been shown before that the second DT eigenvector is sensitive to the presence of sprouting fibres in the SC [98].

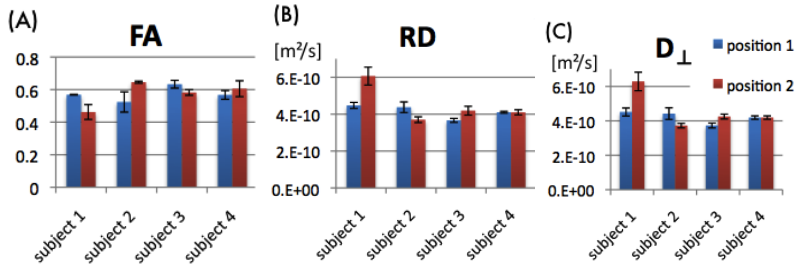

Figure 3.5: *Measurements of FA, RD and ADC$_\perp$. Blue bars represent mean of measurements at nerve root level, red represent the mean of measurements at mid-vertebra level. Black error bars display the standard deviation between scan and rescan.*

Figure 3.6 presents the color-coded maps of $\vec{v}_2$ overlaid on the FA map for two subjects with differing trends in diffusion parameters. Figure 3.6A displays $\vec{v}_2$ of subject 2, Figure 3.6B presents the $\vec{v}_2$-map of subject 4. In both cases, the first row shows the result from the first scan while the second row shows maps derived from the rescan. The position of the slice in the second row (i.e. for the rescan) was chosen to correspond anatomically with the position of the slice in the first experiment presented in the first row. This was achieved using our 45° localization scanning method presented above and using a printout of the first scan positioning as reference.

Distinct patterns emerge in each subject in the directions of the second eigenvector and are consistent over the first and second scan, although the small number of DTI gradient direction in our acquisition limits the directional resolution of the estimated tensor (reflected in the unusual dominance of either L-R or A-P eigenvectors in Figure 3.6). Furthermore, in subject 2, where lower FA and higher RD and ADC$_\perp$ are present at spinal root level compared to mid-vertebra level, we also observe different patterns in position 1 and position 2. In subject 4, which shows no difference in mean diffusion parameters in P1 and P2, the $\vec{v}_2$ map is also similar in both positions. The same geometry is apparent in the repeated scans for both subjects. It has to be noted that a higher angular in-plane resolution of the diffusion gradient scheme would be needed to allow mapping real anatomical directions of the sprouting peripheral nerves. This, however, would increase the number of acquisitions needed and therefore further increase the scan time.

These preliminary findings suggest that the diffusion measurements in the SC depend indeed on the presence of sprouting fibres. However, the organization of those fibres seems to be varying between subjects and needs to be ad-

dressed. The consistency of the patterns at different slice positioning between scans within each subject is encouraging because it suggests that DTI parameters, and in particular RD/ADC$_\perp$, can be used in longitudinal studies to assess structural changes due to degeneration or regeneration of fibers. Table 3.2 shows the COV of all measured parameters in all four subjects. It can be seen that our careful approach towards positioning and analyzing the data allows good reproducibility (COV < 10% in all but one cases) in the scan/rescan experiment among all subjects.

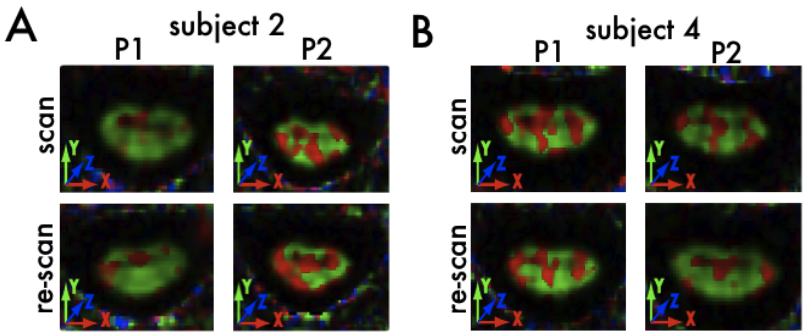

Figure 3.6: *Color coded second DT eigenvector overlaid on FA for two subjects. First row shows the first scan, second row the rescan of two subjects. First column shows values at spinal root level, second column shows mid-vertebra position.*

3.4 Conclusion

This study investigated the position dependency of diffusion parameters measured in the cervical SC at two distinct levels. We concentrated on optimizing the acquisition protocol and the analysis procedure to eliminate the various confounding effects, e.g. from uncertainty in slice positioning, presence of physiological noise and subject motion as well as parameter estimation errors from partial volume effect. Furthermore, we were able to find differences between the two investigated positions consistently reproduced within subjects. Studies using RD/ADC$_\perp$ measurements in the SC will have to take into consideration the inter-subject variability of these parameters.

4

Fuzzy partial volume weighting of average DTI metrics in the spinal cord

As seen in the previous chapter, Diffusion Tensor Imaging (DTI) in the spinal cord (SC) is usually affected by a large proportion of voxels that suffer from partial volume average (PVA) effects from surrounding cerebro-spinal fluid (CSF) due to the small size of the cord and the limited spatial resolution. While the effects of PVA on brain DTI have been studied extensively for over a decade, its effects on SC DTI are by far less well explored.

In the previous chapter we opted for a very conservative approach, excluding all voxels within the boundary of the SC, which drastically reduces the number of effective voxels for further analysis. In this chapter we present an alternative approach to region of interest (ROI) analysis of SC-DTI, which aims to reduce the PVA effect while it retains the information contained in boundary voxels.

4.1 Motivation

In the cord, a large proportion of voxels are usually affected by PVA from surrounding CSF due to the small size of the cord and the limited spatial resolution. Water molecules in CSF are less hindered than in nervous tissue, resulting in increased diffusivity measures and decreased anisotropy in PVA voxels, e.g. demonstrated by Alexander et al. [2], Metzler-Baddeley et al. [103], Pfefferbaum et al. [122], Vos et al. [152]. This can lead to biased average measurements over the whole cord volume and could potentially conceal subtle disease effects. PVA corruption can be dealt with by using CSF-suppressing pulse sequences such as fluid-attenuated inversion recovery (FLAIR) [31, 119]. However FLAIR has several disadvantages such as low signal-to-noise ratio (SNR) and high motion sensitivity, and, moreover, is unsuitable for cardiac gating due to its long inversion recovery preparation. As a consequence, FLAIR-DTI is not a viable alternative in the spinal cord.

PVA post-acquisition correction methods have been proposed that fit a combination of DTI and CSF compartments to the diffusion data as in Pasternak et al. [120], Pierpaoli et al. [124]. While these methods show promising results on brain DTI data, we found that they are not applicable to SC data due to the much lower SNR.

Therefore in common practice, CSF affected voxels are excluded from analysis with a subjective and manual editing of the outlined ROI. However, objectively deciding which voxels to exclude is difficult and might introduce an observer-specific error to the measurements. Furthermore retaining information while excluding those voxels can be problematic, particularly when the cord area is small and only few unaffected voxels exist, e.g. in patients with SC atrophy. We introduce a novel partial volume weighting method that attemps

to reduce the PVA effect on average DTI parameters that avoids the manual exclusion of PVA affected voxels. We propose a contribution weighting factor for each affected voxel that depends on its distance to the interface between SC voxels and CSF. We test our approach in healthy volunteers and patients with chronic spinal cord injury (SCI) and demonstrate that our method significantly reduces PVA effects on mean DTI indices.

4.2 Subjects and data acquisition

4.2.1 Subjects

The dataset we use in this study was acquired for a study of chronic SCI. The data consists of nine male SCI subjects (mean age=45.7 yrs, SD=10.3, range=29–61; n=9) who fulfilled the following inclusion criteria: (1) Bilateral upper and lower limb impairment; (2) No head or brain lesion associated with the trauma leading to the injury; (3) No seizure; no medical or mental illness; (4) no Magnetic Resonance Imaging (MRI) contraindications. Furthermore the dataset includes ten age- and gender-matched right handed healthy subjects (mean age=38.8 yrs, SD=15.5, range=25–65,) without any history of neurological or psychiatric illness.

4.2.2 Image acquisition

DTI was acquired on a 1.5T whole body Magnetom Sonata MRI scanner (Siemens Medical Systems, Erlangen, Germany) with a single shot echo planar imaging sequence employing the twice refocused spin-echo method for diffusion encoding [127]. Two axial datasets were collected using peripheral gating for reducing artifacts associated with cardiac induced gating motion [160]. The two datasets were also acquired with alternating phase encoding blip directions to remove susceptibility induced geometric distortions [5]. Each dataset consisted of 68 images with a low b-value of $100 s/mm^2$ for the first 7 images and a high b-value of $1000 s/mm^2$ for the remaining 61 directions. The diffusion encoding gradient directions were distributed evenly on the surface of the unit sphere [36]. The slice-to-slice repetition time was $180 ms$, the echo time was $90 ms$ and the excitation flip angle was 90°. The image volumes consisted of 20 axial slices with thickness of $5 mm$ and an in-plane resolution of $1.5\ mm^2$, with no inter-slice gaps, acquisition matrix of 96×96, field of view of $144 \times 144 mm^2$, and bandwidth 1408 Hz/Pixel. The large field-of-view (FOV) was necessary to avoid wrap-around artifacts from surrounding shoulder and neck tissue.

Interleaved slice sampling was chosen to avoid cross talk between adjacent slices. The acquisition was pulse triggered and took approximately 20 mins. The two datasets with different phase encoded directions were combined into a single dataset with reduced susceptibility induced geometric distortions as described in Andersson et al. [5]. Then, all volumes in image space were sinc interpolated to a 192×192 image matrix, resulting in an in-plane resolution of $0.75 mm^2$.

4.2.3 Data analysis

The diffusion tensor model was fitted to the interpolated data on a voxel-by-voxel basis using the freely available Camino toolkit [37]. Before further processing, all images were manually checked for remaining artifacts. The DTI dataset of one control subject had to be excluded from further analysis due to distortion artifacts. From the estimated tensor, fractional anisotropy (FA), radial diffusivity (RD), axial diffusivity (λ_1) and mean diffusivity (MD) maps were calculated for each subject. For each we also computed the mean $b = 100s/mm^2$ and performed a semi-automatic spinal cord segmentation on the image using the active surface segmentation implemented in Jim6 [68].

4.3 Fuzzy partial volume weighting method

We propose a novel method that computes the average over the DTI metrics by using the morphology of the initial spinal cord segmentation. By definition, the boundary voxels of the SC are most affected by the PVA effect, while voxels in the center remain unaffected. We can exploit the simple outline of the SC and compute the distance map of the initial segmentation using binary morphology operators [132]. This operation computes the minimal distance d to the border in each voxel. An example of a distance map of the spinal cord segmentation is shown in Figure 4.1.

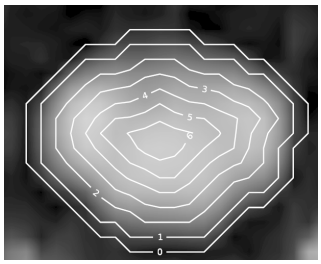

Figure 4.1: *Isolines of distance map of SC segmentation overlayed on FA map in one slice of one control subject.*

A clear relationship between the normalised distance $\hat{d} = d/\max(d)$ and DTI parameters can be seen in both controls (Figure 4.2a) and patients (Figure 4.2b). These plots suggest a correlation between all DTI parameters and d for voxels close to the boundary. Voxels with high $\hat{d}$ appear uncorrelated and therefore unaffected by PVA. We observe decreased FA and increased MD and λ_1 and RD for low $\hat{d}$ values compared to higher $\hat{d}$ values. It is important to note that the PVA effect is not only observed in the immediate boundary of the segmented SC but also affects voxels close to the boundary $\hat{d} < 0.3$. A possible explanation is that the observed PVA here originates not only from the the presence of multiple tissue types in a single voxel, but is affected by additional factors such as additional segmentation errors, movement, and blurring due to a large point-spread function.

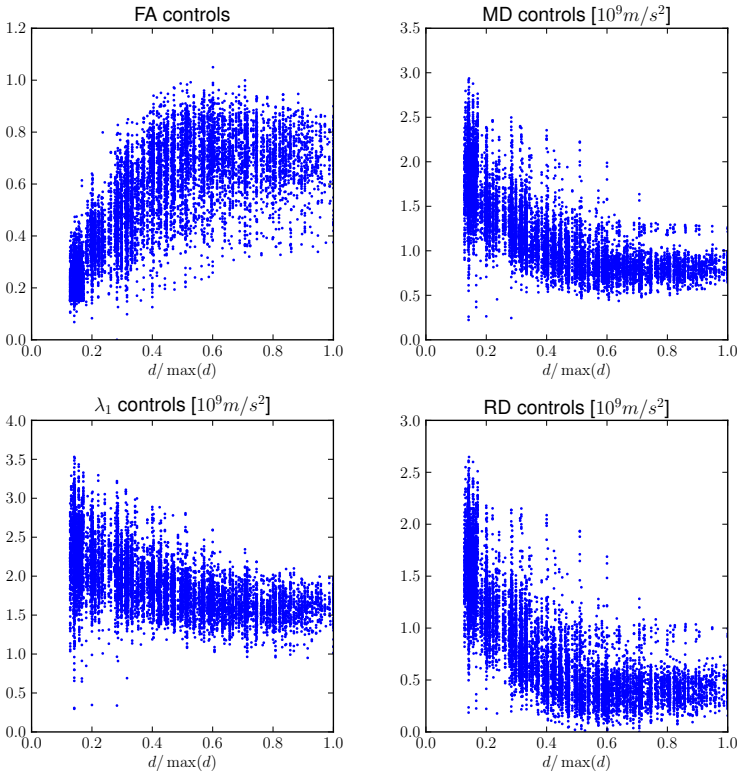

(a) Healthy controls

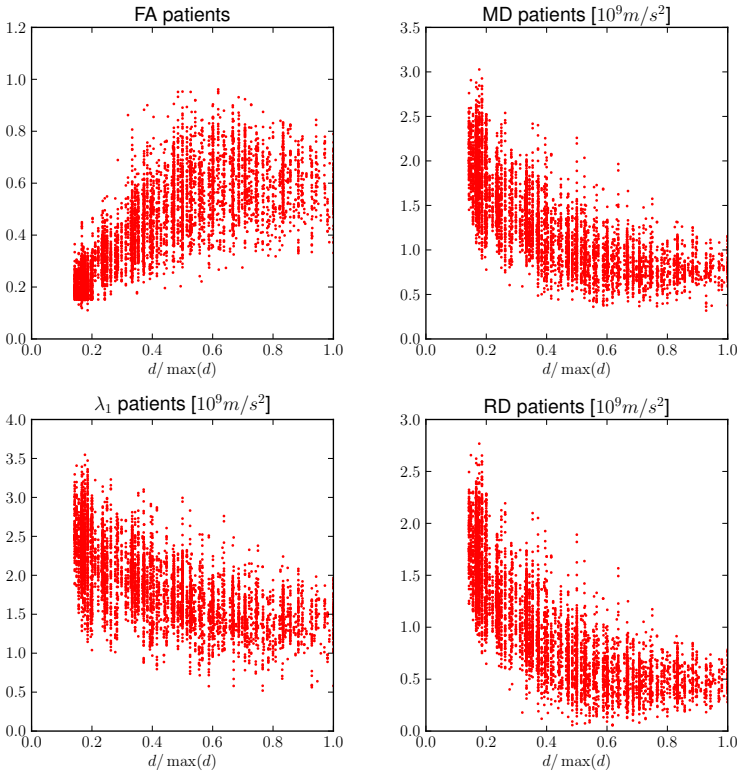

(b) SCI patients

Figure 4.2: *Scatterplots of normalised voxel distance $\hat{d} = d/max(d)$ against DTI parameters for controls and patient groups*

4.3.1 Weighting function

We aim to determine a weighting function that reflects the confidence in each voxel whether it belongs to the spinal cord tissue or not. We identified the criteria for a suitable candidate weighting function as follows:

1. Voxels closer to the boundary are assigned less confidence, i.e. are weighted less than voxels close to the centre
2. After a certain cut-off distance, voxels are assumed to be within the spinal cord
3. Boundary voxels are weighted less in larger spinal cord volumes than in small spinal cord volumes.

As stated above, criteria 1 and 2 are inferred directly from the observations made in both control and patient groups in Figure 4.2. Criterion 3 is included because of the relation between larger volume and increased PVA as shown, e.g. by Pasternak et al. [120]. We choose the weighting function $w(voxel)$ that fulfills all criteria above as:

$$w(voxel) = \begin{cases} d/\max(d) & \text{if } d \leq c \\ 1 & \text{otherwise} \end{cases}, \tag{4.1}$$

where c is a given cutoff distance and d is the distance of a voxel to the boundary as defined earlier. Figure 4.3 gives a graphical representation of the chosen weighting function $w(voxel)$. We chose a linear weighting because the monotonous relationship between distance and PVA in voxels with small d as seen in Figure 4.2 while it is also easy to interpret and implement.

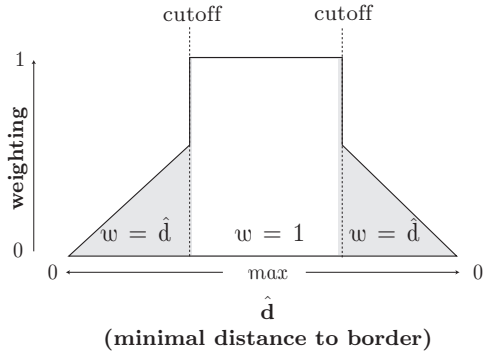

Figure 4.3: *1-d illustration of weighting function defined in Eq. 4.1.*

4.3.2 Data analysis

To determine the appropriate cutoff distance c we then apply the fuzzy weighted averages for the derived DTI parameters and compare them with the unweighted average. After the c is chosen, we compute the average differences between unweighted and fuzzy weighted whole ROI measurements in

Table 4.1: *Averaged relative change of Δmean and Δstandard deviation between non-weighted and PVA-weighted DTI measurements over all subjects.*

	controls		patients	
	Δ mean (%)	Δ std (%)	Δ mean (%)	Δ std (%)
FA	+21.6*	+30.0	+21.6	+37.2
MD	-19.2*	-25.8	-19.4	-19.2
λ_1	-8.6*	-26.6	-11.3	-12.4
RD	-31.0*	-15.2	-27.0	-19.8

*Significance p<0.01

controls and SCI patients for all DTI parameters, and also compute the unweighted and weighted histogram to compare the distribution of DTI values for both methods and both groups.

To quantify the difference between our method and the standard average, we test the statistical significance of the difference using a pairwise two-tailed t-test for control and patient groups independently. We also perform an unpaired two-tailed t-test on the differences between the two groups to investigate the influence of our method on the significance of group-wise changes between healthy subjects and chronic SCI patients. All statistical tests assume a confidence interval of 95%.

4.4 Results

4.4.1 Determining the cutoff distance

Our definition of the fuzzy weighting function (see Equation 4.1) requires the cutoff parameter c to be determined. This has to be done on the basis of the study specific protocol as image acquisition setup and postprocessing steps influence the dimensions of PVA. The isolines for the different values of c are illustrated in Figure 4.4 in a slice of one control subject. In Figure 4.5 and Table 4.2 we present average DTI metrics and standard deviations for different c in controls and patients. We observe higher diffusivity values and decreased FA in both groups for $c \leq 2$ compared to a larger value of c. For $c \geq 3$, the average metrics reach a plateau which can be clearly seen in Figure 4.5. Furthermore, the estimated average FA and diffusivities at $c \geq 3$ in the control group agree with previously reported values in healthy human cervical spinal cord [46, 159]. Based on these observations, we choose a cutoff value of $c = 3$ for this experiment.

4.4.2 Comparison of unweighted and fuzzy weighted average DTI metrics

Table 4.1 summarises the relative change in DTI metrics between the unweighted and PVA-weighted average DTI metrics. In both control and patient groups we observe significant differences between the unweighted and PVA-

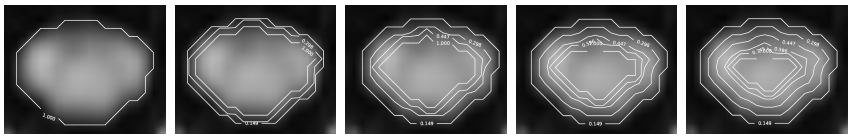

(a) standard average **(b)** $c = 2$ **(c)** $c = 3$ **(d)** $c = 3$ **(e)** $c = 6$

Figure 4.4: *Illustration of weighting isolines for different cutoff distances* $c \in \{0, 2, 3, 4, 5\}$ *overlayed on FA in one slice of one control.*

weighted averages. In RD we see the largest decrease of approx. 30% in both patients and controls. FA is increased by 22% and MD is reduced by 19% in both groups. We also find moderate but significant decrease in λ_1 by 10%. Furthermore we observe a reduction in the standard deviation of the diffusivities between 10% in λ_1 and 25% in MD and RD. In contrast, the variability in FA increases by more than 30% on average in both controls and patients compared to the unweighted average. However, the absolute standard deviation is low in both unweighted and fuzzy weighted averages (see Table 4.2).

Table 4.2 lists the statistical significance of the group-wise differences between controls and SCI patients for the unweighted whole SC average and the fuzzy weighted averages for all DTI parameters. FA are significantly different between both groups (p<0.01) independent of the analysis method. The λ_1 and MD values show no significant differences (all $p > 0.05$). The PVA weighting had most effect on the group-wise difference of RD: significance was decreased from $p = 0.04$ between unweighted averages to $p = 0.02$ in weighted average with chosen cutoff parameter $(c = 3)$.

Figure 4.6 presents histograms of all measured DTI parameters over all voxels of all control subjects and patients respectively. In each figure we present the normalised unweighted and fuzzy weighted histogram. In FA we see clear peaks at 0.7 (controls) and 0.6 (patients) in the fuzzy weighted histogram. In comparison FA values in the unweighted histogram are skewed towards low values in both patients and controls, both showing high peaks around 0.2. Peak position in the histograms of the diffusivity parameters are similar in unweighted and fuzzy weighted histograms, but the unweighted histograms show broader peaks and the distributions are generally more skewed towards high diffusion coefficients.

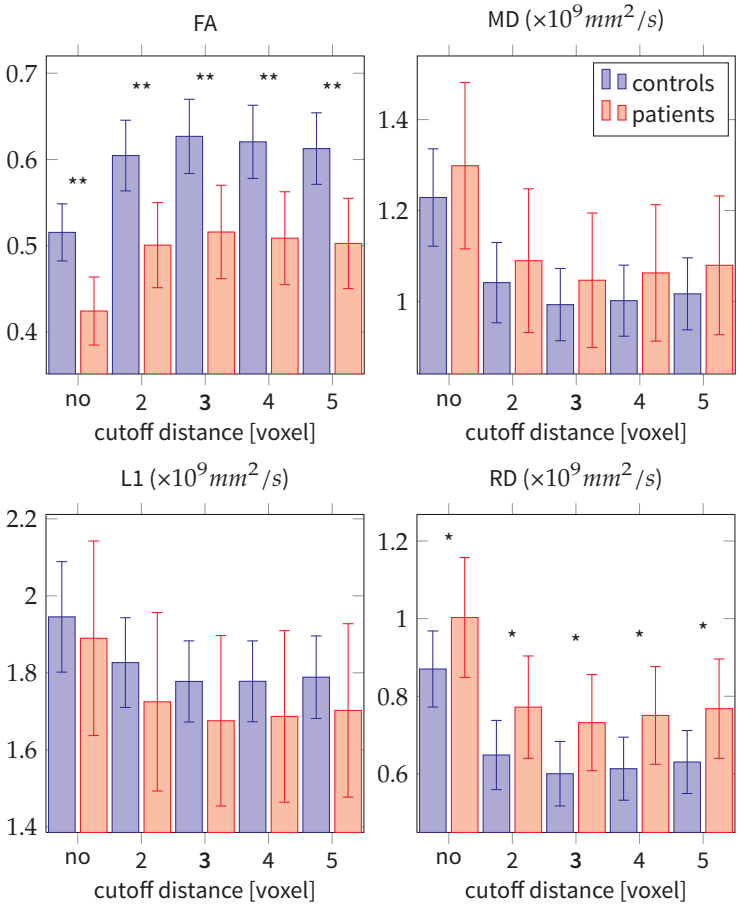

$^{*}p < 0.01, {}^{**}p < 0.05$

Figure 4.5: *Weighted mean and standard deviation of DTI parameters over all controls/-patients with respect to chosen cutoff distance. The chosen cutoff distance $c = 3$ is is marked bold in all figures.*

Table 4.2: *Mean and standard deviation of DTI parameters for controls (con) and SCI patients (pat) with respect to chosen cutoff distance c. The column of the chosen cutoff distance $c = 3$ is marked red. Statistical significant differences between healthy controls and SCI patients are marked with $^{*} * p < 0.01$, $^{*}p < 0.05$.*

		FA		MD		λ_1		RD	
		con	pat	con	pat	con	pat	con	pat
c=0	mean	0.52	0.42	1.23	1.30	1.95	1.89	0.87	1.00
	std	0.03	0.04	0.11	0.18	0.14	0.25	0.10	0.15
	p	**<0.01****		**0.33**		**0.57**		***0.04****	
c=2	mean	0.60	0.50	1.04	1.09	1.83	1.72	0.65	0.77
	std	0.04	0.05	0.09	0.16	0.12	0.23	0.09	0.13
	p	***<0.01*****		**0.42**		**0.24**		***0.03****	
c=3	mean	0.63	0.52	0.99	1.05	1.78	1.68	0.60	0.73
	std	0.04	0.05	0.08	0.15	0.11	0.22	0.08	0.12
	p	***<0.01*****		**0.34**		**0.22**		***0.02****	
c=4	mean	0.62	0.51	1.00	1.06	1.78	1.69	0.61	0.75
	std	0.04	0.05	0.08	0.15	0.11	0.22	0.08	0.13
	p	***<0.01*****		**0.28**		**0.27**		***0.01****	
c=5	mean	0.61	0.50	1.02	1.08	1.79	1.70	0.63	0.77
	std	0.04	0.05	0.08	0.15	0.11	0.23	0.08	0.13
	p	***<0.01*****		**0.28**		**0.30**		***0.01****	

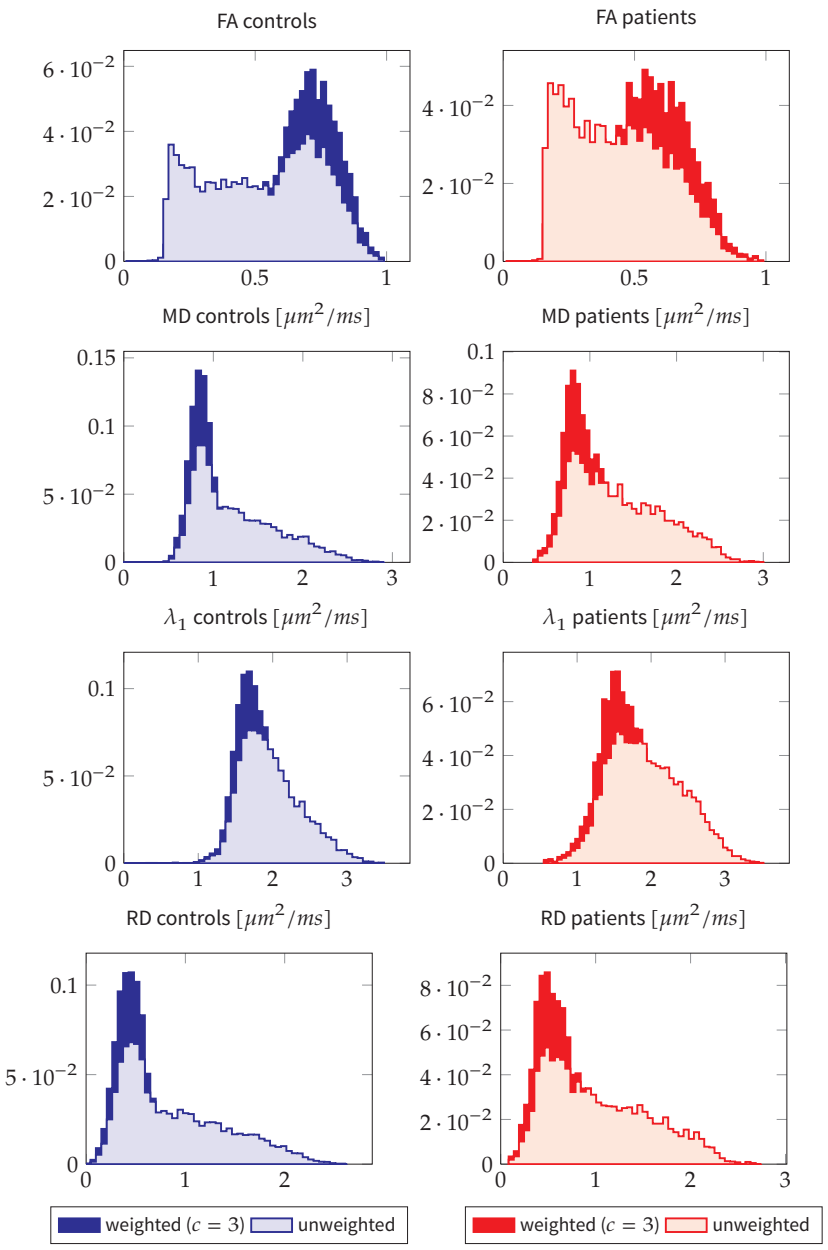

Figure 4.6: *Relative weighted and unweighted histogram of all DTI parameters for pooled SC voxels of controls (blue) and patient(red) groups.*

4.5 Discussion

We demonstrate the effect of PVA using DTI data of a cohort of 10 controls and 9 chronic SCI patients. We show that DTI metrics in the vicinity of the CSF/SC interface are affected and that there is a monotonous relationship between DTI metrics in a voxel and its distance to the border of the SC segmentation in our dataset. The significantly lower values of FA and higher diffusivities MD, λ_1 and RD suggest that these voxels suffer most likely from CSF contribution. These differences are expected from simulations [2, 120] and *in-vivo* brain experiments[122, 152], all of which agree that DTI parameters suffer considerably from CSF contribution.

Choice of cutoff value: We chose the cutoff parameters c depending on the average parameter over all DTI metrics in our control group. We chose the value that achieves a stable plateau in all DTI parameters, assuming that this reflects the elimination of CSF contribution. Although the value of $c = 3$ worked best in this study, we expect the optimal choice of c to be highly dependent on study specific parameters such as the choice of the pulse sequence, additional pre-processing steps and also the accuracy of the initial SC segmentation.

Effect of PVA weighting: The weighted distributions in Figure 4.6 show that our method diminishes the CSF bias in the measurements by reducing the artificial tails of the parameter distribution. Quantitatively, we observe a large reduction in RD, MD and FA parameters and smaller changes in λ_1. In agreement with earlier studies of the PVA effect in the brain, RD is reduced the most, while axial diffusivity (AD) is the least affected parameter. However, in contrast to those brain studies, we also observe a large change in FA. A possible explanation might be that the CSF contaminated voxels with low FA values have a bigger effect on the FA than in the brain due to much the smaller volume of the SC and therefore higher number of near-border voxels.

Group wise differences: We investigated whether our method affects group wise statistics between patients and controls in our study. FA and RD are both significantly diminished in weighted and unweighted metrics in SCI patients compared to controls. However, the PVA weighting increased the confidence in our results, particularly in the RD metric, which may help to detect more subtle changes e.g. in Multiple Sclerosis.

4.6 Conclusion

We propose a novel fuzzy partial volume weighting method that reduces CSF contribution effects in measurements of DTI parameters over the whole spinal cord volume. We emphasise the aspect of avoiding the full exclusion of potentially CSF contaminated voxels. Instead we introduce a weighting factor that is dependent on the size of the cord and therefore accounts for the variability in number of white matter voxels. We show that our method produces reli-

able DTI metrics that agree with previously measured values in the cord. We demonstrate that this method increases significance of group differences between SCI patients, i.e. can potentially increase the statistical power of larger clinical studies.

Application to clinical study: The method we developed was applied in a more clinically relevant context and was recently published in the PLoS One in 2012. The full text of the paper is presented in Appendix A and showcases the PVA weighting method we have developed here in a real application set-up. The work presented in that paper was carried out with equal contribution from Dr. Patrick Freund (Wellcome Trust Centre for Neuroimaging, University College London/Balgrist Spinal Cord Injury Center, Zürich), who recruited the healthy controls and patients and performed the clinical assessment, and myself, who performed the data processing and the majority of the analysis. The paper itself was jointly written by myself and Dr Freund with additional help from the other collaborators.

4.7 Limitations and future work

In this study we attribute changes in DTI parameters exclusively to the PVA effect. This is clearly an oversimplification as several other factors such as field inhomogeneities and field strengths may have an impact on the observed effect. The influence of the PVA will differ across different scanners/coils/centres. As a consequence, the cutoff parameter we found optimal for our study will reflect the influence of all these parameters to some extent, so care has to be taken when using this method to compare datasets that come from different scanners or are acquired with different protocols.

Further work is needed to validate this method against other PVA correction methods. Although validation is challenging due to a lack of ground truth value, in future work we might compare our results with fully CSF suppressed measurements, e.g. by using the FLAIR DTI technique [31, 119], although this technique also suffers from the lack of cardiac gating and lower SNR. Furthermore, a larger systematic study is needed to study the effect on the statistical power of our weighted method, compared to full exclusion of PVA affected voxels.

It is important to point out that in this experiment we don't correct for partial volume effects between grey and white matter inside the cord. This is mainly because the lack of contrast between gray and white matter on the low-b value images does not allow grey and white matter segmentation. Furthermore, our approach uses only macroscopic morphological *a-priori* knowledge of the spinal cord. The method is likely to fail if there is no clear relation between the morphology, i.e. voxel distance to border and present PVA effect.

Under certain circumstances, our method might also bias the average DTI whole cord parameters towards values found in the gray matter, since the downweighted voxels will be located only in the white matter of the cord. This lies in the nature of any morphological correction method, including also the

common mask erosion method. The bias will be elevated with increasing values of c. In this method, we tried to tackle this issue by adjusting the weighting by the overall size of the cord to include more weighting of potentially contaminated white matter (WM) voxels when the cord is small. However, a potential bias must always be considered when interpreting the PVA corrected whole cord parameters, especially when comparing healthy controls and patient cohorts as the bias might conceal genuine disease effects.

Future extension of this method could combine the morphological approach with diffusion models that account for CSF contribution in the raw DTI signal [120, 124]. By using the combination of macroscopic and microscopic information we can potentially overcome the limitation of the modelling approach in the low SNR regime in the spinal cord.

Part II

Q-space imaging studies

5

Tract-specific q-space imaging of the healthy cervical spinal cord (I)

In this chapter we investigate accuracy and sensitivity of spinal cord **q**-space imaging (QSI) metrics in healthy controls and evaluate its potential for clinical application. Previous studies of QSI on experimental MRI systems have shown that QSI can provide accurate information about microscopic restriction in excised tissue [7, 17, 112]. QSI requires an extensive sampling of different **q**-values along a single axis. This restricts the number of diffusion gradient directions that can be sampled when scan time is limited. While QSI application in the brain is limited by the need of high angular resolution of gradient directions to capture the variety of different fibre directions, this is less of a problem in the spinal cord (SC) due to its relatively simple white matter structure. However, the conditions for true QSI, such as the short gradient pulse, are impossible to achieve in clinical systems. Previous proof-of-concept studies have shown the great potential in the assessment of SC white matter and white pathologies in the human brain [10, 163] and in the spinal cord [50].

Following up on the encouraging results of these previous studies, we aim here to study the reproducibility of QSI metrics in the cervical SC on a standard 3T clinical MRI scanner. We also assess QSI measures both in-plane (XY) and parallel to the main SC axis (Z), not presented before. Previous work in *in-vitro* rat spinal cord by Ong et al. [112], Ong et al. [114] suggest that QSI parameters correlate with the axon diameter in different white matter regions. Our particular interest here is to explore whether clinical hardware constraints allow us to detect the structural differences between white matter (WM) and different ascending and descending WM tracts of the cervical SC with QSI. We test whether QSI can discriminate between WM tracts in the cervical in healthy subjects and compare conventional apparent diffusion coefficient (ADC) measures, both in plane and along the cord. Furthermore we also test whether any combination of QSI derived FWHM and P0 metrics can better distinguish between WM regions of interest (ROIs) than the individual metrics alone.

The next two chapters will present two QSI studies that both address the aims outlined above. This first chapter presents a study performed on 9 healthy controls, who were scanned at the Wellcome Trust Centre for Neuroimaging as part of a pilot study of microstructure changes in patients with complete brachial plexus avulsion [73] (and was also used to study a case of neuromyelitis optica (NMO)). Our preliminary findings in healthy controls were submitted for presentation at the Annual Meeting of the International Society for Magnetic Resonance in Medicine (Melbourne, 2013) and were accepted for oral presentation. Following the encouraging results in this first experiment, we re-implemented an improved protocol on the Philips 3T MRI scanner, that was newly installed in our lab. in 2010. The results of a second QSI pilot study using the new protocols comprise the next chapter (Chapter 6).

It should be noted that in all our QSI studies presented here, the short gradient pulse (SGP) is heavily violated, which, technically speaking, prohibits the application of the **q**-space formalism as defined by Callaghan [28] (see e.g. [80]). The term QSI is used here to describe the analysis pipeline associated with the **q**-space formalism, disregarding the known SGP violation. The theoretical and practical implications of this are discussed in general in Chapter 2 and specifically for this study at the end of this chapter and the following Chapter 6.

5.1 Methods

5.1.1 Study design

Twenty right-handed male healthy subjects were recruited (mean age 35$\pm$11yrs) to be scanned on a 3T Tim Trio (Siemens Healthcare, Erlangen). Six subjects were recalled for a second scan on a different day to assess intra-subject reproducibility of QSI derived parameters.

5.1.2 Data acquisition

In each subject we perform cardiac-gated high b-value axial Diffusion Weighted Imaging (DWI) (matrix=96×96, b-spline interpolated to 192×192 in image space, FOV=144 × 144 mm^2, slice thickness=5mm, 20 slices, TE=110ms, TR≈4000ms). The QSI set-up is based on parameters found in the most recent clinical QSI study [50]. However, our gradient system only allowed maximum diffusion gradient strength ($|G|$) of 23mT/m (Farrell et al. [50]: 60mT/m). To achieve similar **q**-values it was necessary to increase the gradient duration diffusion gradient pulse duration (δ) to 51ms. Reproduction of the protocol was further complicated by a limitation in the scanner software, which only permits a b-value to be specified in multiples of 50 mm/s^2, and means that **q**-values can not be exactly linearly spaced. We acquire a total of 32 b-values between 0-3000s/mm^2 in three different DWI directions: two directions perpendicular (XY) and one parallel (Z) to the main SC axis. The full protocol is given in Table 5.1.

After an initial quality check, we found that the prescription of the axial DWI slices varied greatly between different subjects. Figure 5.1 shows two representive cases for correct and incorrect positioning observed in the dataset. QSI is very sensitive to its alignment to the fibre direction, as shown e.g. in [12], and the variation in slice positioning might overshadow the subtle differences between WM we are interested in. We therefore measure the angulation between imaging plane and SC longitudinal axis as seen on a T2w sagittal scan at C2/C3. We excluded 11 subjects and their subsequent data where the angle was less than 80° (ideally we assume the axial images perfectly perpendicular, i.e 90°).

Table 5.1: *QSI protocol displaying: Gradient strength (G), $\mathbf{q}$-value (q) and b-value (b) for each of the 32 DWI volumes. The full protocol was split in two sub-session (left and right table), carried out immediately one after the other.*

G $[mT/m]$	q $[cm^{-1}]$	b $[s/mm^2]$	G $[mT/m]$	q $[cm^{-1}]$	b $[s/mm^2]$
0.0	0.0	0	0.0	0.0	0
3.0	56.2	50	3.0	56.2	50
4.2	79.4	100	4.2	79.4	100
5.1	97.3	150	5.1	97.3	150
5.9	112.3	200	5.9	112.3	200
6.6	125.6	250	7.8	148.6	350
8.4	158.9	400	9.4	177.6	500
9.8	186.3	550	10.7	202.5	650
11.5	217.5	750	12.2	231.6	850
12.9	244.8	950	13.9	263.4	1100
14.5	275.2	1200	15.4	291.9	1350
15.9	302.5	1450	16.7	317.7	1600
17.5	332.3	1750	18.2	346.2	1900
19.2	364.0	2100	19.9	376.8	2250
20.7	393.2	2450	21.3	405.0	2600
22.2	420.3	2800	22.9	435.1	3000

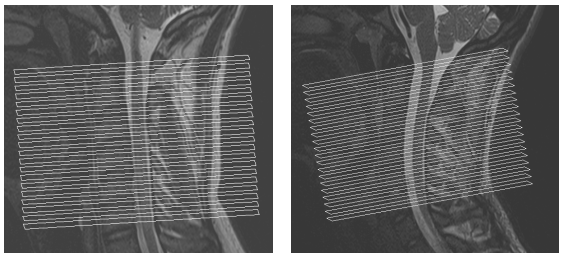

(a) Correct **(b)** Incorrect

Figure 5.1: *Examples of correct and incorrect positioning of QSI scans (displayed in white) overlayed on sagittal anatomical scans.*

5.1.3 Data processing

Similar to Farrell et al. [50], the two perpendicular diffusion directions were averaged to increase the signal-to-noise ratio. The measurements are linearly regridded to be equidistant in **q**-space and the diffusion probability density function (dPDF) is computed using inverse Fast Fourier Transformation. To increase the resolution of the dPDF, the signal was extrapolated in **q**-space to a maximum q=166mm^{-1} by fitting a bi-exponential decay curve to the DWI data as suggested in Cohen et al. [33], Farrell et al. [50]. Figure 5.2 illustrates the processing pipeline. Maps of the full width at half maximum and zero displacement probability were derived for XY and Z as described in Section 2.4.2. For comparison we also computed the ADC from the mono-exponential part of the decay curve (b < 1100s/mm^2) for both XY and Z directions using a constrained non-linear least squared fitting algorithm as suggested by Farrell et al. [50]. Figure 5.3 shows both ADC maps and the four QSI parameter maps in one randomly chosen subject.

5.1.4 ROI analysis

We semi-automatically delineate the whole cervical spinal cord area (SCA) between levels C1 and C3 on the b=0 images using the active surface segmentation by Horsfield et al. [68] available in Jim6. We perform a morphological erosion (2 iterations) of the obtained segmentation mask to exclude voxels with potential partial-volume average effect from surrounding cerebro-spinal fluid (CSF). In addition, four regions of interest were manually placed in specific white matter tracts and one ROI was positioned in the gray matter on all slices between level C1 and C3. The four white matter regions comprised the left and right tracts (l&r-LT) running in the lateral columns and the anterior (AT) and posterior tracts (PT) similar to Freund et al. [58], Hesseltine et al. [67] (see Figure 5.4). Figure 5.5 shows examples of signal curves and dPDFs derived in single voxels that are located in different regions of the cord.

5.1.5 Statistical processing

We compare scan/re-scan reproducibility by computing the absolute difference and relative difference in ADC and QSI parameters over the defined ROIs.

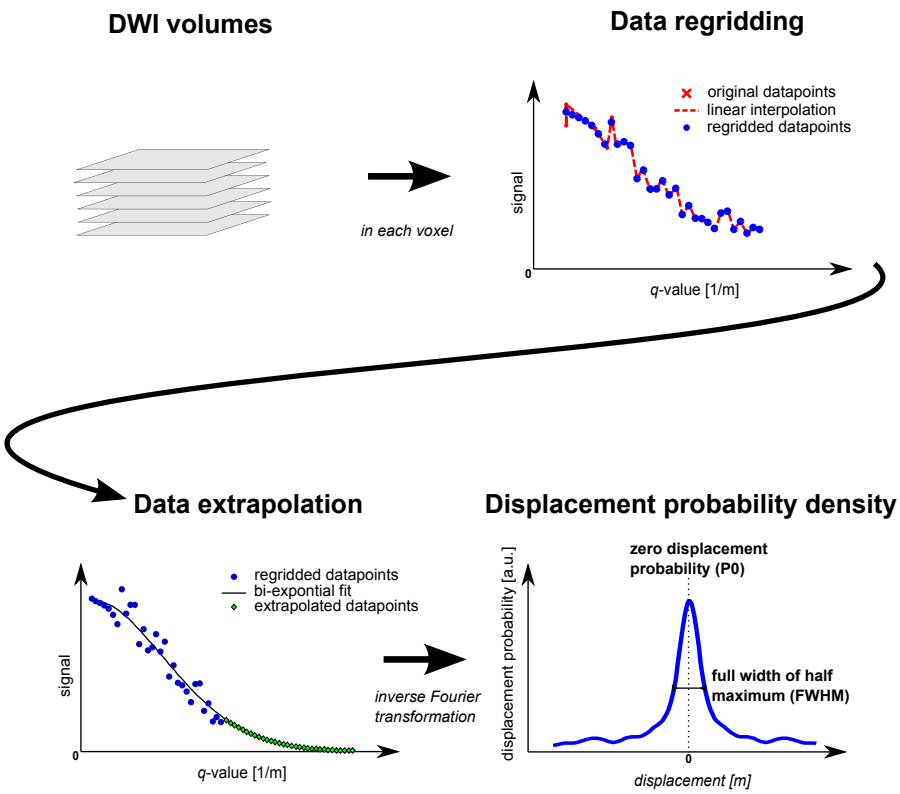

Figure 5.2: *Cartoon of the individual steps in our QSI processing pipeline.*

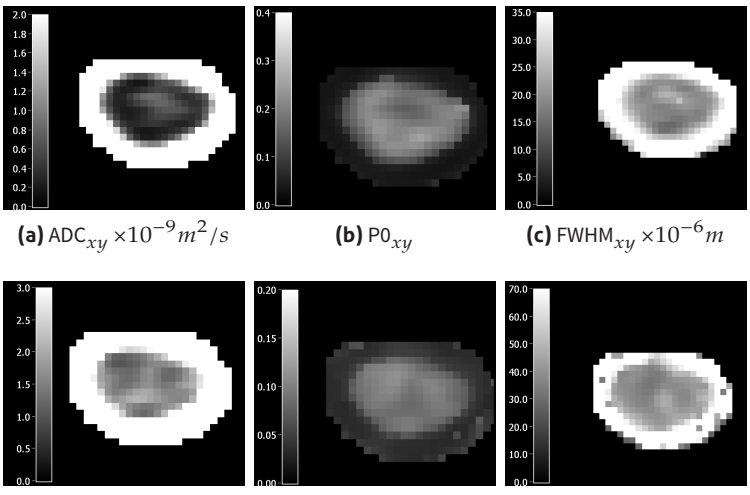

(a) ADC$_{xy}$ $\times 10^{-9} m^2/s$ **(b)** P0$_{xy}$ **(c)** FWHM$_{xy}$ $\times 10^{-6} m$

(d) ADC$_z$ $\times 10^{-9} m^2/s$ **(e)** P0$_z$ **(f)** FWHM$_z$ $\times 10^{-6} m$

Figure 5.3: *ADC maps and QSI parameter maps in one exemplary subject at the level of the C2–C3 disc.*

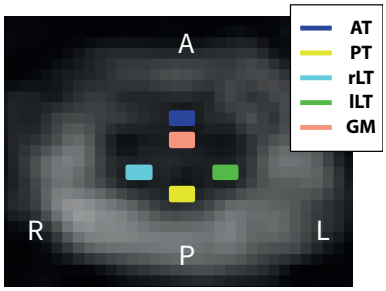

Figure 5.4: *Illustration of ROIs drawn on b=0 image.*

Further, we investigate the correlation between individual ADC and QSI measurements in XY and Z directions. We pool all voxel-wise measurements over the segmented SC area and compute Pearson's correlation coefficient over all voxels. We test for statistical significance of the correlations with a confidence interval of 95%.

We then compare significant differences in individual metrics using a paired two-tailed t-test and further investigate statistical significance in the group mean values of the ADC parameters and QSI metrics between tracts by performing the Hotellings-T^2 test (confidence interval=95%). To investigate the relevance of measurements in the different DWI directions, we compute the same significance test of XY-only QSI parameters ($P0_{xy}$, $FWHM_{xy}$) and compare with Z-only ($P0_z$, $FWHM_z$) and the combination of both ($P0_{xy}$, $FWHM_{xy}$, $P0_z$, $FWHM_z$).

5.2 Results

5.2.1 Reproducibility

Tables 5.2 shows absolute and relative differences between scan and rescan of three healthy subjects in ADC_{xy} and ADC_z and QSI metrics in XY and Z direction. We observe a general trend of measurements perpendicular to the long SC fibres presenting higher variation between scan and rescan than parallel measurements in ADC and both QSI metrics in all subjects. In particular ADC_{xy} shows very high intra-subject variation between 20–40% on average in all white matter ROIs, while only GM values show good reproducibility ($\approx$ 11% variability). In particular ADC_z appears more reproducible in all three subjects with average relative variation between 5–16%.

The perpendicular QSI metrics $P0_{xy}$ and $FWHM_{xy}$ present good reproducibility values of 6–12% and are up to 4 times lower than ADC_{xy} measurements in corresponding ROIs. In both $P0_z$ and $FWHM_z$ we observe relative change between 4–13% similar to values in ADC_z.

5.2.2 Differences between tract-specific ROI measurements

Figure 5.6 compares the average values and standard deviation over all 9 subjects between tract-specific for ADC and QSI metrics. As a general trend, we observe higher inter-subject variation in XY measurements compared to Z

Table 5.2: *Absolute and relative change (in percent) between scan and rescan of diffusivities and QSI parameters in 3 healthy volunteers*

(a) Perpendicular (ADC_{xy}) and parallel diffusivity (ADC_z)

$\mathbf{ADC}_{xy} \times 10^{-9} m^2/s$

subject	rLT	lLT	AT	PT	GM
1	0.10 (30.4%)	0.00 (4.7%)	0.07 (27.6%)	0.06 (24.1%)	0.09 (12.0%)
2	0.06 (16.9%)	0.06 (34.4%)	0.12 (44.6%)	0.03 (11.0%)	0.05 (12.0%)
3	0.09 (25.5%)	0.12 (51.9%)	0.24 (57.2%)	0.20 (82.5%)	0.04 (8.6%)
mean	0.08 (24.3%)	0.06 (30.4%)	0.14 (43.1%)	0.10 (39.2%)	0.06 (10.9%)

$\mathbf{ADC}_z \times 10^{-9} m^2/s$

subject	rLT	lLT	AT	PT	GM
1	0.04 (3.3%)	0.07 (4.7%)	0.18 (12.2%)	0.03 (2.1%)	0.03 (2.4%)
2	0.13 (9.0%)	0.17 (9.8%)	0.40 (23.2%)	0.03 (1.6%)	0.30 (16.9%)
3	0.16 (12.5%)	0.10 (6.2%)	0.21 (12.9%)	0.16 (10.2%)	0.28 (16.6%)
mean	0.11 (8.3%)	0.12 (6.9%)	0.26 (16.1%)	0.07 (4.7%)	0.20 (12.0%)

(b) Perpendicular and parallel QSI parameters

$\mathbf{P0}_{xy}$

subject	rLT	lLT	AT	PT	GM
1	0.01 (3.1%)	0.02 (6.8%)	0.01 (3.4%)	0.00 (1.7%)	0.00 (1.9%)
2	0.00 (0.4%)	0.00 (0.3%)	0.01 (4.3%)	0.01 (3.3%)	0.00 (2.3%)
3	0.01 (6.1%)	0.06 (28.2%)	0.04 (19.9%)	0.06 (26.7%)	0.03 (14.8%)
mean	0.01 (3.2%)	0.03 (11.8%)	0.02 (9.2%)	0.02 (10.6%)	0.01 (6.3%)

$\mathbf{FWHM}_{xy}$

subject	rLT	lLT	AT	PT	GM
1	0.52 (2.5%)	0.67 (4.8%)	0.67 (3.5%)	0.29 (1.5%)	0.62 (2.4%)
2	0.03 (0.1%)	0.29 (1.6%)	0.76 (4.1%)	0.36 (1.9%)	0.32 (1.5%)
3	1.10 (5.2%)	5.69 (29.6%)	4.72 (20.6%)	5.10 (27.5%)	3.29 (15.5%)
mean	0.55 (2.6%)	2.22 (12.0%)	2.05 (9.4%)	1.92 (10.3%)	1.41 (6.5%)

$\mathbf{P0}_z$

subject	rLT	lLT	AT	PT	GM
1	0.00 (4.5%)	0.00 (0.6%)	0.01 (6.9%)	0.00 (2.5%)	0.01 (5.6%)
2	0.01 (9.2%)	0.01 (11.4%)	0.01 (11.0%)	0.00 (3.4%)	0.01 (10.6%)
3	0.01 (6.0%)	0.00 (0.1%)	0.00 (1.2%)	0.01 (7.8%)	0.01 (14.9%)
mean	0.01 (6.6%)	0.00 (4.1%)	0.01 (6.3%)	0.00 (4.6%)	0.01 (10.4%)

$\mathbf{FWHM}_z$

subject	rLT	lLT	AT	PT	GM
1	1.42 (3.9%)	1.67 (3.9%)	4.20 (10.4%)	1.07 (2.7%)	3.86 (10.7%)
2	5.72 (15.4%)	9.04 (22.2%)	4.69 (11.6%)	4.47 (10.9%)	4.76 (12.5%)
3	1.08 (3.0%)	0.13 (0.3%)	1.66 (4.1%)	4.89 (12.4%)	6.17 (16.1%)
mean	2.74 (7.4%)	3.61 (8.8%)	3.52 (8.7%)	3.48 (8.6%)	4.93 (13.1%)

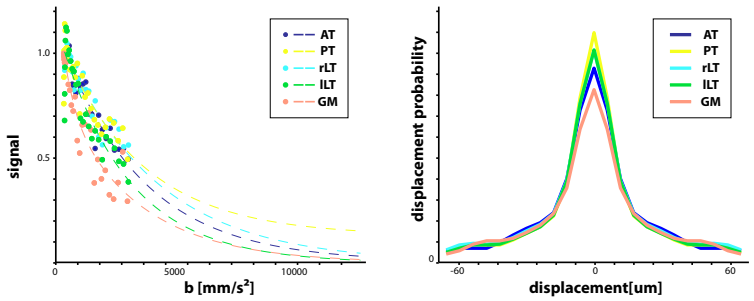

(a) Diffusion signal curves and derived PDF shapes for representative voxels in different tracts in XY direction.

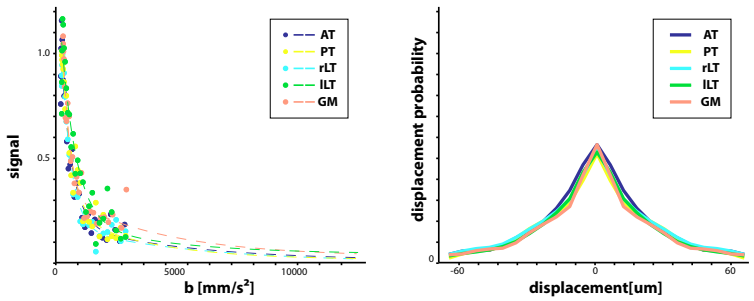

(b) Diffusion signal curves and derived dPDF shapes for representative voxels in different tracts in Z direction.

Figure 5.5: *Illustration of diffusion signals and dPDFs derived for different ROIs.*

measurements among all 9 subjects which is in line with our results of intra-subject variation shown above.

Table 5.3 present *p*-values for pairwise differences between different tract-ROIs for ADC and QSI metrics. The most notable differences are found between the GM ROI and the white matter regions in ADC_{xy} and both $P0_{xy}$/$FWHM_{xy}$ with high statistical significance ($p<0.01$ between WM tracts GM for all QSI_{xy} metrics), while ADC_z and QSI_z metrics are less different between GM ROI and WM ROIs. In fact, significant differences are only found between rLT and GM in ADC_z. The QSI_z metrics only show significant differences between GM and rRT in $P0_z$ ($p=0.01$) and between GM and AT and PT ($FWHM_z$).

Between WM ROIs only the left LT but not the right LT is significantly different from both AT and PT in ADC_{xy} perpendicular to long white matter fibres. Parallel to the long SC axis we only find ADC_z in the right LT significantly lower from AT and PT. Left and right LT show significant differences in both ADC_{xy} and ADC_z, while we find no difference between AT or PT. In QSI metrics we find the same tracts as with ADC to be significantly different in XY and Z direction. However, *p*-values are increased in QSI compared to corresponding ADC, but remain below $p<0.05$.

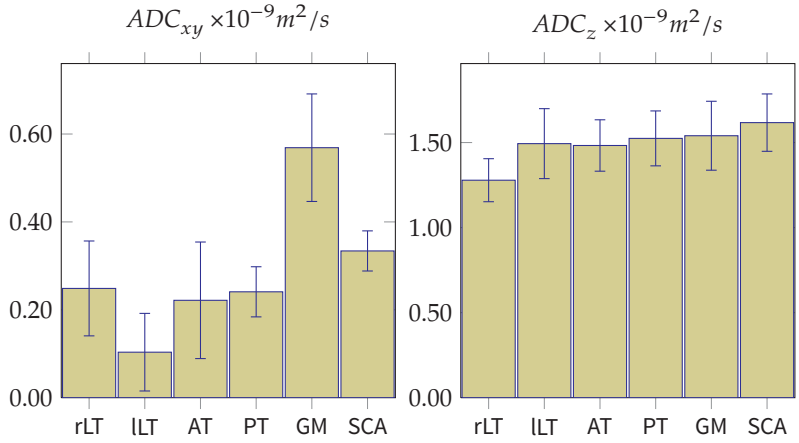

(a) Perpendicular (ADC_{xy}) and parallel diffusivity (ADC_z)

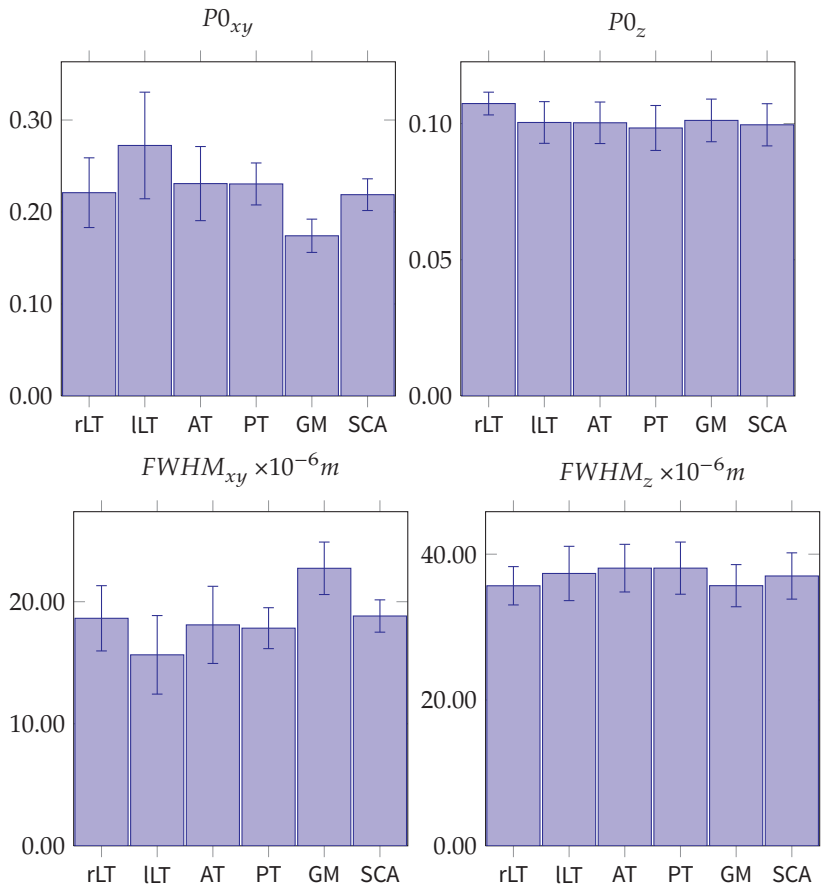

(b) Perpendicular and parallel QSI parameters

Figure 5.6: *Mean and standard deviation of perpendicular and parallel ADC and QSI metrics for all ROIs over all 9 volunteers.*

5.2.3 Multi-variate differences between tract-specific ROI measurements

The single parameter comparisons above indicate that both ADC and QSI metrics can discriminate some WM tracts, but offer complementary information in perpendicular and parallel measurements. The multivariate Hotelling's-T^2 test allows us to test whether a combination of XY and Z metrics is better suited to characterize and discriminate WM measures in different ROIs. Below we present results for the following combinations of parameters:

- Both diffusivity parameters ADC_{xy} and ADC_z (Table 5.4a)
- Perpendicular only QSI metrics $P0_{xy}$ and $FWHM_{xy}$ (Table 5.4a)
- Parallel only QSI metrics $P0_z$ and $FWHM_z$ (Table 5.4c)
- Perpendicular and parallel QSI metrics $P0_{xy}$, $FWHM_{xy}$, $P0_z$ and $FWHM_z$ (Table 5.4d)

Similar to the single t-test results shown above, GM and WM ROIs can clearly be distinguished using either of the combinations of ADC and QSI parameters. However, GM/WM differences are more pronounced in XY than in Z direction. The combined ADC metrics show significant differences between both the lateral tracts and also l/r LT and the posterior WM ROI. AT is only significantly different from the right but not the left LT.

For combination of QSI parameters in Z only, as well as the combination of both XY and Z, the only two emerging differences are found between lLT/rLT and rLT/PT, both with $p<0.05$.

Table 5.3: *Significance of pair-wise differences between SC tracts in diffusivities and QSI parameters (confidence interval: 95%). Statistically significant differences are marked as follows:* ***bold*** *if p<0.05,* **bold-italic** *if p<0.01.*

(a) Perpendicular (ADC_{xy}) and parallel diffusivity (ADC_z)

$ADC_{xy} \times 10^{-9} m^2/s$	lLT	AT	PT	GM
rLT	**0.01**	0.60	0.84	***<0.01***
lLT		***<0.01***	***<0.01***	***<0.01***
AT			0.56	***<0.01***
PT				***<0.01***

$ADC_z \times 10^{-9} m^2/s$	lLT	AT	PT	GM
rLT	**0.01**	***<0.01***	***<0.01***	***<0.01***
lLT		0.85	***<0.01***	0.57
AT			0.44	0.30
PT				0.74

(b) Perpendicular and parallel QSI parameters

$P0_{xy}$	lLT	AT	PT	GM
rLT	**0.04**	0.27	0.48	***<0.01***
lLT		**0.05**	0.48	***<0.01***
AT			0.97	***<0.01***
PT				***<0.01***

$P0_z$	lLT	AT	PT	GM
rLT	**0.01**	***<0.01***	***<0.01***	**0.01**
lLT		0.94	***<0.01***	0.77
AT			0.40	0.69
PT				0.16

$FWHM_{xy}$	lLT	AT	PT	GM
rLT	**0.04**	0.56	0.37	***<0.01***
lLT		**0.02**	0.37	***<0.01***
AT			0.72	**0.01**
PT				***<0.01***

$FWHM_z$	lLT	AT	PT	GM
rLT	0.21	**0.02**	**0.03**	0.99
lLT		0.20	**0.03**	0.13
AT			1.00	**0.01**
PT				**0.01**

Table 5.4: *Hotelling's-T^2 significance of pair-wise tract-specific differences for ADC and QSI parameters. (**bold** marks p<0.05,* **bold-italic** *marks p<0.01).*

(a) Combined ADC_{xy},ADC_z

	lLT	AT	PT	GM
rLT	***<0.01***	**0.02**	**0.01**	***<0.01***
lLT		0.10	**0.01**	***<0.01***
AT			0.85	***<0.01***
PT				***<0.01***

(b) Combined perpendicular QSI parameters ($P0_{xy}$,$FWHM_{xy}$)

	lLT	AT	PT	GM
rLT	0.13	0.79	0.71	**0.01**
lLT		0.26	0.12	***<0.01***
AT			0.76	**0.02**
PT				***<0.01***

(c) Combined parallel QSI parameters ($P0_z$,$FWHM_z$)

	lLT	AT	PT	GM
rLT	**0.03**	0.08	**0.02**	**0.02**
lLT		0.60	0.86	0.18
AT			0.49	**0.01**
PT				***<0.01***

(d) Combined perpendicular and parallel QSI parameters ($P0_{xy}$,$FWHM_{xy}$,$P0_z$,$FWHM_z$)

	lLT	AT	PT	GM
rLT	**0.04**	0.25	**0.01**	***<0.01***
lLT		0.62	0.50	***<0.01***
AT			0.75	***<0.01***
PT				***<0.01***

Table 5.5: *Pearson-correlation coefficient and significance between all ADC and QSI metrics. The p-values < 0.01 are marked bold-italic.*

		ADC_{xy}	ADC_z	$P0_{xy}$	$FWHM_{xy}$	$P0_z$	$FWHM_z$
ADC_{xy}	*r*		0.58	0.00	-0.74	0.20	0.01
	p		***<0.01***	0.91	***<0.01***	***<0.01***	0.56
ADC_z	*r*	0.58		0.00	-0.29	0.71	0.00
	p	***<0.01***		0.87	***<0.01***	***<0.01***	0.82
$P0_{xy}$	*r*	0.00	0.00		0.00	0.00	0.00
	p & 0.91	0.87		0.82	0.99	1.00	
$FWHM_{xy}$	*r*	-0.74	-0.29	0.00		-0.18	-0.01
	p	***<0.01***	***<0.01***	0.82		***<0.01***	0.70
$P0_z$	*r*	0.20	0.71	0.00	-0.18		0.01
	p	***<0.01***	***<0.01***	0.99	***<0.01***		0.52
$FWHM_z$	*r*	0.01	0.00	0.00	-0.01	0.01	
	p	0.56	0.82	1.00	0.70	0.52	

5.2.4 Voxel-wise correlation of ADC and QSI metrics

Table 5.5 shows the Pearson correlation coefficient *r* and statistical significance of the correlation between ADC and QSI parameters over all SC voxels in all subjects. We observe significant correlations between ADC_{xy} and ADC_z. Further we find significant correlations between and QSI parameters, both within and across XY and Z direction. Interestingly, we find both $FWHM_{xy}$ and $P0_z$ are correlated with each other and also with both ADC parameters, while the other two QSI parameters $P0_{xy}$ and $FWHM_z$ did neither correlate with each other nor any other metrics.

5.3 Discussion

QSI metrics obtained without sequence development, using a standard DWI protocol available on a 3T clinical scanner, show a good reproducibility that is superior to simple ADC analysis. We observe tract-specific correlations between ADC and QSI parameters between several WM tracts. However some of the associations in QSI metrics are weaker in XY compared to Z, particularly between lateral and posterior tracts. Together with the findings of weak correlation between QSI and ADC metrics in both XY and Z, our results suggest that the Z direction provides additional information to perpendicular measurements. Our results also suggest that on a clinical scanner QSI might not be able to reliably distinguish between individual WM tracts.

The results of this experiment need to be interpreted with caution due to the limitations in hardware and software in the experimental set up. In particular the low gradient strength used in this study might conceal differences between

tracts. Simulations by Lätt et al. [91] show that insufficient gradient strength might lead to overestimation of compartment size and suggest that gradients of at least 60 mT/m are required to be sensitive to the typical size of axons found in human WM. Beside the hardware limitations of the scanner, there are also several issues in the design of this study including:

1. the high number of subjects that had to be excluded due to misalignment of the axial images
2. the linear regridding that was made necessary because of scanner software limitation
3. the relatively high in-plane resolution of the acquired images

To overcome these flaws in the study design, the data had to undergo a rather extensive pre-processing pipeline, which might weaken the confidence in our results. The installation of a new 3T scanner in our lab offered us the possibility to repeat this experiment with improved hardware and software capabilities. The results are described in the following chapter.

6

Tract-specific q-space imaging of the healthy cervical spinal cord (II)

The aim of this study is to repeat the experiment in Chapter 5 and improve on the several confounding factors that we identified in the previous chapter. We carefully optimise the acquisition to achieve an increase in spatial resolution and signal-to-noise ratio (SNR) of the axial DWI measurements, and higher diffusion gradient strength, as well as linear spacing of **q**-values.

6.1 Methods

6.1.1 Study design

We recruit 10 healthy volunteers (4 male/6 female) to be scanned on a 3T Philips Achieva 3TX (Philips Healthcare, Eindhoven). Four subjects are re-scanned at a different time to assess intra-subject reproducibility of the derived parameters.

6.1.2 Data acquisition

To ensure consistent positioning of the DWI volumes among all scans, we acquire a structural scan of the whole cervical cord using a sagittal T2 weighted turbo-spin-echo sequence (voxel size=1×1×3 mm^3, FOV=256×247mm^2, TR=4000ms, TE=63ms, 2 averages). We then position the DWI volumes based on the structural scan so that the centre of the acquisitions volume is aligned with the C2/C3 disc and the acquisition plane is parallel to the cord at this level.

We use a cardiac gated DWI acquisition with the following imaging parameters: voxel size=1×1×5 mm^3, FOV=64×64mm^2, TR=9RR, TE=129ms). To avoid aliasing artifacts from surrounding tissue we use a ZOOM sequence with outer-volume suppression, as described by Wilm et al. [161]. We acquire 32 DWI equally spaced **q**-values in two directions perpendicular (XY) and in one parallel (Z) direction with respect to the main SC axis. To achieve the maximum possible gradient strength on our scanner, we exploit the combination of parallel gradient amplifiers in our scanner, which can each generate a maximum $|G|$ of 62mT/m along the major axes of the scanner bore. Assuming axial symmetry of the axons along the long axis of the spinal cord, we modify the scanner software to drive multiple gradient amplifiers in two orthogonal directions perpendicular to major SC fibre direction (see Figure 6.1 for illustration). This allows us to generate a guaranteed maximum $|G|$ of $\sqrt{2} * 62mT/m = 87mT/m$ in XY direction. In Z direction we use a maximum $|G|$ of 62 mT/m. We use the same **q**-values in this experiment as described by Farrell et al. [50]. However the increase in $|G|$ allows us to reduce the gradient

duration from 50ms to 11.4ms in XY direction (16ms in Z). The full protocol is given in Table 6.1.

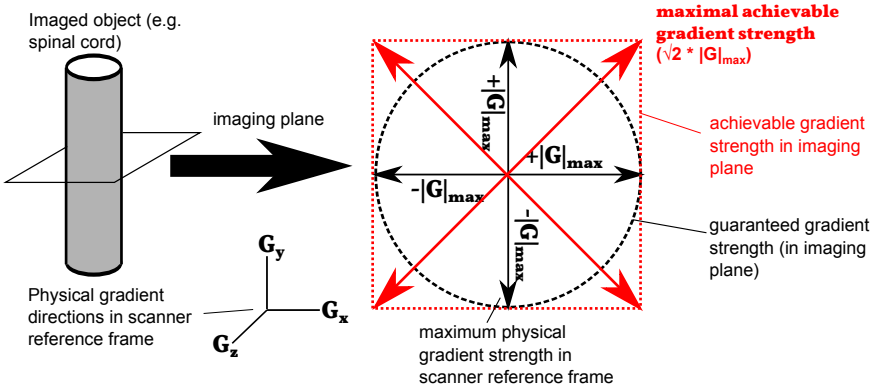

Figure 6.1: *Cartoon of our implemented gradient strength modification method.*

6.1.3 Data processing & analysis

We apply the same data processing pipeline as in the previous experiment (see Section 5.1) with the exception of the linear regridding of acquired **q**-values, which is not necessary in this data set. We segment the whole cervical SC and place ROIs in the lateral columns and the anterior and posterior tracts between level C1/2 and C3 in all subjects. Figure 6.2 illustrates the placement of the ROIs and representative dPDFs in XY and Z direction respectively.

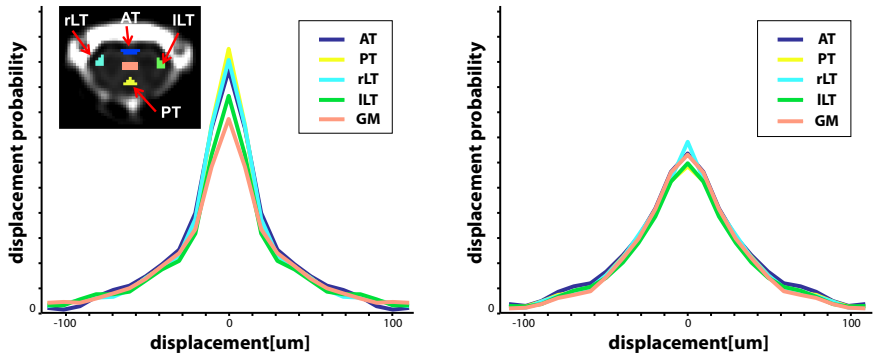

(a) DPDF shapes for representative voxels in different tracts in XY and Z direction.

Figure 6.2: *Illustration of diffusion signals and PDFs derived for different ROIs.*

6.1.4 Statistical processing

We derive the same statistics from this dataset as in the previous chapter. We present the absolute difference and relative difference in ADC and QSI parameters over the defined ROIs in the scan/re-scan cases. Further we show results of t-tests between different tracts for individual metrics and the multivariate Hotelling-T^2 test for combination of parameters. We also investigate

Table 6.1: *QSI protocol displaying: Gradient strength (G), $\mathbf{q}$-value (q) and b-value (b) for each of the 32 DWI volumes. The full protocol was split in two sub-session (left and right table), carried out immediately one after the other.*

(a) Protocol for X and Y direction

G $[mT/m]$	q $[cm^{-1}]$	b $[s/mm^2]$	*... continued* G $[mT/m]$	q $[cm^{-1}]$	b $[s/mm^2]$
0.0	0.0	0	0.0	0.0	0
5.8	66.2	22	2.9	33.0	6
11.7	132.8	90	8.7	99.2	50
17.5	198.6	200	14.6	165.7	139
23.3	264.5	355	20.4	231.5	272
29.1	330.3	554	26.2	297.4	449
35.0	397.3	802	32.1	364.3	674
40.8	463.1	1089	37.9	430.2	940
46.6	528.9	1421	43.7	496.0	1250
52.5	595.9	1803	49.5	561.8	1603
58.3	661.7	2224	55.4	628.8	2008
64.1	727.5	2688	61.2	694.6	2451
69.9	793.4	3197	67	760.5	2937
75.8	860.3	3759	72.9	827.4	3477
81.6	926.2	4357	78.7	893.2	4053
87.4	992.0	4998	84.5	959.1	4672

(b) Protocol for Z direction

G $[mT/m]$	q $[cm^{-1}]$	b $[s/mm^2]$	*... continued* G $[mT/m]$	q $[cm^{-1}]$	b $[s/mm^2]$
0.0	0.0	0	0.0	0.0	0
4.1	46.9	11	2.1	23.4	3
8.3	94.2	45	6.2	70.4	25
12.4	140.9	101	10.4	117.5	70
16.5	187.6	179	14.5	164.2	137
20.6	234.2	279	18.6	210.9	226
24.8	281.7	403	22.8	258.4	339
28.9	328.4	548	26.9	305.1	473
33.0	375.1	715	31.0	351.8	629
37.2	422.6	907	35.1	398.5	806
41.3	469.3	1119	39.3	446.0	1010
45.5	516.0	1352	43.4	492.6	1233
49.6	562.7	1608	47.5	539.3	1477
53.8	610.2	1891	51.7	586.8	1749
57.9	656.9	2191	55.8	633.5	2038
62.0	703.5	2514	59.9	680.2	2350

voxel-wise correlations between the six metrics using Pearson correlation coefficient.

6.2 Results

6.2.1 Scan/Rescan reproducibility

Table 6.2 shows the intra-subject variability for ADC and QSI metrics in all four subjects. In both ADC and QSI and all ROIs, the observed COV values are lower in Z compared to the XY direction. We also observe that QSI metrics are generally more reproducible than ADC values. The small relative change between scan/rescan values for QSI metrics suggest very good reproducibility in both XY (less than 10%) and Z (less than 5%), while the intra-subject variation of ADC values is considerably higher with 26% in XY and 7% in Z. All investigated ROIs show similar scan/rescan reproducibility over all the studied ADC and QSI parameters.

6.2.2 Differences between tract-specific ROI measurements

Comparing XY and Z parameters: Figure 6.3 shows mean and standard deviation of both ADC and QSI values over all 10 healthy subjects in each ROI. In all ROIs, ADC_{xy} values are significantly lower than ADC_z. Similarly, in XY we also observe small FWHM and larger P0 compared to Z parameters. Both ADC and QSI findings support our assumption of restricted diffusion predominantly in XY direction.

Difference between WM and GM: Table 6.3 presents the results of pairwise t-tests between all GM and WM ROIs, testing for statistically significant differences in individual ADC and QSI metrics. The most significant differences are found between both the lateral tracts and GM region, as well as the posterior tract and GM. In both ADC and QSI, the XY measurements distinguish WM and GM regions better than the Z parameters. All the XY parameters, i.e. ADC_{xy}, $P0_{xy}$ and $FWHM_{xy}$, show similar p-values in detecting the differences between GM and the WM regions. In contrast, neither of the parameters is able to discriminate AT from GM.

Differences between WM regions: No statistical difference is observed between left and right LT in either ADC or QSI values. However, we detect differences between the PT and both LTs with ADC and QSI ($p<0.05$). The $P-values$ between PT and LTs are consistently smaller in $P0_{xy}$ and $FWHM_{xy}$ compared to ADC_{xy}. None of these tracts show significant differences in any of the XY metrics. AT appears different from all the other WM regions with most ADC/QSI parameters in XY and Z.

Multi-variate differences between tract-specific ROI measurements: Table 6.4 shows the results of the multivariate test for statistical differences between ROIs for various combinations of ADC_{xy}, ADC_z, and P0 and FWHM metrics

Table 6.2: *Absolute and relative change (in percent) between scan and rescan of ADC and QSI in 4 healthy volunteers*

(a) Perpendicular (ADC_{xy}) and parallel diffusivity (ADC_z)

$\mathbf{ADC}_{xy} \times 10^{-9} m^2/s$

subject	rLT	lLT	AT	PT	GM
1	0.02 (7.6%)	0.04 (11.5%)	0.01 (1.9%)	0.03 (9.5%)	0.01 (1.0%)
2	0.03 (10.1%)	0.10 (34.9%)	0.07 (15.0%)	0.21 (47.3%)	0.01 (3.0%)
3	0.02 (6.5%)	0.09 (24.4%)	0.09 (18.6%)	0.13 (37.5%)	0.08 (14.8%)
4	0.11 (29.8%)	0.06 (16.4%)	0.17 (32.1%)	0.03 (10.4%)	0.03 (5.3%)
mean	0.05 (13.5%)	0.07 (21.8%)	0.08 (16.9%)	0.10 (26.2%)	0.03 (6.0%)

$\mathbf{ADC}_z \times 10^{-9} m^2/s$

subject	rLT	lLT	AT	PT	GM
1	0.22 (10.9%)	0.07 (3.4%)	0.23 (12.3%)	0.24 (11.9%)	0.31 (19.9%)
2	0.33 (17.4%)	0.12 (5.9%)	0.23 (14.0%)	0.32 (14.3%)	0.34 (17.6%)
3	0.18 (9.3%)	0.01 (0.4%)	0.05 (2.6%)	0.03 (1.3%)	0.04 (2.1%)
4	0.19 (9.5%)	0.05 (2.7%)	0.01 (0.6%)	0.12 (5.6%)	0.13 (7.4%)
mean	0.23 (11.8%)	0.06 (3.1%)	0.13 (7.4%)	0.18 (8.3%)	0.21 (11.8%)

(b) Perpendicular and parallel QSI parameters

$\mathbf{P0}_{xy}$

subject	rLT	lLT	AT	PT	GM
1	0.00 (0.0%)	0.04 (18.4%)	0.02 (8.6%)	0.00 (1.8%)	0.00 (2.5%)
2	0.00 (0.0%)	0.03 (11.1%)	0.01 (4.4%)	0.03 (15.8%)	0.01 (3.2%)
3	0.01 (5.7%)	0.00 (0.0%)	0.01 (4.7%)	0.02 (10.6%)	0.02 (10.9%)
4	0.01 (3.8%)	0.01 (3.4%)	0.00 (2.2%)	0.00 (0.0%)	0.01 (4.0%)
mean	0.01 (0.0%)	0.02 (0.0%)	0.01 (0.0%)	0.01 (0.0%)	0.01 (0.0%)

$\mathbf{FWHM}_{xy}$

subject	rLT	lLT	AT	PT	GM
1	0.00 (0.0%)	3.00 (14.6%)	1.60 (7.1%)	0.40 (1.9%)	0.70 (2.5%)
2	0.20 (0.9%)	1.90 (9.4%)	1.00 (4.0%)	3.20 (13.6%)	1.00 (4.7%)
3	1.20 (5.9%)	0.30 (1.4%)	0.50 (2.1%)	2.00 (9.3%)	1.90 (7.6%)
4	0.40 (1.8%)	0.10 (0.4%)	0.10 (0.4%)	0.40 (1.8%)	0.80 (3.1%)
mean	0.45 (2.2%)	1.33 (6.5%)	0.80 (3.4%)	1.50 (6.7%)	1.10 (4.5%)

$\mathbf{P0}_z$

subject	rLT	lLT	AT	PT	GM
1	0.01 (4.8%)	0.00 (2.9%)	0.01 (4.6%)	0.01 (7.5%)	0.01 (10.1%)
2	0.01 (11.1%)	0.00 (2.0%)	0.01 (7.0%)	0.01 (5.8%)	0.01 (10.9%)
3	0.01 (5.7%)	0.00 (1.2%)	0.00 (1.9%)	0.00 (0.4%)	0.00 (1.0%)
4	0.01 (5.9%)	0.00 (0.0%)	0.00 (0.9%)	0.00 (3.1%)	0.00 (3.6%)
mean	0.01 (6.9%)	0.00 (1.5%)	0.00 (3.6%)	0.00 (4.2%)	0.01 (6.4%)

$\mathbf{FWHM}_z$

subject	rLT	lLT	AT	PT	GM
1	1.80 (3.0%)	1.00 (1.6%)	3.00 (5.3%)	5.40 (8.8%)	4.40 (8.4%)
2	6.10 (10.4%)	0.80 (1.3%)	3.50 (6.4%)	4.30 (6.5%)	8.50 (14.1%)
3	4.20 (7.1%)	1.20 (1.8%)	1.60 (2.7%)	0.40 (0.6%)	1.60 (2.6%)
4	3.50 (5.6%)	1.00 (1.7%)	0.50 (0.9%)	0.00 (0.0%)	1.60 (2.8%)
mean	3.90 (6.5%)	1.00 (1.6%)	2.15 (3.8%)	2.53 (4.0%)	4.03 (7.0%)

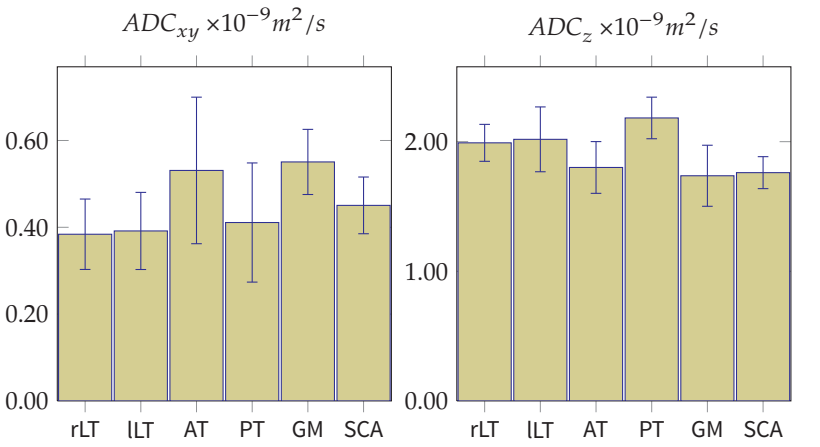

(a) ADC_{xy} & ADC_z

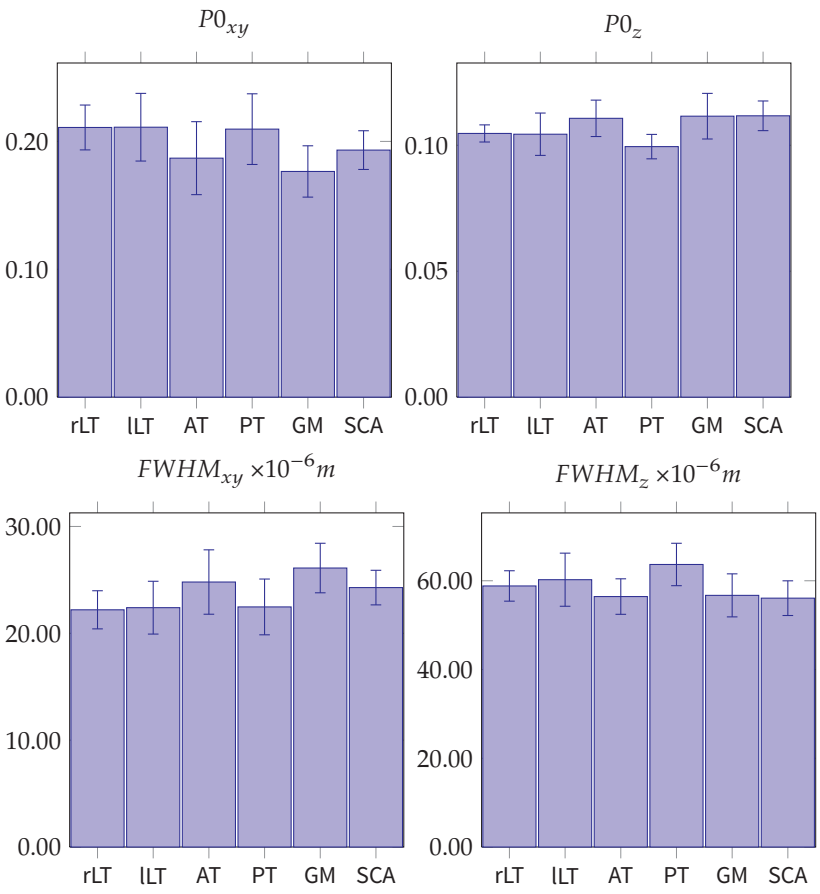

(b) QSI_{xy} & QSI_z metrics

Figure 6.3: *Mean and standard deviation of ADC and QSI parameters over all 10 healthy controls for each SC tracts.*

in XY and Z. As expected from single parameter t-test results, each tested combination is sensitive to differences between WM (except AT) and GM. However, including any of the QSI_z parameters noticeably reduced the significance of the observed differences.

Between WM regions, the combination of ADC_{xy} and ADC_z shows good discrimination between the left and right LTs and the PT. In contrast, neither combinations of QSI metrics in XY is significantly different between any pair of WM regions. However, the combined QSI_z metrics ($P0_z$,$FWHM_z$) revealed differences between PT and rLT and PT and AT that are not found in XY. The full combination of both QSI_{xy} and QSI_z revealed the least differences between any tracts.

6.2.3 Correlation between ADC and QSI

Table 6.5 shows the Pearson coefficient and p-value for voxel-wise correlations between the investigated ADC and QSI metrics. We observe a strong correspondence ($p<0.01$) between ADC measurements and P0 and FWHH QSI metrics in X as well as FWHM in Z. $P0_z$ is the only parameter that does not correlate with any of the other metrics, which suggest that it captures additional information that is neither present in the ADC_z value nor in any of the XY measurements.

6.3 Discussion

6.3.1 Reproducibility

We find overall very good reproducibility of our measurements in both XY and Z. We attribute this to the combination of: (i) the small FOV imaging protocol, (ii) careful positioning, and (iii) strong gradient hardware. ADC values are considerably less reproducible than QSI metrics. To some degree this can be explained by the fact that only a subset of the full QSI dataset was used to compute the ADC values. On the other hand, the ADC model is very simple and the number of data points we used in this study for ADC fitting should suffice to allow a reliable fit of the mono-exponential decay curve. We assume therefore that the improvement we find in intra-subject reproducibility of QSI over ADC are unlikely to be just an effect of the number of acquisitions alone but rather a feature of the QSI method.

6.3.2 Discrimination of tracts in healthy spinal cord

Both ADC and QSI parameters allow some degree of discrimination between the different ROIs we investigated in this study. In both metrics, GM is most differentiated from all WM regions (except AT). The AT region presents values very similar to those found in the GM region. This can partly be explained by the largest standard deviation of all investigated ROIs. However, it must be noted that the AT is the most difficult ROI to locate due to its small size. Its size and location makes it hard to delineate from GM in the studied part of the SC. Furthermore, both the AT and GM suffer most from CSF contribution

Table 6.3: *Pair-wise t-test results between SC tracts in ADC and QSI parameters. Statistically different values are marked* ***bold*** *for p<0.05,* ***bold-italic*** *for p<0.01.*

(a) ADC_{xy} & ADC_z

ADC_{xy}	lLT	AT	PT	GM
rLT	0.51	***<0.01***	0.53	***<0.01***
lLT		***<0.01***	0.60	***<0.01***
AT			**0.03**	0.73
PT				**0.02**

ADC_z	lLT	AT	PT	GM
rLT	0.83	0.06	**0.03**	**0.02**
lLT		**0.01**	0.06	***<0.01***
AT			***<0.01***	0.44
PT				***<0.01***

(b) QSI_{xy} & QSI_z metrics

$P0_{xy}$	lLT	AT	PT	GM
rLT	0.96	***<0.01***	0.82	***<0.01***
lLT		***<0.01***	0.83	***<0.01***
AT			***<0.01***	0.36
PT				**0.01**

$FWHM_{xy}$	lLT	AT	PT	GM
rLT	0.50	***<0.01***	0.58	***<0.01***
lLT		***<0.01***	0.91	***<0.01***
AT			***<0.01***	0.24
PT				***<0.01***

$P0_z$	lLT	AT	PT	GM
rLT	0.93	0.06	**0.02**	0.05
lLT		***<0.01***	0.05	**0.01**
AT			***<0.01***	0.74
PT				***<0.01***

$FWHM_z$	lLT	AT	PT	GM
rLT	0.46	0.12	***<0.01***	0.19
lLT		**0.01**	**0.03**	**0.04**
AT			***<0.01***	0.85
PT				***<0.01***

Table 6.4: *Hotelling's-T^2 significance of pair-wise tract-specific differences for ADC and QSI metrics (confidence interval: 95%). Statistically different values are marked* ***bold*** *for p<0.05,* ***bold-italic*** *for p<0.01.*

(a) ADC_{xy},ADC_z

	lLT	AT	PT	GM
rLT	0.93	**0.04**	**0.03**	***<0.01***
lLT		0.09	0.22	***<0.01***
AT			***<0.01***	0.81
PT				***<0.01***

(b) Perpendicular QSI ($P0_{xy}$,$FWHM_{xy}$)

	lLT	AT	PT	GM
rLT	0.44	0.10	0.60	***<0.01***
lLT		0.19	0.92	**0.01**
AT			0.23	0.43
PT				**0.01**

(c) Parallel QSI parameters ($P0_z$,$FWHM_z$)

	lLT	AT	PT	GM
rLT	0.57	0.08	**0.02**	**0.04**
lLT		0.22	0.32	0.19
AT			***<0.01***	0.63
PT				**0.01**

(d) Both perpendicular and parallel QSI ($P0_{xy}$,$FWHM_{xy}$,$P0_z$,$FWHM_z$)

	lLT	AT	PT	GM
rLT	0.71	0.22	0.17	**0.02**
lLT		0.45	0.69	0.08
AT			**0.03**	0.66
PT				**0.02**

from the anterior median fissure (in case of the AT) and the spinal canal (in case of GM). Therefore the resulting measurements in this region might rather be caused by partial volume effects with CSF and GM (as shown in Chapter 5) than reflect a difference in underlying microstructure of the WM in the AT.

We did not observe any differences between WM regions in the XY direction with either ADC or QSI measurements. This is likely an effect of the relatively low gradient strength we used here, which does not allow us to distinguish the small axon diameters we expect to find in WM tracts. Considering the relatively long gradient pulse duration of $\delta = 11ms$ used in this study, the centre-of-mass effect described would cause similar contrast for small axons (in Section 2.4.5 for details). A further indication of this is the strong correlations between ADC and QSI parameters, which might suggest that the contrast might be governed by the hindered diffusion compartment rather than by differences in restriction.

Interestingly, we found ADC and QSI parameters in Z to be more sensitive to differences between lateral and posterior tracts. Unlike, XY measurements, diffusion along the long axis of the SC is considered to be predominantly hindered. Henceforth, the observed differences are less likely to be attributed to differences in axon diameter distributions. Instead, they might inform about other microstructural properties such as the axon packing density or dispersion[169] or axonal undulation[110], which might differ between the PT and

Table 6.5: *Pearson-correlation coefficient and significance between all ADC and QSI metrics. P-values* < 0.01 *are displayed as* ***bold-italic****.*

		ADC_{xy}	ADC_z	$P0_{xy}$	$FWHM_{xy}$	$P0_z$	$FWHM_z$
ADC_{xy}	r	1.00	0.43	-0.15	-0.25	-0.01	0.15
	p		***<0.01***	***<0.01***	***<0.01***	*0.60*	***<0.01***
ADC_z	r	0.43	1.00	-0.46	-0.30	0.00	0.21
	p	***<0.01***		***<0.01***	***<0.01***	*0.85*	***<0.01***
$P0_{xy}$	r	-0.15	-0.46	1.00	-0.05	0.01	0.16
	p	***<0.01***	***<0.01***		***<0.01***	*0.55*	***<0.01***
$FWHM_{xy}$	r	-0.25	-0.30	-0.05	1.00	0.00	-0.80
	p	***<0.01***	***<0.01***	***<0.01***		*0.92*	***<0.01***
$P0_z$	r	-0.01	0.00	0.01	0.00	1.00	0.00
	p	*0.60*	*0.85*	*0.55*	*0.92*		*0.84*
$FWHM_z$	r	0.15	0.21	0.16	-0.80	0.00	1.00
	p	***<0.01***	***<0.01***	***<0.01***	***<0.01***	*0.84*	

the LTs. In addition, the parallel metrics might also be influenced more by non-axonal features such as glial cell density in the WM tracts than their perpendicular counterparts. No significant correlation was found between QSI in XY and Z, suggesting that QSI in Z provides valuable information on these microstructural properties, which is complementary to the XY measurements.

Finally, we found no advantage in combining multiple QSI parameters in the multi-variate Hotelling-T^2 tests. We suggest this is caused by the redundant information provided by P0 and FWHM parameters describing the dPDF in this clinical set up. This is also supported by the correlations we find between P0 and FWHM in both XY and Z.

6.3.3 Comparison to previous study

The improved study design and image protocol leads to a much reduced variation in both ADC and QSI metrics compared to the previous study (previously variations were found >40% in XY and >16% in Z). Using the better image volume positioning method, we are also more confident in measuring ADC and QSI perpendicular and parallel to the major SC nerve fibres.

Both studies identified significant differences between GM and WM regions. The major difference between the two experiments is the fact that in Experiment 1 we were able to find statistical differences in XY metrics, which we couldn't reproduce in this second study. However, it should be noted that some of those XY findings were suspicious, e.g. they showed differences between left and right lateral tract. Although we find less discrimination in XY here, we think the result from this study are more convincing. The discrepancies are likely artefactual and stem from different hardware and study designs. Nevertheless, the study size is small for both experiments and a larger cohort would be needed to verify the results.

6.4 Conclusion

We have performed two experiments to investigate reproducibility of QSI metrics. We compared QSI metrics with conventional ADC analysis and investigated their ability to discriminate individual WM and GM tracts. For the first time, we also report QSI parameters measured parallel to the SC long axis. In both studies we found better intra- and inter-subject reproducibility in QSI compared to ADC in all investigated ROIs. Furthermore, both QSI and ADC did discriminate GM and WM as well as between some WM ROIs, although QSI metrics did not increase the differences significantly. Furthermore, we found that measurements in Z helped to distinguish structural differences of WM tracts with more accuracy, and complemented ADC and QSI values in the XY direction.

The encouraging initial results described in Chapter 5 motivated this second study, in which we tackled some of the major limiting factors of the previous Experiment, in particular low gradient strength and low spatial resolution. We confirmed the general trends found in intra- and inter-subject reproducibility, although overall reproducibility was reduced in all metrics as an effect of the optimised imaging protocol. However, we were able to confirm in this experiment that ADC and QSI metrics in Z provides useful information about the microstructure parallel to the principal fibre direction. The low standard deviation of QSI in this study makes our QSI protocol attractive for clinical studies, as it would help reducing sample numbers to detect differences, e.g. in patient cohorts as in [50].

Part III

Microstructure imaging

7

An optimised diffusion MRI protocols framework for estimating axonal characteristics in the presence of a single fibre orientation

In the previous chapters we have investigated two very different techniques in Diffusion Tensor Imaging (DTI) and **q**-space imaging (QSI). In comparison to QSI, DTI requires relatively little amounts of data, but its underlying model is based on the assumption that all observed diffusion is Gaussian. Clearly, this is an over-simplification of the complex diffusion mechanisms present in biological tissue. QSI on the other hand makes no assumption about the diffusion process and can theoretically reveal even the most complex diffusion displacement profiles. QSI generally requires large amounts of data and requires very strong diffusion gradients. Henceforth, the implementation of true QSI on clinical systems is very difficult and the derived parameters are often difficult to interpret (as seen e.g. in chapters 5&6).

In the following chapters we will investigate a different model-based diffusion imaging technique, which can be seen as a compromise between the simple model of DTI and the complex QSI approach. Here, our work is heavily based on the ActiveAx approach by Alexander [3], who used a simple compartment tissue model to derive axon diameter and axon density indices in the brain using standard clinical hardware (see Chapter 2, section 2.4.10).

Alexander's work is designed under the premise of full brain imaging and therefore he presents DWI protocols that work independently of the fibre orientation. We call this the orientation invariant (OI) design. The OI approach is characterised by acquiring multiple high-angular-diffusion-imaging (HARDI) shells and requires good angular resolution to retain the orientation invariant features. As a consequence, the OI protocols used, e.g. in [4], require scan times of more than 1 hour, which limits their transition to clinical practice.

The main motivation of this work is to reduce the scan time of the ActiveAx protocols to a more clinically applicable limit of 20-30 minutes. The central objective in attaining this reduction is to discard the requirement for orientation invariance and focus on structures with a coherent known single fibre orientation. Many previous studies have focussed on those single fibre structures (e.g. corpus callosum (CC) or spinal cord (SC)) as they can be expressed in terms of relatively simple models without the need to include complex fibre configurations such as multiple fibre crossings, bending or fanning. Furthermore, many single fibre structures such as CC and SC are of great importance to many developmental and pathological processes. Our approach makes imaging these structures more practicable within a 20-30 minute time frame, where a full-brain protocol with a scan time of 1 hour or more might not be feasible.

In this chapter, we present a modification to the existing protocol optimization framework of [3] (see Section 2.4.10) that incorporates this a-priori information about fibre organisation. We call this the single fibre (SF) design. We evaluate different SF implementations and use computer simulations to test and compare the SF strategy with the original OI approach. By design, the SF protocols are optimised only for a specific predetermined fibre orientation. However, in reality there will always be some variation even in very coherently aligned white matter (WM) tracts. We therefore test how much influence this variation has on SF compared to OI. Finally, we implemented an instance of the SF protocol to demonstrate its feasibility within a real biological tissue sample of fixed cervical monkey SC. Although this study is motivated by improving *in-vivo* clinical applicability, we chose to first test our approach on a pre-clinical scanner on a fixed tissue sample to avoid the challenges of *in-vivo* scanning (e.g. motion and insufficient image resolution) and focus on an initial demonstration of our method. The results and observations made in this chapter form the basis of the subsequent *in-vivo* implementation we present in the following chapter.

7.1 Protocol optimisation

This section discusses how we adapt the OI optimisation of Alexander [3] to the SF case. The original OI optimisation is designed to determine the best OI DWI protocols, i.e. the best PGSE pulse parameters, i.e. diffusion gradient strength ($|G|$), diffusion gradient pulse duration (δ), diffusion time (Δ), for a fixed number M of shells, each including a fixed number N of distributed gradient directions. The gradient directions scheme in the OI protocols is fixed and uniformly distributed over the sphere as in [36]. The HARDI-like gradient scheme is necessary to guarantee orientational invariance, i.e. be sensitive to restriction regardless of diffusion direction. In our SF implementation we can assume a known diffusion direction and therefore do not require the uniform angular sampling of the OI approach. This allows us to include the gradient scheme together with the PGSE pulse setting in the optimisation process. In addition to SF, which optimises gradient scheme and PGSE pulse parameters simultaneously, we are also interested in how much effect the optimisation of the gradient scheme alone (SFDIRS) and the PGSE parameters alone (SFPULSES) has on the performance of the resulting protocols. In total we tested the four following different variants of Alexander's [3] optimisation framework, given a number of shells M and a number of gradient directions per shell N:

OI: The orientation invariant protocol optimisation as described in [3]. The algorithm uses a fixed gradient scheme of isotropically distributed gradient directions for each of the M shells and only optimises the PGSE pulse parameters. To minimise the influence of the fibre direction, the method is performed for a set of 'worst case' fibre directions, which are determined prior to the optimisation.

Table 7.1: *Overview of parameters for the tested protocol optimisation approaches.*

Protocol name	OI (orientation invariant)	SF (pulses + directions)	SFPULSES (pulses only)	SFDIRS (directions only)
Free parameters	δ_m, Δ_m, G_m	$\phi_{m,n}, \theta_{m,n}$ δ_m, Δ_m, G_m	δ_m, Δ_m, G_m	$\phi_{m,n}, \theta_{m,n}$
Fixed parameters	ϕ_n, θ_n	–	ϕ_n, θ_n	δ_m, Δ_m, G_m
Specific fibre direction	no	yes	yes	yes
No. of free parameters	O(M)	O($M \times N$)	O(M)	O($M \times N$)

SF: The adapted algorithm optimises both the PGSE parameters and gradient direction scheme for M shells assuming a single a-priori known fibre direction. In other words, this individually optimises the $M * N$ gradient directions within the protocol together with the M PGSE pulse parameters.

SFPULSES: Similar to the OI optimisation approach, the algorithm uses a fixed gradient scheme for each of the M shells. The main difference to the OI design is that the algorithm optimises for a single a-priori known fibre direction instead of a set of 'worst case' fibre directions.

SFDIRS: This is a two-step optimisation approach. The SFPULSES algorithm is performed to determine the best M PGSE pulse settings. In a second step the gradient scheme for each of the M shells is optimised, keeping the PGSE pulse parameters fixed.

Table 7.1 summarises the optimisation parameters for each of the four algorithms. It is important to note that the inclusion of the optimisation of individual gradient directions in SFDIRS and SF drastically increases the number of free parameters to be optimised from $O(M)$ to $O(N \cdot M)$ compared to OI and SFPULSES.

7.1.1 Tissue model

Like Alexander [3], we use a simple two-compartment model of white matter tissue, with axons represented as cylinders with a single radius and extra-axonal tissue represented by an axially symmetric diffusion tensor ('Zeppelin-Cylinder' in the taxonomy of Panagiotaki et al. [118]). We assume tissue diffusion properties typically found in healthy *in-vivo* human white matter based on the recommendations by Alexander et al. [4]. A full list of the model parameters used in the optimisation is given in Table 7.2.

7.1.2 Implementation

We implement the four algorithms as described in Section 7.1 for $M = 8$ different sets of PGSE parameters. For OI and SFPULSES we use the default setting

Table 7.2: *Model parameters used for optimisation.*

Cylinder (intra-axonal)		Axially symmetric tensor (extra-axonal)	
f_{intra}	0.7	f_{extra}	0.3
$d_{\|0}$	$1.7 \cdot 10^{-9}\ m^2/s$	$d_{\|\|}$	$1.7 \cdot 10^{-9}\ m^2/s$
$d_{\perp}$	$6 \cdot 10^{-10}\ m^2/s$	$d_{\perp}$	$6 \cdot 10^{-10}\ m^2/s$
dir	$[0, 0, 1]^T$	dir	$[0, 0, 1]^T$
R	$\{1..1..10\}\mu m$		

for the SOMA algorithm , i.e. 500 migration steps with 100 migrating individuals. For SFDIRS and SFPULSES, the parameter space to explore is much larger and we are using 1000 individuals with 750 migration steps to ensure convergence. To avoid local minima, each optimisation is repeated 5 times and from the resulting protocols the one with the smallest CRLB is chosen. The available gradient strength is limited to 60mT/m to simulate a typical clinical MRI scanner.

7.1.3 Optimised protocols

Figure 7.1 shows the CRLB of the four different optimisation schemes for different N. We can see that CRLB distinguishes the four protocols in two groups: OI/SFPULSES with fixed directions and SFDIRS/SF with optimised directions. SFDIRS and SF consistently produce lower CRLB than OI and SFPULSES regardless of the chosen N, although the differences between the two groups become smaller for larger $N > 60$. For better comparison, Figure 7.1 shows the corresponding N for a different values of CRLB. We can see that SF and SFDIRS both achieve the same CRLB values of OI with significantly less directions. In other words, the SFDIRS and SF promise a comparable performance to OI with only 25%–33% of the amount of data required.

Furthermore, we observe that our SF protocols contain slightly stronger diffusion weighting factors compared to the other protocols. We can attribute this to the custom gradient scheme, which translates to more perpendicular measurements and hence increases the effective SNR in this direction. The optimisation uses this increase in measurement quality to trade off against stronger diffusion weighting factors, which is inherently associated with more noisy data in our framework.

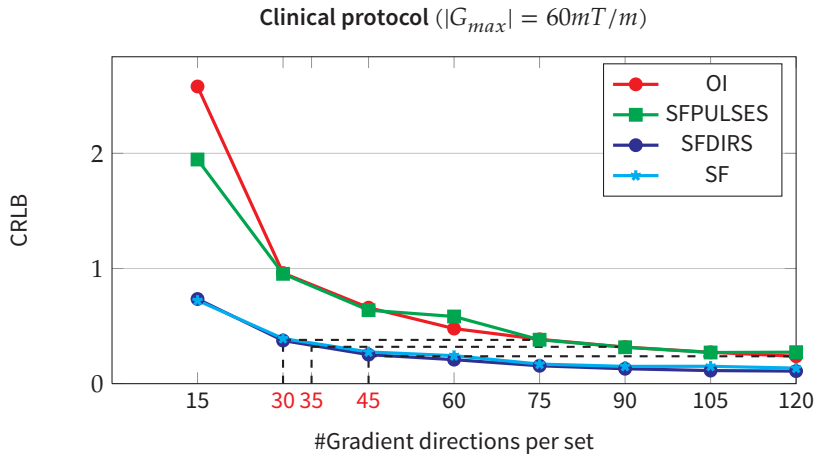

Figure 7.1: *CRLBs of optimised protocols with different N number of gradient directions.*

Figure 7.2 shows the CRLB of the four different optimisations for a fixed $N = 90$ but different signal-to-noise ratio (SNR) conditions. The results here are very similar to the findings shown above. Both SF and SFDIRS consistently show CRLB values three to four times lower than those of OI and SFPULSES for similar SNR values. The differences are most apparent for low SNR values, which are also more common in real clinical diffusion MRI.

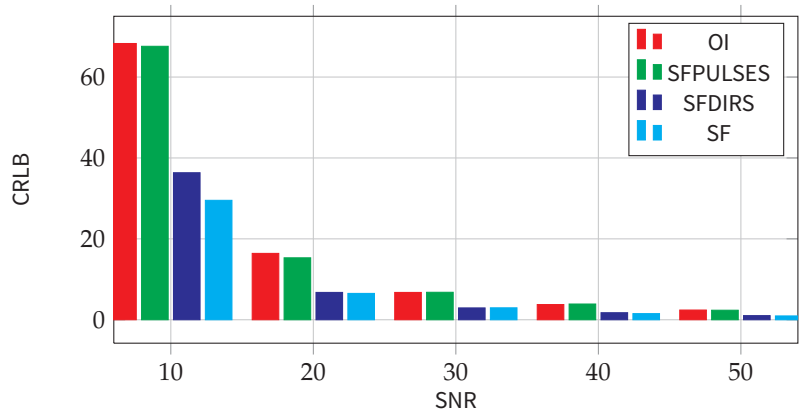

Figure 7.2: *CRLBs of optimised protocols under different SNR.*

Table 7.3 shows an example of the OI and the three SF protocol variants we obtain for $N = 90$ and SNR$= 20$. A more comprehensive visualisation of the different protocol parameters can be found in Appendix 7.A.1. We deliberately chose a large number of M to reevaluate the optimal number of different PGSE for each protocol. Our findings here show that a smaller number of $M = 4$ suffices to capture all unique combinations of PGSE pulse parameters, which confirms the results of Alexander [3]. We also note that OI and SFPULSES protocols are almost identical, suggesting that the choice of diffusion orientation for the OI has little influence on the outcome of the algorithm.

Table 7.3: *Protocol parameters and gradient schemes for $N = 90, M = 8$. The M different gradient direction schemes are coded by different colors. Please note that in the OI and SFPULSES protocols all M gradient direction schemes are identical.*

(a) OI protocol

δ $[ms]$	Δ $[ms]$	$\|G\|$ $[mT/m]$	b-value $[s/mm^2]$
12.9	17.9	60	583
12.9	17.9	60	585
12.9	17.9	60	587
12.9	17.9	60	588
22.7	48.3	30	1480
24.4	46.6	30	1684
26.3	44.7	40	2752
33	38	60	7585

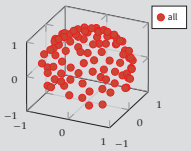

(b) SFprotocol

δ $[ms]$	Δ $[ms]$	$\|G\|$ $[mT/m]$	b-value $[s/mm^2]$
14.7	19.8	60	832
14.8	19.8	60	837
15.1	20.1	60	883
15.4	20.4	60	932
21.2	53.9	30	1361
27.2	47.9	40	3123
27.9	47.2	40	3452
35	40	60	8974

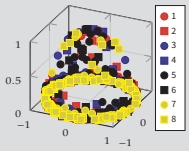

(c) SFPULSESprotocol

δ $[ms]$	Δ $[ms]$	$\|G\|$ $[mT/m]$	b-value $[s/mm^2]$
12.8	17.8	60	572
12.9	17.9	60	580
12.9	17.9	60	580
12.9	17.9	60	582
21.9	48.9	30	1484
24.7	46	30	1677
26.3	44.5	40	2639
32.9	37.9	60	7515

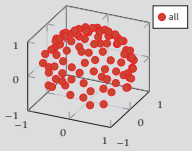

(d) SFDIRS protocol

δ $[ms]$	Δ $[ms]$	$\|G\|$ $[mT/m]$	b-value $[s/mm^2]$
12.8	17.8	60	572
12.9	17.9	60	580
12.9	17.9	60	580
12.9	17.9	60	582
21.9	48.9	30	1484
24.7	46	30	1677
26.3	44.5	40	2639
32.9	37.9	60	7515

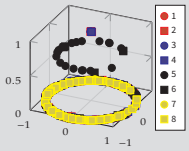

7.2 Experiments

7.2.1 Synthetic data

From all protocols for N=90 and SNR=20 we generate synthetic datasets, with which we then test and compare the performance of the different protocol optimisations. The number of gradient directions was chosen to be large in order to allow sufficient angular resolution for OI and SFDIRS protocols.

The MR signals are generated from the same tissue model and tissue diffusion properties we used for the protocol optimisation (see section 7.1 and Table 7.2 for details). We use the Camino software package [37] to simulate datasets for four different cylinder radii $R = 1, 2, 5, 10\mu m$ as a representation of radii usually found in *in-vivo* white matter tissue. To simulate noise in the MR acquisition, we add Rician noise with SNR=20 to the simulated noise-free datasets. To concentrate on comparing the estimates of radius and volume fraction between the protocols we assume all cylinders to be perfectly aligned along the $[0, 0, 1]^T$ as assumed in the optimisation process.

Effect of principal diffusion direction

Even in very coherent structures such as the CC, the observed fibre direction is subject to some variation. However the protocols SF and SFDIRS contain gradient schemes designed for a fixed principal diffusion direction. To test the effect of potential misalignment between assumed and true principal diffusion direction we designed the following experiment.

We created similar dataset as above, with the exception of varying the principal diffusion direction for each synthetic sample. Using the spherical representation of the cylinder direction, we sampled each combination of polar angle $\phi \in \{0..90\}^\circ$ and azimuth angle $\theta \in \{0..180\}^\circ$ in discrete steps of 5°. In total we simulated 703 unique datasets with different principal diffusion directions (see Figure 7.3 for a plot of the generated diffusion directions).

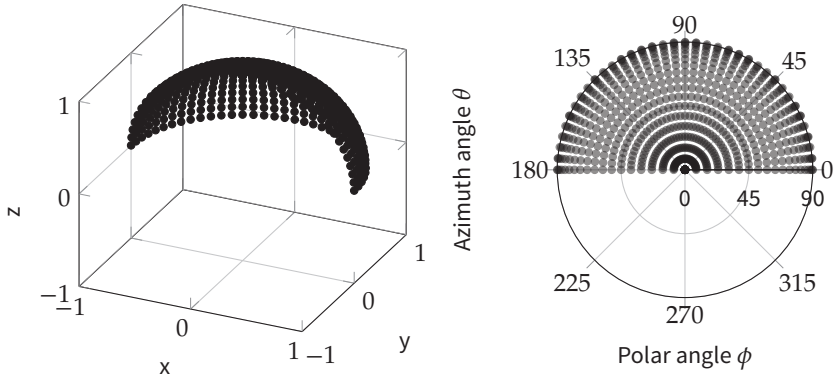

Figure 7.3: *Generated diffusion directions to test orientation bias as 3-d scatter plot (left panel) and polar scatter plot (right panel).*

Dispersion

The dispersion of fibres is another confounding factor that has considerable influence on the estimates of cylinder radius and volume fraction as shown by Zhang et al. [167]. While Zhang et al. also showed that the effect in coherent structures with moderate dispersion, such as in the CC, is negligible for OI, it is unclear whether this is still the case for the optimised gradient schemes used in our SF and SFDIRS protocols. We therefore created a set of data to test the effect of dispersion on our protocols. To simulate different degrees of dispersed diffusion directions, we used the the Von-Mises-Fisher distribution p_d:

$$p_d(\mathbf{x}; \mu, \kappa) = \frac{\kappa}{2\pi(e^{\kappa} - e^{-\kappa})} \left(\kappa \mu^T \mathbf{x}\right), \tag{7.1}$$

which is defined for each point $\mathbf{x} \in {}^2$ on the unit sphere with μ being the mean distribution of the distribution, and κ being the scalar concentration parameter that controls the dispersion of the distribution. From p_d we sampled 1000 directions. We then took the average of the noise-free MR signal generated from our tissue model, and added Rician noise as described above. To simulate different degrees of dispersion we varied $\kappa \in [2, 4, 8, \ldots, 512]$ with fixed $\mu = [0, 0, 1]^T$. Figure 7.4 illustrates the sampled directions for each of the used κ values. For $\kappa \to \infty$ the amount of dispersion becomes neglible and the simulation is equivalent to a perfectly coherent fibre configuration.

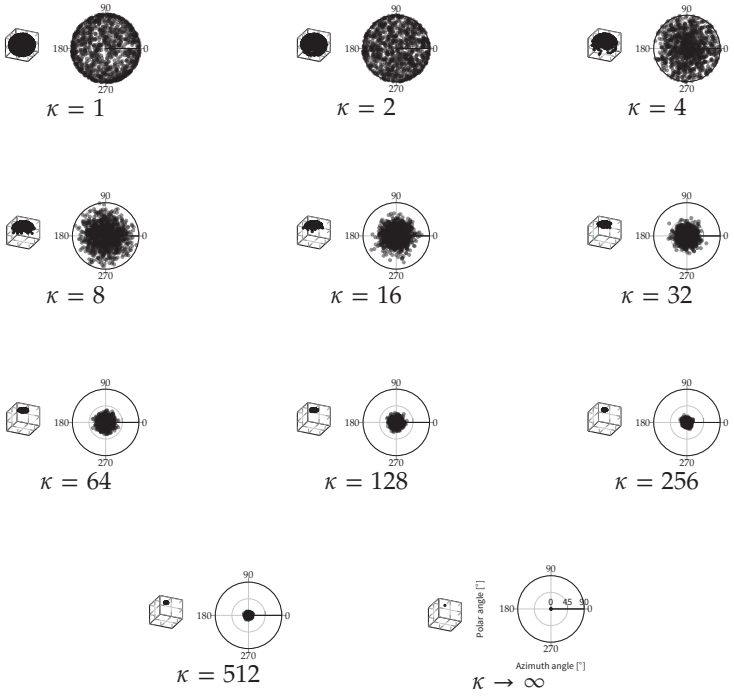

Figure 7.4: *Visualisation of 1000 sample directions drawn from Von-Mises-Fisher distribution with varying κ. Left half of each figure shows the 3-d scatter plot, right half shows a polar plot of the sampled directions for each value of κ.*

7.2.2 Feasibility study on fixed monkey spinal cord

Scans were performed on an experimental 4.7 Tesla scanner (Varian Inc., Palo Alto, CA, USA) in collaboration with the Danish Research Centre for Magnetic Resonance (DRCMR). To make best use of the hardware, we carried out the protocol optimisation as described above but increased $|G|_{max}$ to $300mT/m$. We also adjusted for differences in tissue properties between live and fixed tissue, e.g. decreased diffusivity and shrinkage of axon diameters, based on preliminary DTI analysis of the tissue sample. The full list of modified tissue parameters is given in Table 7.5. Scan time in this experiment was limited to 12h only. To retain acceptable image resolution and SNR within the given time frame, we reduced the number of acquisitions to $M = 4$ and $N = 30$. Furthermore, we only had time to test the SF protocol in this experiment. The resulting protocol is summarised in Table 7.4 and described more comprehensively in Appendix 7.A.2.

We used a volume coil for transmission and a homemade 20 mm surface coil was used as receive coil. The data was acquired using a spin-echo sequence with single line readout and a conventional pulsed gradient spin-echo preparation [142]. TE/TR were 59/2000 ms, field-of-view (FOV) was $10 \times 10mm^2$. The matrix size was 64×64 and was 2-D interpolated to 128×128 leading to an axial in-plane resolution of $79 \times 79\ \mu m^2$. To support the high in-plane resolution we acquired thick slices of 1.5mm to achieve acceptable SNR in our data. The protocol was repeated 4 times with a total imaging time of 13 h. The magnitude images of the four repeated measurements were averaged offline prior to analysis.

7.2.3 Model fitting

A voxel-wise fit of the MR signal is performed using a fitting method similar to Alexander et al. [4]. We define the objective function as the likelihood of model parameters given the observed MR signals under Rician noise ($\sigma = 0.05$). We use the multi-run fitting routine of Panagiotaki et al. [118] to find an initial estimate, which determines the best parameter vector from multiple gradient-descend runs with pertubed starting points (n=20 in our case). Based on the

Table 7.4: *Protocol parameters and gradient schemes for the* ex-vivo *protocol ($N = 30$, $M = 4$). The M different gradient direction schemes are coded by different colors.*

δ $[ms]$	Δ $[ms]$	$\|G\|$ $[mT/m]$	b-value $[s/mm^2]$
6	13	300	2541
7	13	300	3353
3	47	300	2656
10	41	254	17736

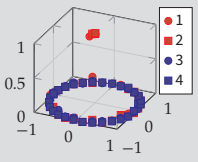

Table 7.5: *Adjusted* ex-vivo *tissue model parameters used for pre-clinical scan optimisation (changes to* in-vivo *protocol are displayed in red).*

Cylinder (intra-axonal)		Axially symmetric tensor (extra-axonal)	
f_{intra}	0.7	f_{extra}	0.3
$d_{\|0}$	$4 \cdot 10^{-10}\ m^2/s$	$d_{\|\|}$	$4 \cdot 10^{-10}\ m^2/s$
$d_{\perp}$	$2.5 \cdot 10^{-10}\ m^2/s$	$d_{\perp}$	$2.5 \cdot 10^{-10}\ m^2/s$
dir	$[0,0,1]^T$	dir	$[0,0,1]^T$
R	$\{0.5,1,2\}\mu m$		

initial parameter estimates, we then performed a Markov chain Monte Carlo (MCMC) algorithm to determine the posterior distributions of the model parameters. To ensure convergence, we used the following, rather conservative setting for the MCMC algorithm: burn-in of 5000, sample interval of 1000, 5% parameter pertubations with uniform, uninformative priors.

To increase stability of the fitting we fixed $d_{\|}$ to its true value of $1.7 mm/s^2$ similar to previous studies [4, 9, 16]. Moreover, $d_{\perp}$ is approximated by the tortuosity formulation for randomly positioned cylinders proposed by Szafer et al. [144]:

$$D_{\perp} = f_{intra} \cdot D_{\|}. \tag{7.2}$$

For SFDIRS and SF, we also found our method to be very unstable with respect to determining the correct principal diffusion direction of the model, even when the fibre direction was close to $[0,0,1]^T$. This possibly stems from the fact that the initial guess of the direction is computed from the Diffusion Tensor (DT) model. While this method works well for OI and SFPULSES protocols, it fails when using the optimised gradient direction sets of SFDIRS and SF. We therefore fixed the principal fibre direction to $[0,0,1]^T$ in all experiments, unless stated otherwise.

Fixed tissue

We chose to scan a sample of fixed monkey cervical spinal cord to test our protocol in a real biological system. The details of the sample preparation are described in [95]. For the fixed tissue we used a slightly modified fitting routine to account for the differences between fixed and live tissue. For the *ex-vivo* sample we fixed $d_{|0}$ to $0.45 \mu m/mm^2$. The volume fraction of the restricted compartment f was constrained to be in the range of $[0.5, 1.0]$. In each voxel, the mean of the posterior distribution of R and f_{intra} is calculated. For consistency with indices derived from histological examination [1, 77, 86] and also previous imaging studies [4], maps of the axon diameter index $a = 2 \cdot R$ and the axonal density index $\rho = f_{intra}/\pi/R^2$ were generated.

7.3 Results

7.3.1 Accuracy and precision of parameter estimates

Figure 7.5 shows box plots of the fitted volume fraction f_{intra} and R for different cylinder radii.

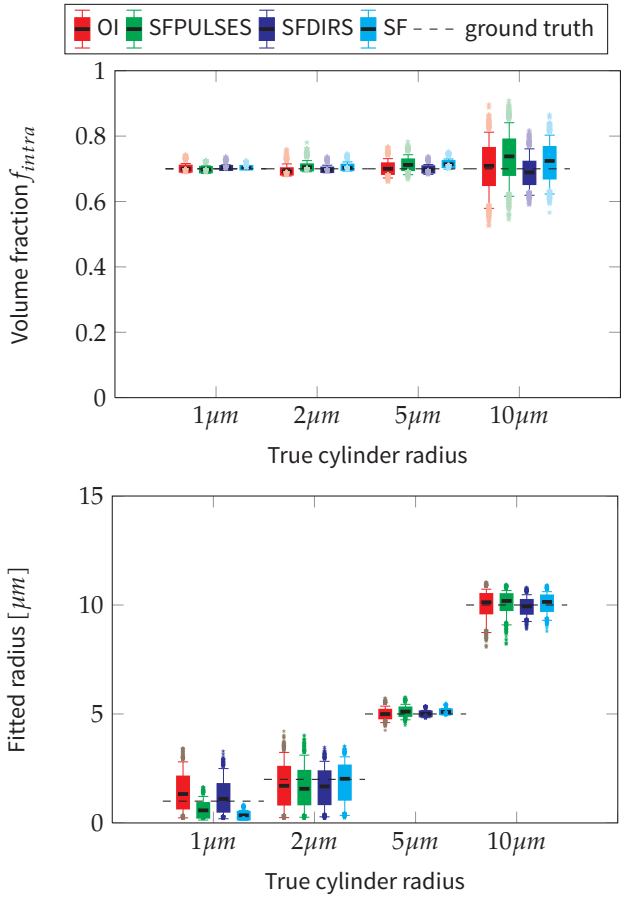

Figure 7.5: *Boxplots of estimated f_{intra} and R for different cylinder radii.*

All protocols can successfully recover the correct value of f_{intra} for all radii 1, 2 and 5 μm with the posterior distributions being centred around the true value $f_{intra} = 0.7$ with little variance. When $R = 10\mu m$ we observe significantly more variance in the estimates for in all protocols. Further we find the estimates to be less accurate, mainly in SF and SFPULSES, which overestimate f_{intra} slightly.

Compared to f_{intra} results, we observe more variance in the posterior distributions of R estimates for all protocols. Over all R, the protocols SFDIRS and SF appear to achieve better results than OI and SFPULSES. To illustrate this better, Figure 7.6 shows the posterior distributions of R for each protocol in more detail.

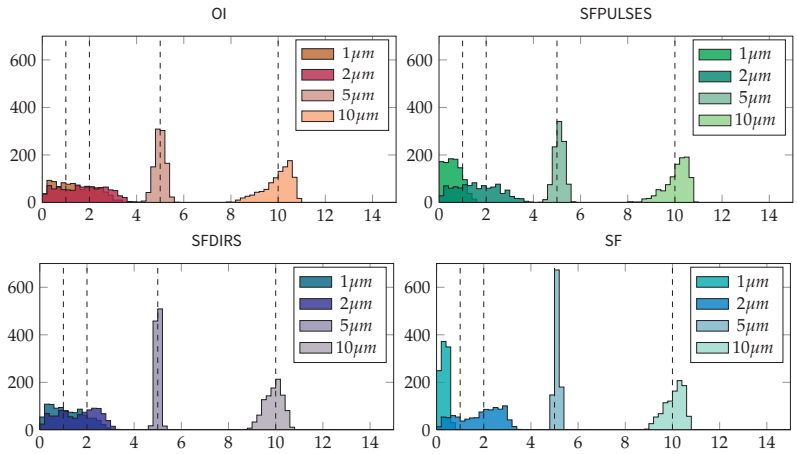

Figure 7.6: *Histograms of fitted cylinder radius R for different protocols.*

All protocols perform best for $R = 5\mu m$ with tight posterior distributions centred around the ground truth. While generally all protocols show very good accuracy in estimating R, SFDIRS and SF have the advantage in terms of precision as their distributions are considerably tighter than for OI and SFPULSES. Compared to $R = 5\mu m$, $R = 10\mu m$ estimates are generally broader and with a noticeable negative skew, particularly for OI and SFPULSES protocols. As for $5\mu m$, SFDIRS and SF produce more sharp parameter distributions than OI and SFPULSES, although the difference is less obvious. The broader distributions for $R = 10\mu m$ might be explained by the lack of diffusion times long enough for most molecules to interact with the boundary, which are necessary to estimate large radii accurately. We assume a typical T2 signal decay of 70ms in this experiment. In this regime long diffusion times can not be reached with acceptable SNR [168]. As a consequence, for $R = 10\mu m$ a greater proportion of the signal will appear unrestricted and causes the underestimation of f_{intra} and larger variation in radius estimates in our results.

Smaller radii, $R = 1\mu m$ and $R = 2\mu m$ can clearly be distinguished from the larger radius samples, but are less well separable from each other in all protocols, with posterior distributions showing significant overlap as expected from limited gradient strength used in this experiment [3, 4, 135]. For small radii the centre-of-mass (COM) effect on small radii prohibits any contrast between small R (see Section 2.4.5 for a detailed explanation). As can be appreciated in Figures 7.6 and 7.5, this results in either a very broad posterior distribution, as seen in OI and SFPULSES protocols or in consistent underestimation of the axon diameter parameter with small variance as seen in SFDIRS and SF. Consequently, none of the four protocols can estimate small R with confidence. However, SF, and to a lesser extent SFPULSES, at least allow some distinction between $R = 1\mu m$ and $R = 2\mu m$, while they are effectively indistinguishable for the two protocols.

7.3.2 Variation of fibre direction

Figure 7.7 shows the root mean squared error for both f_{intra} and R parameters with respect to the principal orientation of diffusion for cylinders with small

radius $R = 2\mu m$ and large radius $R = 5\mu m$. As in the previous experiment, all the protocols generally perform better for $R = 5\mu m$ than $R = 2\mu m$. The most marked differences between protocols appear in the $R = 2\mu m$ dataset.

The plots clearly show that estimates of f_{intra} are unaffected by the true diffusion orientation in all protocols for $R = 2\mu m$. While this is expected for OI and SFPULSES, we can explain the performance of SF and SFDIRS by the small cylinder radius, which even at non-perpendicular angles offers enough restriction for SF and OI to distinguish hindered and restricted diffusion even when the gradient scheme is not aligned perpendicular to the intra-axonal compartment. Respectively, simulation results for $R = 5\mu m$ show that f_{intra} estimates are affected more by the misalignment of the gradient scheme, which artificially increases the effective cylinder radius and is misinterpreted as less restriction in the larger radii samples because less molecules are sufficiently explore the boundary (see also e.g. [12, 167]). However, the estimation error still remains low over all different directions.

Larger differences between the protocols can be seen in the R estimation error. Again, OI and SFPULSES are consistent over the whole range of simulated fibre directions, with no apparent directional pattern of the estimation error. In contrast, SF and SFDIRS performance is considerably more impeded for larger misalignment of gradient scheme and cylinder orientation. The maximum estimation error is observed for rotation angles around 45°. With ϕ close to 90°, the SF and SFDIRS gradient direction scheme now features more measurements perpendicular and parallel to the cylinder compartment, which reduces again the fitting error. For smaller misalignments of $\phi < 15°$ both SF/SFDIRS perform very similar to the OI/SFPULSES protocols.

Effect of fibre dispersion: Figure 7.8 shows the fitted f_{intra} and R estimates different degrees of intra-voxel dispersion of fibre orientations. For small κ, i.e. high degrees of dispersion, we observe large errors in estimates of both f_{intra} and R, as expected e.g. from [167]. However, for $\kappa \geq 64$, the fitted parameters converge to their respective ground truth, although such a value of κ still presents a considerable degree of dispersion (5% quantile of fibre misalignment is 2.5°, 50% quantile is 10°, 95% quantile is 17° respectively). With increasing κ, there appears to be no noticeable difference between the four protocols.

7.3.3 Proof-of-concept *ex-vivo* implementation

Figure 7.9 presents maps of axon diameter a and axonal density ρ in the upper cervical spinal cord obtained from the SF protocol. We can discriminate clearly differences in axon diameter and axonal density indices between anatomically different white matter tracts. Dorsal and lateral sensory tracts show small axon diameters between 1–4μm and a density of 0.03–0.08μm^{-2}. The smallest axon calibers (<1.5μm) are observed in the dorsal columns (DC) while mean axon size in the anterolateral column (ALC) is 1.5–2.5μm. The largest axons (3–4μm) are found in the corticospinal tracts (CST) together with low density of 0.01–0.02μm^{-2}. Overall, we clearly observe left-right symmetry of axon

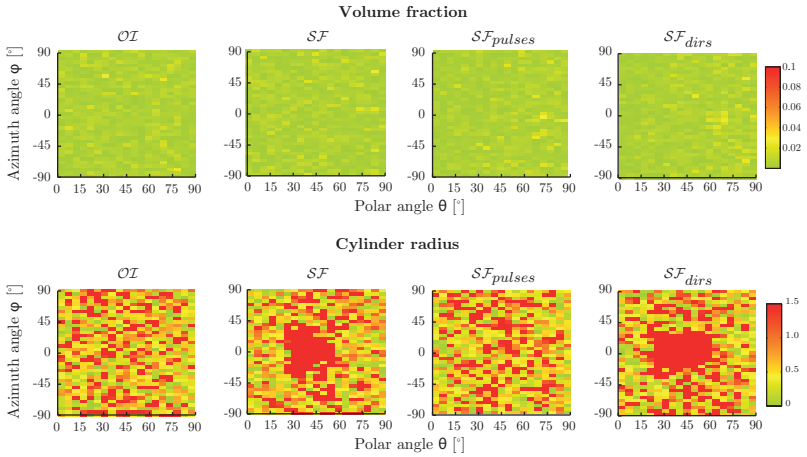

(a) Cylinder radius $R = 2\mu m$

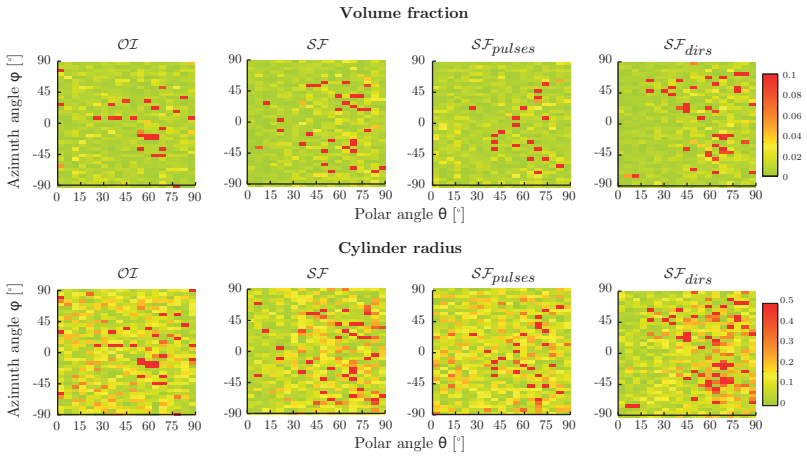

(b) Cylinder radius $R = 5\mu m$

Figure 7.7: *Root mean square error of f_{intra} and R estimates for different principal diffusion directions.*

diameter and density in all tracts, which corresponds well with the known anatomical organisation of the the SC. Parameters are also consistent along the SC within the limits of anatomical variation and are in the range of values reported in previous histological evaluation of the cord [59, 61].

7.4 Discussion

We presented here a novel method that provides optimal diffusion weightings and gradient directions for estimating axonal diameter by exploiting the single fibre orientation of structures like the corpus callosum or spinal cord. We demonstrated that the SF approach reduces the required amount of data by 60–75%, while achieving similar performance to OI. This translates into a considerable reduction in scan time from >1 hour for OI to less than 20-25 minutes, which makes routine clinical implementation much more viable.

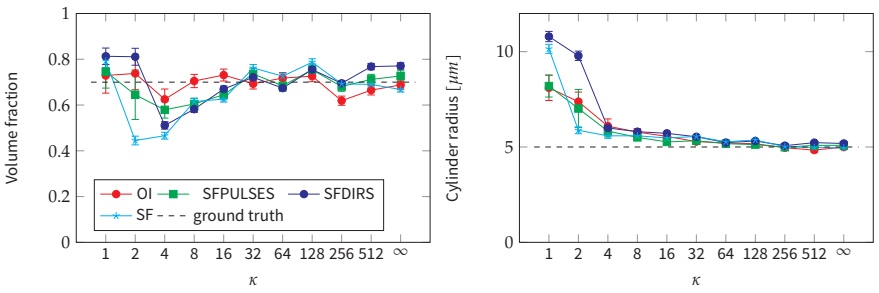

Figure 7.8: *Mean and standard deviation of posterior distribution for fitted volume fraction and radius for different κ values.*

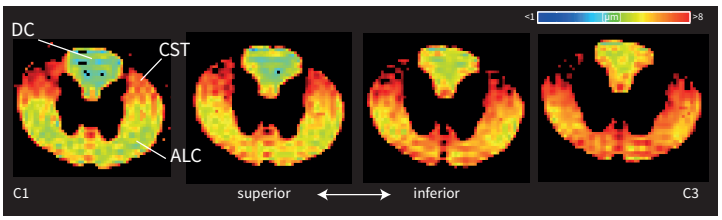

(a) Axon diameter index a

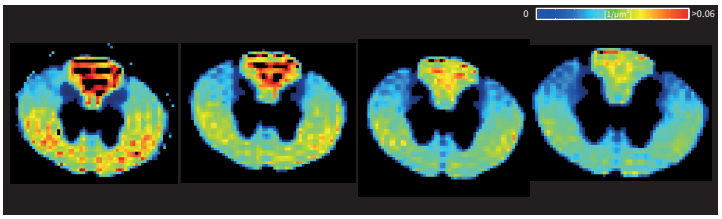

(b) Axon density index ρ

Figure 7.9: *Axial slices of cervical cord (C1–C3) showing maps of a and ρ. White markers show the approximate location of the corticospinal tracts (CST), anterolateral column (ALC) and dorsal column (DC)*

Our results suggest that a dedicated optimisation of gradient directions is clearly beneficial over the orientation invariant OI approach, both in terms of CRLB and simulated noisy data, when the fibre direction is known a-priori. We find that the optimisation routine deliberately diminishes angular resolution in favour of measuring diffusion only in the most informative directions (predominantly parallel and perpendicular to the WM tracts). We noticed that our optimised gradient scheme picks out predominantly gradient directions parallel and perpendicular to the cylinder compartment, presumably to maximise sensitivity to restricted diffusion. In that respect our automatically optimised gradient schemes agree with many other studies e.g. [9, 13, 118, 139], which only chose parallel and perdendicular measurements to maximise sensitivity to restricted diffusion.The few intermediate gradient directions are most likely the result of imperfections in the optimisation due to the overwhelming number of free parameters in the SF and SFDIRS designs (see next chapter for more details). Overall, our results confirm that parallel and perpendicuar directions gives the most information about the tissue, and one should focus on those directions when the fibre configuration is known a-priori. Furthermore, the

simulation results show that the combination of stronger diffusion weighting and custom gradient scheme in the SF design is most successful in estimating the cylinder radius, especially when R is very small.

Considering the small number of distinct gradient directions, it comes as no surprise that we found the optimised gradient schemes in SF and SFDIRS more prone to error when the true fibre orientation differs from the one assumed in the optimisation process. However, when the misalignment was less than 15° (as expected in coherent WM structures) the impact was negligible. We are confident that with careful positioning, the SF gradient scheme can be aligned to the dominant fibre directions in CC and SC with little error, without diminishing the performance of the SF protocols.

Finally, the feasibility study on our post-mortem SC sample demonstrates that we can estimate a reasonable range of axon diameters and densities under realistic imaging conditions, while retaining a high image resolution. Furthermore we were able to distinguish different WM tracts of the SC by both axon diameter and axon density.

There are some limiting factors to our study. Firstly, we only optimise and fit a very simple tissue model, which only allows a crude approximation of the real tissue properties. Other, more complex, models might be a better representation of the real tissue microstructure, e.g. modelling explicitly a distribution of axon radii [16], or including more extra-axonal tissue compartments [118, 139, 154]. While these models might arguably be more accurate, they also require many more acquisitions and therefore do not agree with the aim of this study to reduce the scan time to less than 30 minutes. The choice of a simpler model offers a compromise of manageable data requirements and informative model parameters.

Secondly, the spinal cord sample we used in this study was not available for histological processing. Despite the lack of independent validation, the differences between WM tracts agree with previous results in [59]. It should be noted that our results were obtained with a significantly smaller number of diffusion weighted directions and b-factors compared to other studies [9, 16, 118], making it more comparable to conditions found in *in-vivo* scanning. Nevertheless, in many cases the pre-clinical set-up has advantages over the *in-vivo* situation, as it profits from long scan times, high SNR and an absence of motion artefacts. Although the findings in this experiment might therefore not be directly transferable to clinical practice, the results are sufficiently encouraging to pursue the SF approach in clinical practice. In the next two chapters we will therefore focus on moving the SF approach towards a feasible *in-vivo* implementation on standard clinical hardware.

7.A Protocols

7.A.1 Protocols optimised for $|G|_{max}$=60mT/m, N=90, M=8

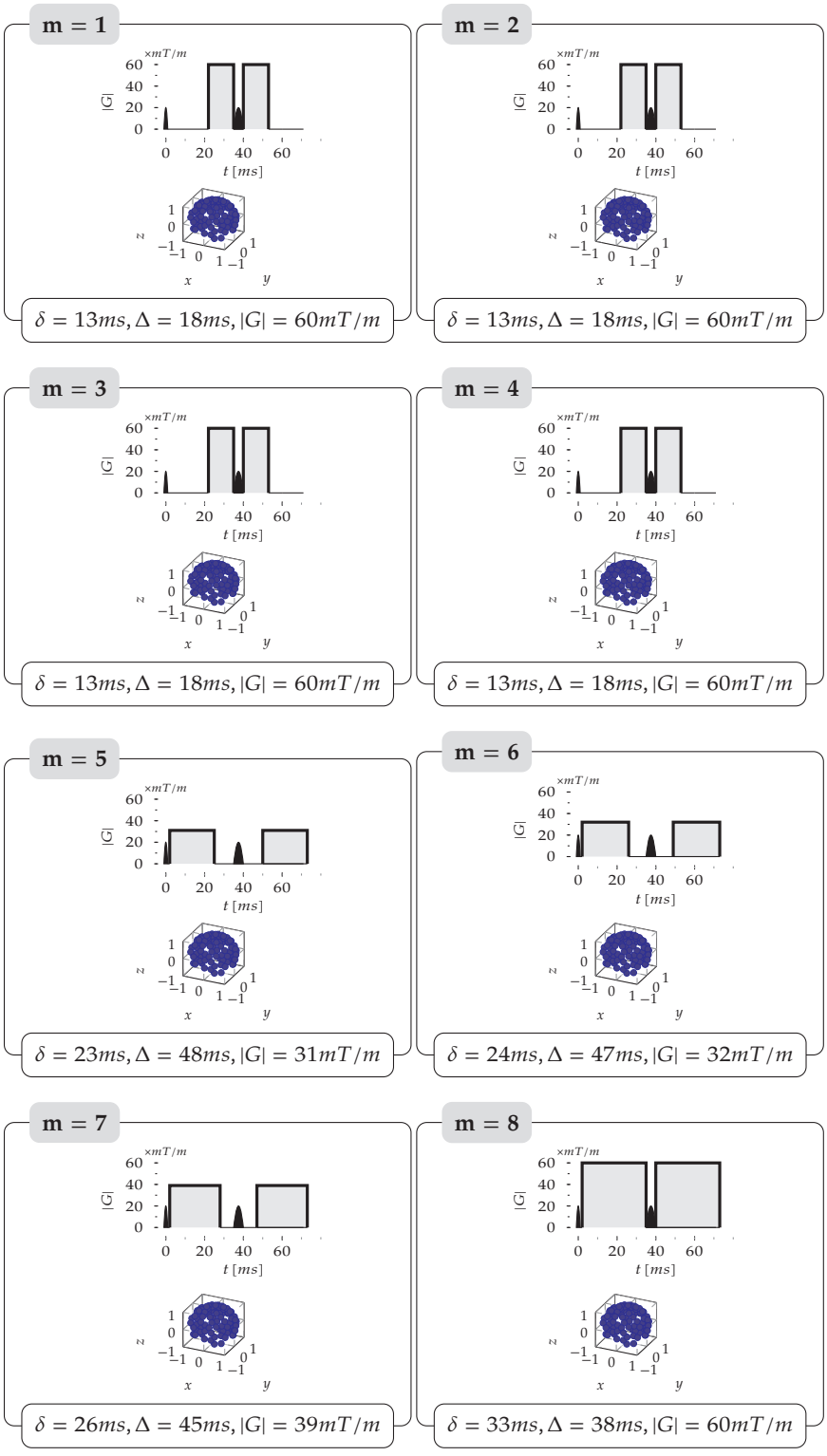

Figure 7.10: *OI protocol optimised for clinical gradient strength.*

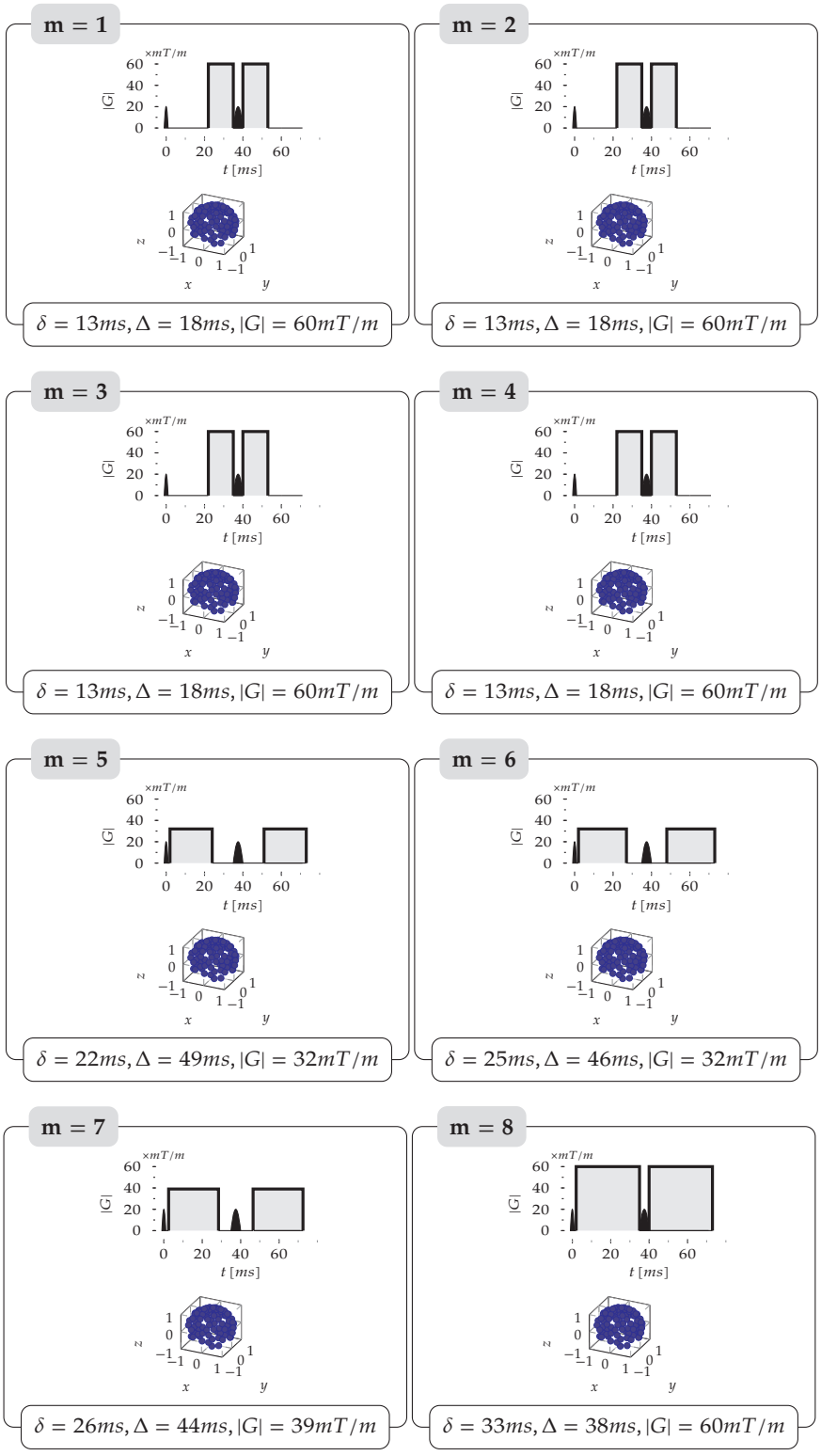

Figure 7.11: *SFPULSES protocol optimised for clinical gradient strength*

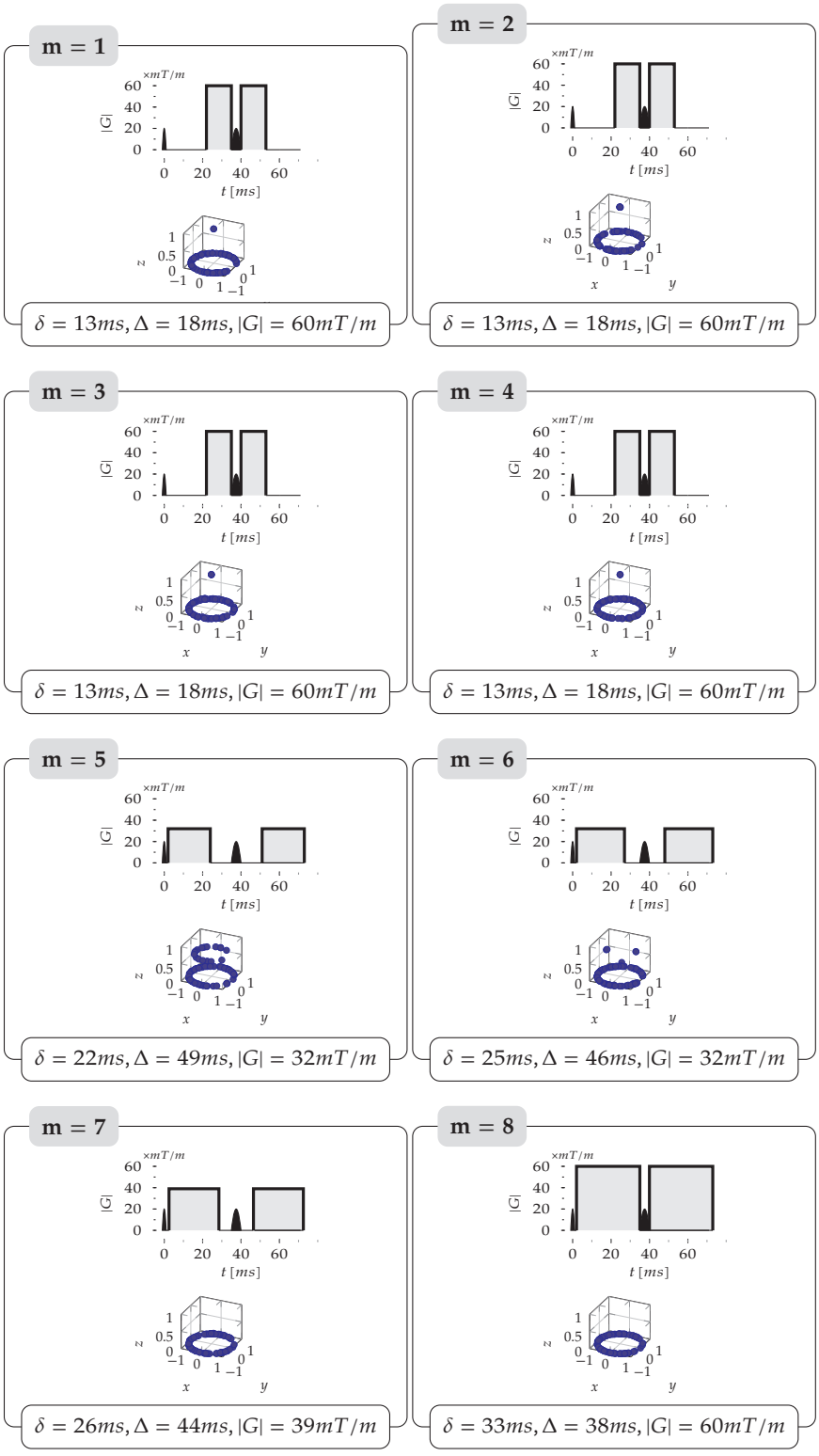

Figure 7.12: *SFDIRS protocol optimised for clinical gradient strength*

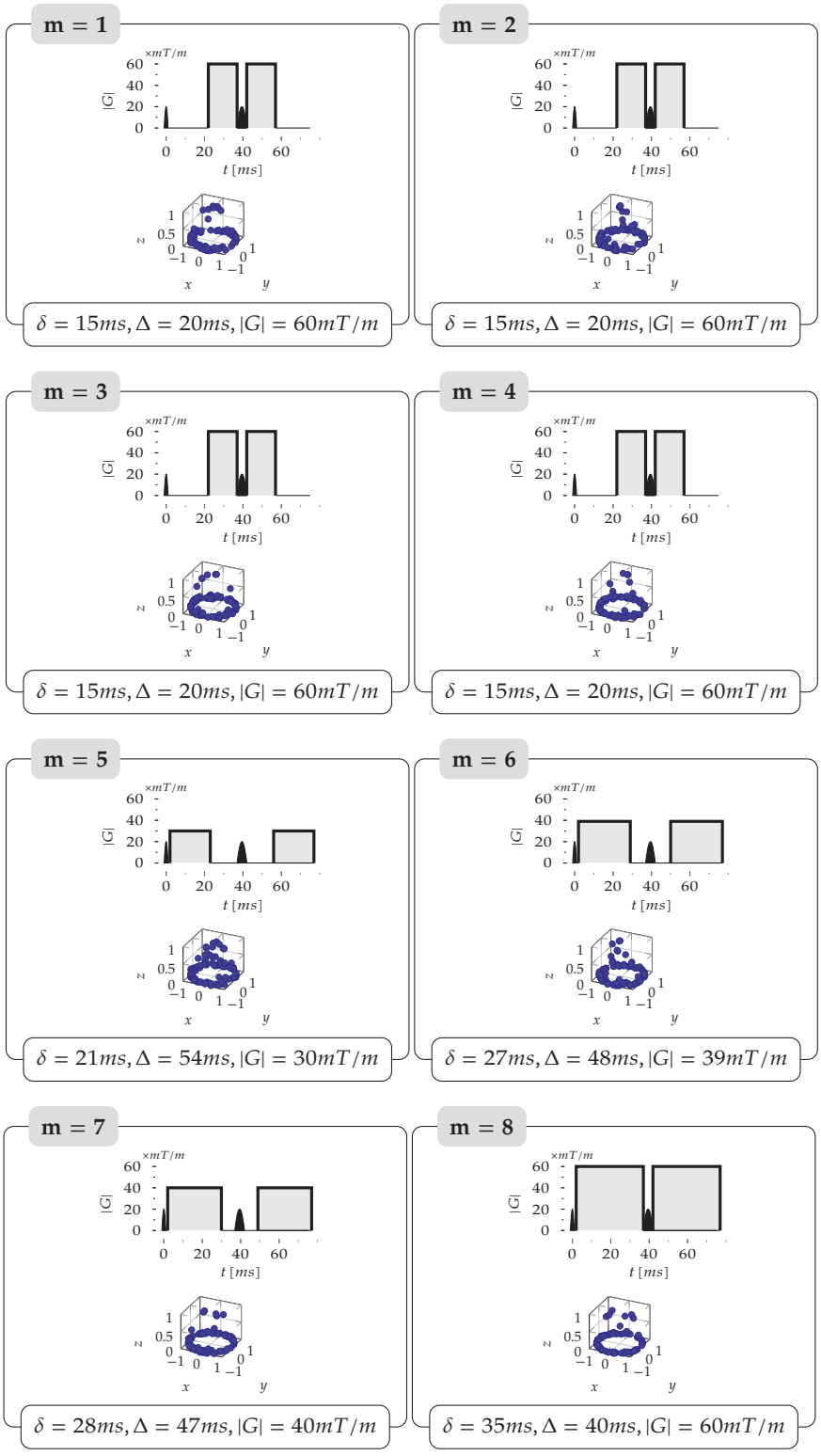

Figure 7.13: *SF protocol optimised for clinical gradient strength*

7.A.2 Pre-clinical scanner (300mT/m), N=30, M=4

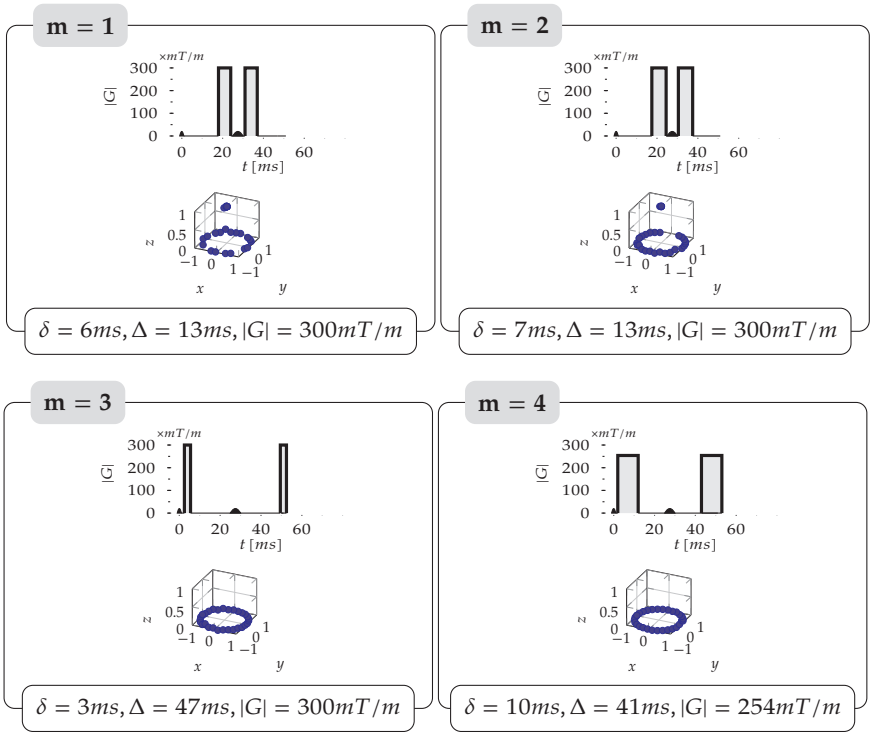

Figure 7.14: *SF protocol optimised for pre-clinical scanner and fixed tissue.*

8

Clinical feasibility of *in-vivo* estimates of axonal characteristics using optimised single fibre DWI protocol in the corpus callosum

8.1 Introduction

In the previous chapter we have introduced the single fibre SF diffusion MRI protocol optimisation framework designed for unidirectional white matter tracts. The aim of this chapter is to investigate the clinical feasibility of the SF protocols to estimate axon diameter and axon density indices *in-vivo*. Alexander et al. [4] has already shown that such indices can be acquired *in-vivo* on a standard clinical system, but the long scan time of 1 hour is excessive for routine clinical application.

We have already shown in simulations that SF protocols allow more accurate estimates of microstrucure indices in highly coherent WM bundles compared to the OI approach of Alexander [3]. We further demonstrated the feasibility of estimating a biologically reasonable range of axon diameter and axon density indices in a sample of fixed primate spinal cord. Our initial results suggest that SF protocols can produce acceptable estimates of tissue microstrucure indices using only a moderate number of diffusion weighted acquisitions.

Our aim is to produce a SF protocol that can be acquired within 25 minutes, which is comparable in scan time to a typical DTI protocol. We focus here on studying the effect of reducing the total number of diffusion weighted directions (SF) to accomodate the scan time limit. First, we compare our SF protocols with Alexander's OI approach using Monte Carlo (MC) simulations. We then evaluate both methods in an MRI scan/rescan experiment on two healthy volunteers to investigate the feasibility of estimating microstructural parameters *in-vivo* under realistic clinical conditions.

8.2 Asymptotic protocol optimisation

In the previous chapter we have implemented a SF protocol optimisation, given a total number of acquisitions N divided in M sets of different pulsed gradient spin echo (PGSE) pulse settings with the gradient scheme being either fixed OI or optimised for each set SF. Our simulations showed that protocols with optimised gradient schemes consistently outperformed the protocols with a fixed uniform gradient scheme. While the complete optimisation of all gradient directions offers great flexibility, it is also computationally very demanding. The increase in free parameters increases the computational complexity and thus requires much longer computation times compared to OI. The

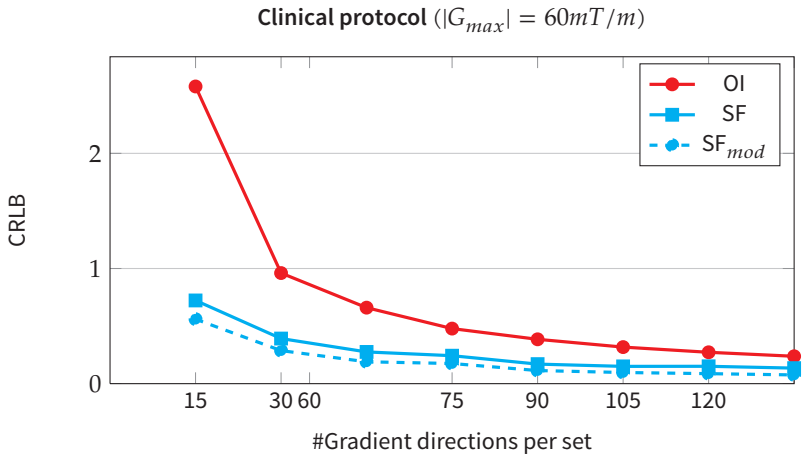

Figure 8.1: *Comparison of CRLBs between OI, SF and the modified SF$_{mod}$ protocols for different number N of gradient directions per set.*

larger parameter space also causes a higher risk for the algorithm to converge to a local minimum instead of the global minimum.

We observed in the previous chapter that the SF-optimised gradient schemes converged to a trivial arrangement of gradient directions, featuring predominantly perpendicular and parallel measurements to the given fibre direction. In fact, we can hypothesise that the few variations in gradient direction do not reflect the true optimal gradient scheme, but are caused by imperfections in the optimisation algorithm. To test this hypothesis, we can simply use the SF, presented in the previous chapter, to produce a modified SF$_{mod}$ protocol with only parallel and perpendicular gradients by aligning each gradient to the closest perpendicular or parallel gradient direction. Figure 8.1 compares the CRLB values for such a modified SF$_{mod}$ protocol compared to the untouched SF and OI protocols for different numbers of gradient directions. We can see that not only does the SF$_{mod}$ protocol achieve a similar improvement of CRLB values to SFover the OImethod, but it even gives the smallest CRLB values out of the three methods. We conclude that it suffices to use gradient schemes with only in-parallel and perpendicular gradient directions in our optimisation.

To reduce the complexity of the optimisation problem, we constrain our measurements in the protocol to have gradient directions only perpendicular to the fibre bundles, but we include one measurement in the parallel direction for the estimation of diffusivity along the axons. Such a gradient scheme contains exclusively either parallel or perpendicular measurements, and thus can be considered independent of the number of gradient directions N in each set M. We can therefore replace the optimisation for each pair of (N, M), with an asymptotic optimisation for $N \to \infty$ (in the following referred to as ASF). The ASF approach allows us to introduce the weighting factors w_m that reflect how important each measurement is, i.e. how often it should be sampled relative to the other measurements. We can then adapt Eq. 2.30 so that:

$$\Omega = diag\{w_1, \cdots, w_M\} \text{ with } \sum_{m=1}^{M} w_m = 1 \tag{8.1}$$

For any given desired discrete realisation of ASF for a total number of measurements N_{total}, we can simply calculate the number of acquisitions per set by $N_m = w_m N$. Table 8.1 summarises the optimisation parameters for the asymptotic protocol optimisation in comparison with the OI and SF methods described in the last chapter. It must be noted that the computational complexity of the ASF is only dependent on M, making it similar to the complexity of OI and significantly less computationally demanding than SF.

Table 8.1: *Overview of free and fixed parameters for the ASF protocol optimisation compared to SF and OI protocols.*

	ASF	OI	SF
Free parameters	$w_m, \delta_m, \Delta_m, G_m$	δ_m, Δ_m, G_m	$\phi_{m,n}, \theta_{m,n}, \delta_m, \Delta_m, G_m$
Fixed parameters	ϕ_n,θ_n	ϕ_n,θ_n	–
Specific fibre direction	yes	no	yes
No. of free parameters	$O(M)$	$O(M)$	$O(M \times N)$

8.3 Experiments & Methods

8.3.1 Protocols

We generate optimized protocols for our 3T Philips Achieva scanner with a maximum $|G|$ strength of $|\vec{G}_{max}| = 60mT/m$. We assume same two-compartment tissue model and parameter range we described in the previous chapter for the ASF design. The ASFprotocol optmisation is performed and we derive a protocol with a total of 90 diffusion weighted acquisitions (SF_{90}), which corresponds to the desired 25 minutes of scan time on our scanner. For comparison, we also generate an OIprotocol $N = 360$ (OI_{360}) as used in [4] and an ASFprotocol with the same number of acquisitions (SF_{360}). The three protocols are presented in table 8.2. The OI_{360} protocol optimisation uses $M = 4$ and report the three unique PGSE parameter settings. For the SF_{90} and SF_{360} protocols we increased $M = 8$ to avoid unneccessary constraints in the estimation of the asymptotic weighting factors. We only report here the 5 estimated unique PGSE parameters with $w > 0$.

8.3.2 Simulations

We use the free diffusion simulation of Hall et al. [62], which performs a Monte Carlo (MC) simulation of water particles in packed cylinders. We use the 44 synthetic white matter substrates from Alexander et al. [4] with diameter distributions and packing densities similar to previously reported histology studies [1, 61, 87].We perform the MC simulation with 50000 walkers and 20000 time steps for each protocol. For each substrate we generate 10 sets of noise-

Table 8.2: *PGSE settings of SF_{90}, SF_{360} and OI_{360} protocols. $\perp$ and $\parallel$ mark acquisitions perpendicular and parallel to the fibre bundles.*

(a) *SF_{360} and SF_{90} protocols*

N_m		Δ $[ms]$	δ $[ms]$	G $[mT/m]$	b $[s/mm^2]$	
70	18	0	0	0	0	
72	17	33.0	14.5	36.8	550	$\parallel$
38	10	22.4	15.9	60.0	1114	$\perp$
45	11	29.3	22.8	60.0	2908	$\perp$
68	17	48.0	26.6	43.7	3666	$\perp$
67	17	40.5	34.0	60.0	8692	$\perp$
360	90					

(b) *OI_{360} protocol*

N_m	Δ $[ms]$	δ $[ms]$	G $[mT/m]$	b $[s/mm^2]$
71	0	0	0	0
101	19.2	11.7	60.0	540
107	38.2	12.5	47.8	870
81	29.1	21.6	60.0	2634
360				

free MR signals and add Rician noise of $\sigma = 0.05$, resulting in a total of 440 sets of noisy MR signals. For each protocol we apply the model fitting procedure to the 440 sets of MR signals and retrieve the tissue model parameters.

Compared to the simple simulated substrates we used in the previous chapter, these substrates are more realistic and much less biased towards the tissue model that is used for fitting the observed signal. However, it is also more difficult to compare the ground truth axon diameter distribution with the fitted axon diameter index a. To compare the axon distributions with the estimated axon diameter index a, we have to take into consideration that the contribution of each axon to the MR signal depends upon its volume and is proportional to the square of its diameter. As in Alexander et al. [4] we correlate the estimated axon diameter index a with the weighted axon diameter average $\hat{a} = \hat{f} / \int p(\alpha)\alpha^3 \mathrm{d}\alpha$, where p is the true distribution of axon diameter α and $\hat{f}$ is the intracellular volume fraction $\hat{f} = \int p(\alpha)\alpha^2 \mathrm{d}\alpha$.

8.3.3 MRI experiment

The SF_{90} and OI_{360} protocols (see table 8.2) are implemented on our 3T Philips Achieva scanner to test the clinical viability of the 25 minute SF_{90} protocol and compare it to the three times longer OI_{360} protocol. Diffusion weighted MR images of two healthy volunteers (male 32yo, female 25yo) are acquired using a cardiac-gated EPI sequence with imaging parameters similar to the protocol described in [4]: 8 channel Philips head-coil, 10 slices, slice thickness=5mm, in-plane resolution=128×128 (FOV=35×35mm^2), TR=7RR, TE=125ms/TE=100ms for SF_{90} and OI_{360} respectively. We position the centre slice so that it is aligned with the mid-sagittal body of the CC to be able to acquire DWI measurements perpendicular and parallel to the fibres of the CC. SF_{90} acquisition is repeated twice on two separate days for each subject to investigate the reproducibility of the estimated parameter maps.

8.3.4 Model fitting

We use the three stage fitting algorithm as described in Alexander et al. [4], to fit the tissue model to the MR signal in each voxel. We increase stability by fixing $d_{\|}$ to $1.7 \cdot 10^{-9} m^2 s^{-1}$ and d_I is fixed to $3.0 \cdot 10^{-9} m^2 s^{-1}$[4, 9, 16]. The objective function is defined as the maximum likelihood of model parameters given the observed MR signals under Rician noise ($\sigma = 0.05$). An initial estimation is found using a coarse grid search algorithm over a set of physiologically possible parameters. Then a gradient descent algorithm further refines the parameter estimates. Finally a Markov Chain Monte Carlo (MCMC) algorithm with a burn-in of 2000, 50 samples at an interval of 200 provides posterior distributions of the parameters intra-axonal volume fraction (f_{intra}) and the axon radius r. An average over the MCMC samples provides the final parameter estimates. We report the axon diameter index $a = 2r$ and the axon density index $\rho = 4f_1 \pi^{-1} r^{-2}$.

8.4 Results

8.4.1 Simulations

Figure 8.2 presents the results from fitting the model to the synthetic MC datasets as described above. For all three protocols we plot the fitted axon diameter index a against $\hat{a}$ and the intra-cellular volume fraction f_1 against the true intra-cellular volume fraction $\hat{f}$ for all 440 noisy sets of MR signals. We also compute the mean over the 10 replications for each of the 44 unique substrates and display them in the same plot. The bottom row of Fig.8.2 shows that all protocols estimated the volume fraction accurately with little variance. Further, all protocols estimate larger radii a that agree with the $\hat{a}$ index. The estimated a varies arbitrarily between 0–2 μm for $\hat{a} < 3\mu m$. Thus smaller $\hat{a}$ can be distinguished from larger ones but not accurately measured. This is because of the limited maximum $|G|$ that does not attenuate the signal from water inside axons of diameter $< 2\mu m$. Despite the limitation, the trends of a agree with the true values for $\hat{a}$ and suggest that the index a is a useful discriminator of axon diameter distributions. SF_{360} estimates both indices more accurately than OI_{360} and variations among the 10 estimates in each substrate are smaller. SF_{90} and OI_{360} appear to have similiar accuracy and precision in estimating $\hat{a}$ and $\hat{f}$. This suggests that we can reduce the total number of acquisitions by a third by exploiting a-priori known fibre orientation without sacrificing the quality of the parameter estimates.

8.4.2 MRI experiment

Figure 8.3 shows maps of a and ρ in the centre slice of the CC for all acquisitions in two volunteers. From previous histological studies [1] we expected low axon diameter and high density in the splenium and genu and higher axon diameters with lower density in the body of the CC. As predicted by the MC simulations (see also Alexander et al. [4]), all protocols overestimated a because of the lack of sensitivity to lower diameters. The low-high-low trend in a and high-low-high trend of ρ can be observed in both subjects in OI_{360} results but are less apparent in SF_{90} scans. The worst case is seen in the result derived from SF_{90} in subject 1, which presents very noisy parameter maps. This is likely to be caused by a misalignment with the true fibre direction of the CC and the gradient directions, which demonstrates the sensitivity of the SF protocol to accurate positioning. Furthermore, all SF scans consistently produce larger estimates of a than OI_{360}. Variation in true fibre orientation is again the likely explanation. Unlike the SF protocols, the OI protocol can better compensate for this variation because of the high angular gradient sampling. However, despite the limitations, the results of subject 2 demonstrate reproducible estimates of a and ρ. This suggests that with accurate positioning, the 20 minute SF_{90} protocol is able to produce comparable parameter maps to OI_{360}, which requires more than three times the scan time.

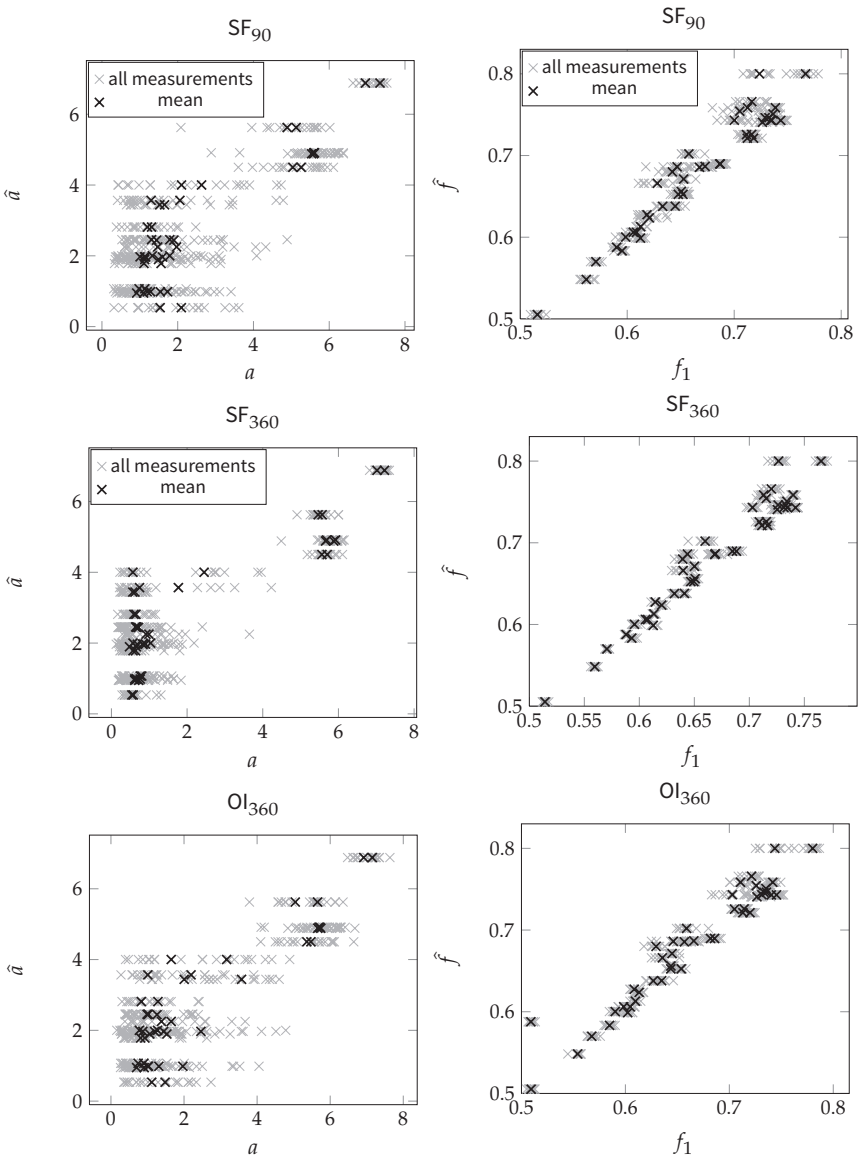

Figure 8.2: *Scatter plots of estimated tissue model parameters a and f_1 (grey) and and mean a and f_1 over 10 replications (black) against true $\hat{a}$ and $\hat{f}$ of the MC substrates.*

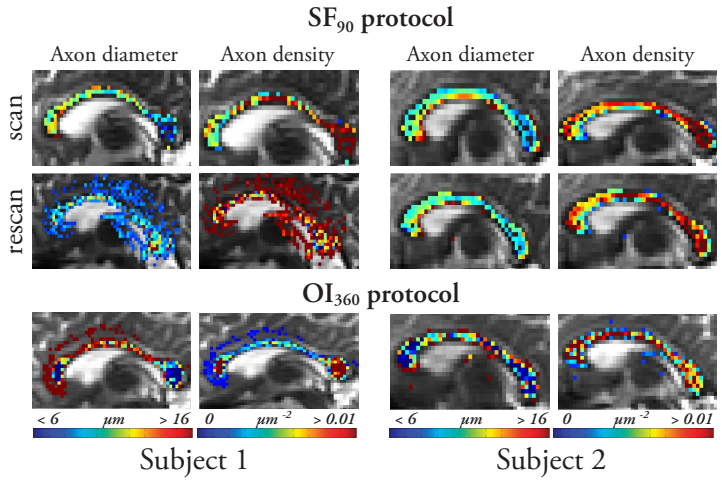

Figure 8.3: *Color coded parameter maps of a and ρ in the centre slice of the CC in two subjects. Scan and rescan results for the SF_{90} are shown together with results from the OI_{360} acquisition.*

8.5 Discussion

In this work we propose optimised Diffusion Weighted Imaging (DWI) protocols that use the known fibre orientation in specific structures like the CC and allow us to estimate indices of axon diameter and density in the live human brain. We develop a new optimization algorithm that overcomes several limitations of previous approaches and produces DWI protocols that can be acquired in under 20 minutes. While previous protocols were too time consuming for clinical practice, the short acquisition time of our protocols opens the possibility to be included in a variety of studies. Experiments on synthetic data show that our protocols can provide axon diameter and density indices with similar variance to those from longer orientation invariant protocols. *In-vivo* scans on two healthy volunteers show the potential of our method to produce parameter maps of axon diameter and density that agree with the general histological trend but also reveal the limitations caused by misalignment and variation in fibre orientation, compared to the longer OI protocol. If such protocols are to be used, great care must be taken to align gradient directions with the fibre orientation. The successful application of the SF, as well as the apparent shortcomings of the imaging protocol applied here, are the main motivation for the work presented in the next chapter. Building on the experiences we gathered in this initial *in-vivo* feasibility study, we will focus in the next chapter on improving the image quality and SNR of our parameter maps while addressing some of the most severe shortcomings of the present protocol, such as low spatial resolution and scan volume misalignment.

9

Viability and repeatability of *in-vivo* microstructure estimation in the corpus callosum and application to spinal cord

9.1 Introduction

In the previous chapter we have presented an implementation of our ASF optimised protocols on a clinical system. We found that the 25 minute long ASF acquisition can produce comparable results to the ≈3 times longer OI method. Our initial work was focussed only on the optimisation of the acquisition protocol. Clearly, however, other non-diffusion related imaging parameters, such as accurate positioning or spatial resolution, also contribute significantly to the goodness of the parameter estimates coming from our protocol. In this chapter we address several shortcomings of the initial ASF setup. Our main aim is to improve SNR and spatial resolution of our dataset in order to maximise accuracy and reproducibility of our microstructure maps.

In detail, we make the following changes compared to the ASF experiment described in Chapter 8:

1. We use a small FOV imaging sequence to increase image resolution and reduce distortions.

2. We develop a new method to better align the image volume with the dominant fibre direction of the CC using fast DTI tractography directly on the scanner console.

3. We extend the signal model used in the optimisation and fitting to allow the use of shortest available echo time (TE) for different combinations of δ and Δ, which will maximise SNR for each acquisition individually.

4. We increase the nominal maximal gradient strength to 87mT/m using the modified scanner software we developed for the QSI study in Chapter 6. Stronger gradients should aid the performance of the axon diameter parameters as shown by Dyrby et al. [44]. Stronger gradients also allow for shorter gradient pulses, which will further improve SNR.

We apply our new imaging pipeline in 5 healthy volunteers, who were scanned at two different timepoints to assess both intra- and inter-subject reproducibility. Furthermore we propose the first implementation of our ASF protocol in the cervical spine and test it in one healthy volunteer.

9.2 Protocol optimisation

We modify the ASF optimisation described in Chapter 8 by extending the tissue model to include an additional T2 decay factor that accounts for signal loss in the DWI with respect to the TE on a per-acquisition basis. For simplicity, we assume here a mono-exponential T2 decay of the signal. Previously, the TE was governed by the largest TE in the whole protocol. This modification now allows the dynamic use of TEs for different settings of δ and Δ in the protocol optimisation. This has the advantage of effectively reducing the TE in the low DWI acquisition, which greatly improves the SNR in those acquisitions.

We carry out the optimisation using the same parameters as described in the previous chapters (see Table 7.2 for details). We further assume T2=70ms, which is typical for WM in the CC at 3T field strength [140]. We also use our modified scanner software (described in Chapter 7), which allows us to combine several orthogonal 62mT/m-gradients to increase the maximum gradient strength to 87mT/m for the perpendicular gradients. The maximum gradient strength for the parallel gradient direction was 62mT/m. To improve the directional resolution required for the fit of the diffusion direction, we add a single shell DTI acquisition (max b=800s/mm^2, 1 b=0, 16 uniformly distributed directions) to the optimised protocol. The full set of parameters is given in Table 9.1.

Table 9.1: *Optimised protocol parameters for the ASF method with variable TEs. denotes number gradient direction samples parallel to assumed fibre direction (alternating between positive and negative directions). ⊥ denotes number of gradient direction samples perpendicular to assumed fibre directions (alternating between the four in the orthogonal gradient directions with maximum gradient strength (see Figure 6.1))*

	δ [ms]	Δ [ms]	G [mT/m]	b-value [mm/s^2]	TE [s]
1b0	0	0	0	0	23
1b0 + 5‖	8	22	62	340	46
1b0 + 14⊥	13	20	87	1430	54
1b0 + 7⊥	22	56	48	3870	96
1b0 + 26⊥	23	29	87	6090	73
1b0 + 20⊥	27	50	63	8457	93
1b0 + 11⊥	35	42	81	17380	93
1b0 + 16 DTI	b=800 s/mm^2			47	
				total scan time 35min	

9.3 CC reproducibility experiment

9.3.1 Data acquisition

We recruited 5 healthy volunteers (3 female, 2 male, mean age=28 $\pm$ 7) to be scanned on a Philips Achieva 3TX scanner. All subjects were recalled for a second scan on a different day to assess the intra-subject reproducibility of the experiment. In each scanning session we acquire the optimised DWI protocol given in Table 9.1 with the following scan parameters: voxel size: $1\times1\times4\text{mm}^3$, FOV=$96\times96\text{mm}^2$, TR=6000ms, 2 averages, using an outer-volume suppressed ZOOM acquisition [161] to avoid fold-over artifacts. The scan were performed in sagittal-oblique orientation, aligned with the AC-PC line.

The previous experiments have shown that our SF methods benefit from accurate alignment of the gradient scheme with respect to the dominant fibre direction. While standard T2w localizers are adequate to align the scan volume to anatomical reference, it offers no information about the WM fibre orientation. To aid slice positioning, we acquire a fast DTI scan in addition to the conventional scout scans. The scout-DTI imaging parameters are as follows: vo×elsize=$2\times2\times4\text{mm}^3$, 16 slices, FOV=$232\times232$ mm^2, TE=78ms, TR=4200ms, 6 non-colinear diffusion weighted directions (b=1000) plus one non-diffusion weighted image. Total scan time of the scout DTI scan is 57 seconds. We use the PRIDE tools directly on the scan console to place a region of interest (ROI) in the mid-sagittal slice of the CC and perform FACT tractography on the DTI dataset with default settings (FA threshold=0.45, angle threshold=0.15). The tracts are then overlayed on the colour-coded FA map, rastered, and resliced to obtain a new $1\times1\times1$ image volume. To plan the final SF scan, we use the axial and coronal views of the tractography results to adjust the angulation of the axial slices with respect to the observed tracts. Figure 9.1 shows an example of the final slice alignment based on both the structural localizer scan and tractography results. Since all processing steps of the whole scout-DTI are performed directly on the scanner console, the additional scan setup time for analysing the scout-DTI data is kept to a minimum.

9.3.2 Post-processing

We compensate for motion during the acquisition by aligning all scan volumes to the first b=0 image using the block-wise rigid registration algorithm [115] implemented in [105]. However, since the diffusion weighted images provide little contrast in non-coherently aligned WM tissue, we only register the interleaved b=0 images and apply the estimated transformation matrix to the subsequent intermediate b>0 images.

To ensure anatomical correspondence between scan and rescan, we then register the rescan dataset to the scan dataset (using rigid registration) using the transformation estimates from registering the first b=0 images of the two datasets. The transformation matrices for intra-scan motion and scan/rescan alignment are combined before applying them to the dataset to avoid unnec-

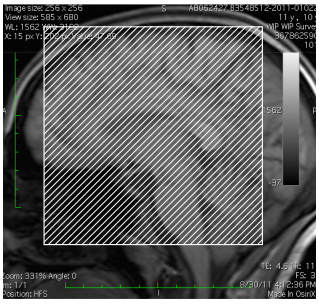

(a) Sagittal localizer

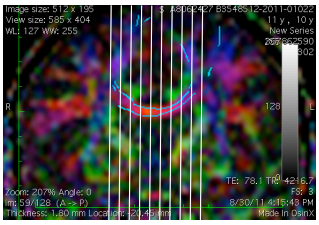

(b) Coronal FA map overlayed with tractography results (cyan lines)

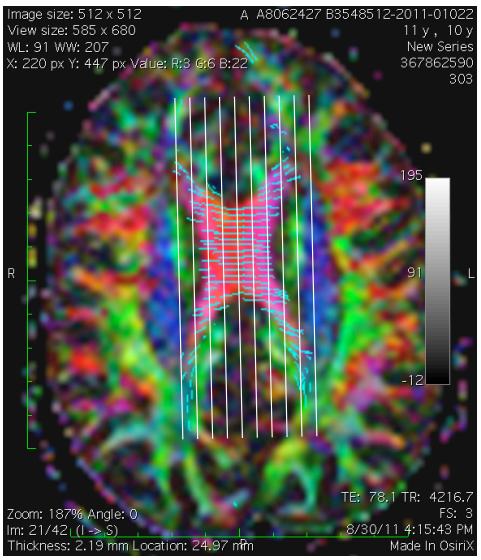

(c) Axial FA map with overlayed tractography results (cyan lines)

Figure 9.1: *Positioning of small FOV scans in white, overlayed on a sagittal scout image (a) and axial and coronal DTI tractography results (b&c).*

essary multiple interpolations. The data is then smoothed using the Unbiased-Non-Local-Means filter [148] with a small filter radius of $3 \times 3 \times 4mm^3$.

Data analysis

We use the same fitting procedure as outlined in the previous chapters. However since we allowed for variable TE in each acquisition, we need to account for the resulting differences in T2 signal decay within the data. We therefore estimate the voxel-wise mono-exponential decay curve using a linear regression model based on the non-diffusion-weighted acquisitions only. The predicted MR signal S from the tissue model is then adjusted based on its TEs by:

$$S' = S * exp(-TE/T2) \tag{9.1}$$

before the other model parameters are fitted. The adjusted signal S' is used to compute the rician log-likelihood with the observed signal as before. As in the previous studies, we compute the posterior distributions of the model parameters using an MCMC method on a voxel-by-voxel basis. From the mean of the posterior distribution we compute the axon diameter index a and axonal density index ρ=f/π/a^2. In addition we also fitted the diffusion tensor to the 16-direction DTI data and derive the principal eigenvector v_1 and scalar maps of FA, MD, AD, RD. All fitting is implemented using the Camino toolkit [37].

9.3.3 ROI analysis

In each subject we manually segmented the CC on the mid-sagittal slice on a non-diffusion weighted volume of the DWI dataset. We then removed all

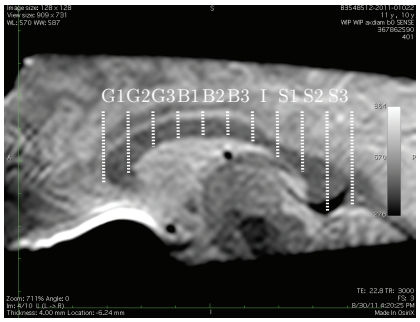

Figure 9.2: *Example of CC subdivision scheme overlayed on the midsagittal slice of a b=0 image in one volunteer. The ROIs divide the CC in genu (G1–G3), midbody (B1–B3), isthmus region (I) and splenium (S1–S3).*

voxels from the CC mask with FA<0.5 to exclude voxels with more than one single fibre orientation or significant CSF contamination. We further exclude voxels from the analysis where v1 deviated more than 10 degrees from the left-right fibre orientation that we assumed in the protocol optimisation. The CC segmentation is then divided in 10 equidistant regions along the anterior-posterior baseline similar to [1]. Figure 9.2 shows an example of the CC subdivision in one subject. Mean a and ρ indices are then computed for each CC subdivision in each of the 10 datasets. Scan/rescan agreement is assessed visually and is also quantified by computing the intraclass correlation coefficient (ICC) [134] over the whole CC and in each ROI. To investigate the correlation between DTI metrics and a and ρ, we pool all values in the CC ROI from all subjects separately for scan and rescan and report the robust correlation coefficient[69]. All statistical processing was performed using the software R[126] with packages 'ICC'[162] and 'robust'[153].

9.4 Spinal cord experiment

Data acquisition

We performed the scans for ASF as described above in the spinal cord of one healthy volunteers (42YO female). The SF DWI protocol was acquired with following scan parameters: voxel size: 1×1×5mm3, FOV=64×64mm^2, cardiac gated, TR=5RR, using the outer-volume suppressed ZOOM acquisition [161] as in the CC. We chose the 32-channel head coil to perform the scans as we found that it offers superior SNR in the cervical cord region than the dedicated 16-channel head-neck coil alternative. Scans were acquired between the discs C1/2 and C3/4, although severe motion artefacts made it necessary to exclude all except the 3 most caudal slices.

9.5 Results

9.5.1 Axon diameter and axon density indices in the CC

Figure 9.3 shows side-by-side scan/rescan maps of a and ρ for all five subjects. Figure 9.4 summarizes the mean a and ρ parameters measured in each ROI for all five subjects. In all subjects we can clearly see the variation along AP we expect from previous experiment, and earlier studies [4]. Furthermore, in comparison with those earlier results, our maps appear considerably less noisy and show improved contrast between different CC regions. Consistent with our previous results we estimate values of a in the range of 5–15μm. The largest a estimates are found in the midbody of the CC. The smallest a values are found in the splenium (<8μm) and the anterior part of the genu (9–11μm). The axon density index ρ is inversely related to the a trends, with ρ being largest in the anterior genu and posterior splenium regions and smallest in the body and isthmus of the CC. The a and ρ pattern we observe here agrees very well with the microstructure that is seen in excised human CC tissue samples[1].

Unlike in the previous experiments, the high spatial resolution here provides a large number of voxels that are completely contained in the CC. As a consequence, the CC can be easily distinguished from surrounding tissue and the tissue parameter estimates are less influenced by CSF contamination, particularly in the thinning part of the CC (B3–S1). This is beneficial for subjects with smaller CC such as found in s2 & s3, but becomes even more important in view of future applications in patients with neurological diseases such as MS or Alzheimer's disease, who often suffer from severe CC atrophy.

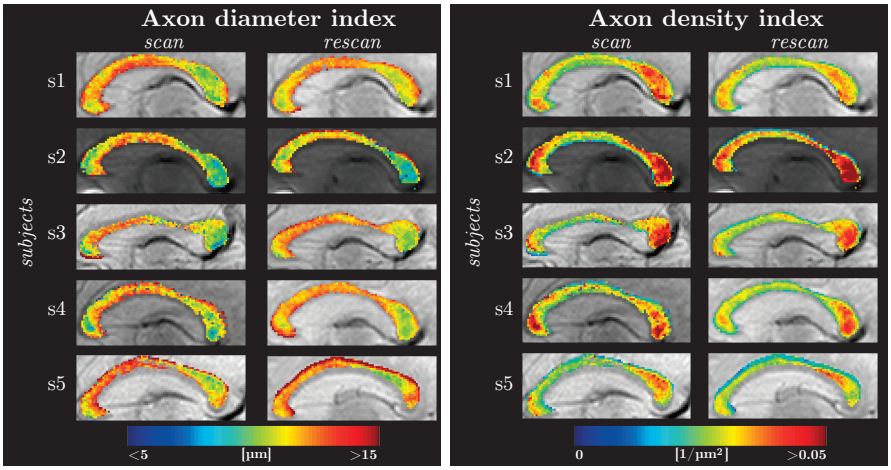

(a) (b)

Figure 9.3: *Individual maps of a and ρ in the sagittal slice for each subject for the scan and rescan experiments.*

9.5.2 Inter- & Intra-subject reproducibility

Results in Figure 9.3 and Figure 9.4 suggest good ROI consistency of the parameter maps between the five subjects. Furthermore, Figure 9.5 shows that

the average of a and ρ over all 5 subjects agree well between the scan and rescan experiment for all ROIs, both in the average trend as well as in the observed standard deviation. Moreover, both a and ρ show little variation from the mean over all subjects. Inter-subject variation is lower in the mid-body and the proximal genu regions (G2–G3) than in the more distal anterior and posterior regions. The Bland-Altman plots shown in Figure 9.6 show good reproducibility, i.e. the scan/rescan variation of the majority of ROI estimates centred around zero within the confidence interval of 1.5 standard deviations. In a minority of ROIs we see outliers with large scan/rescan variation. This appears to be related to large axon density estimates, which appear less stable than smaller ρ values. Those outliers appear mostly in the most distal G1 and S3 regions. Such large variations might indicate cardiac pulsation artifacts as these regions are closest to the adjacent Arteria Cerebralis. In a the scan/rescan variability appears more independent of the actual estimation values.

Table 9.2 presents the ICC for whole CC and its subdivisions. For both a and ρ, we find the scan/rescan agreement being 'moderate' or better for both whole CC values and most ROIs. As noted before, the lowest ICC values are found in boundary regions (G1) or in the thin proximal part of the CC, which are most affected by imaging and analysis artefacts. Both Bland-Altman analysis as well as the ICC values suggest that the estimated values in those ROIs appear more prone to error and must be interpreted with caution.

Table 9.2: *ICC values for whole CC and individual ROIs for a and ρ estimates.*

		Individual ROIs									
	whole CC	G1	G2	G3	B1	B2	B3	I	S1	S2	S3
a	0.66	0.14	0.83	0.56	0.14	0.81	0.46	-0.25	-0.07	0.70	0.94
ρ	0.79	0.74	0.77	0.78	0.44	0.59	0.34	0.79	-0.14	0.34	0.73

Guidelines for agreement [88]: < 0.2: poor, 0.2–0.4: fair, 0.4–0.6: moderate, 0.6–0.8: substantial, > 0.8: almost perfect

Correlation with DTI metrics

Figure 9.7 presents the correlation between the standard DTI metrics and the a and ρ estimates. The correlations we see here agree with the findings of [16] and [4]. Correlations are found between FA and both microstructure indices of a and ρ. While *MD* is not correlated with either of the microstructure indices, the directional diffusivities AD and RD both show moderate correlations with a and ρ. Of course it is not surprising to find RD positively correlated with a and negatively correlated with ρ respectively, as it is known that axonal packing density and axon diameter both influence RD measurements [20]. The observed correlation between AD and a (negative) and ρ (positive) is less intuitively explainable, however it is consistent with previous findings [4, 16]. Alexander et al. speculate that the increase of axon size and decrease of packing density are associated with lower fibre coherency, and thus are causing an increasing amount of diffusion impedance along the dominant diffu-

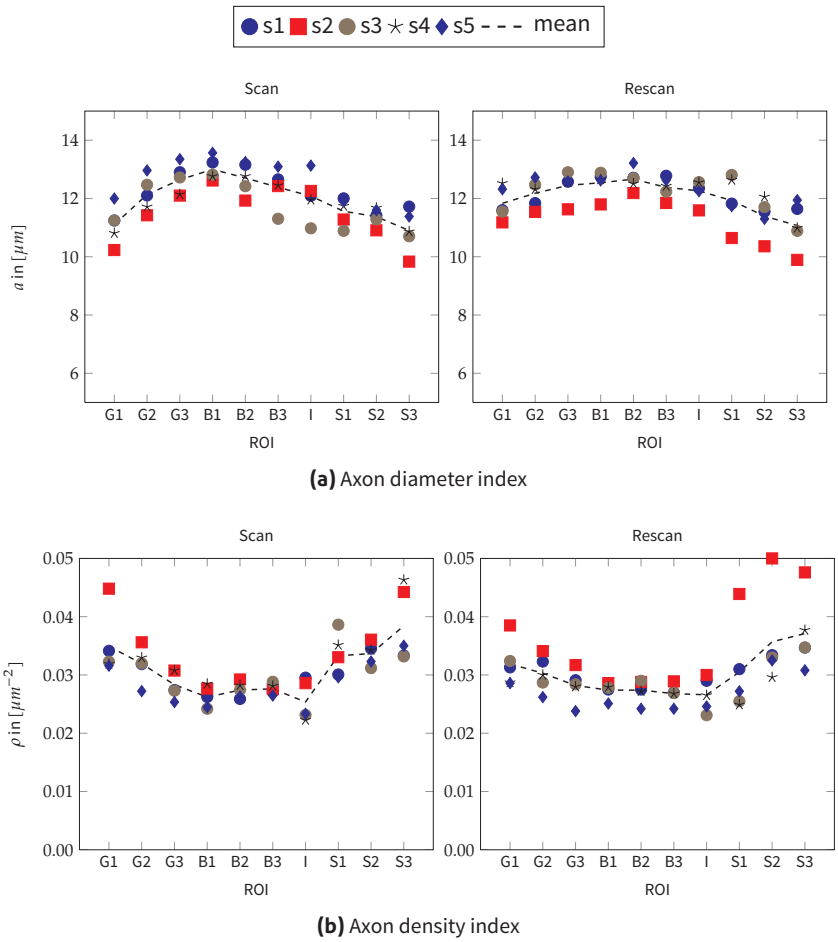

(a) Axon diameter index

(b) Axon density index

Figure 9.4: *Scatter plots of axon diameter (a) and axon density (ρ) indices in all 5 subjects in individual ROIs. The dashed line shows the average over all subjects.*

sion direction. Although spatial resolution has been greatly improved compared to previous experiments, the correlation between AD and the a and ρ indices might still be influenced by residual CSF contamination, since the region's largest axon diameters are mostly found in the thinner mid-body region, which might be more affected by partial volume effects coming from motion or eddy-current distortions than those in the larger genu and splenium regions.

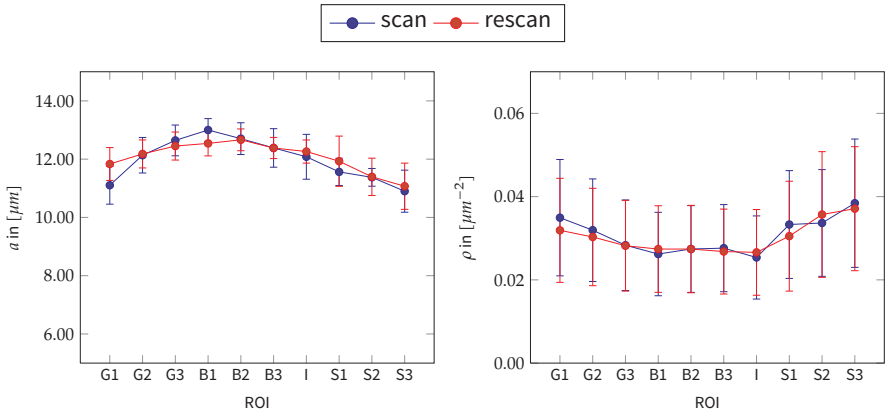

(a) Axon diameter index **(b)** Axon density index

Figure 9.5: *Average and standard deviation a and ρ over the whole group of 5 subjects for different ROIs.*

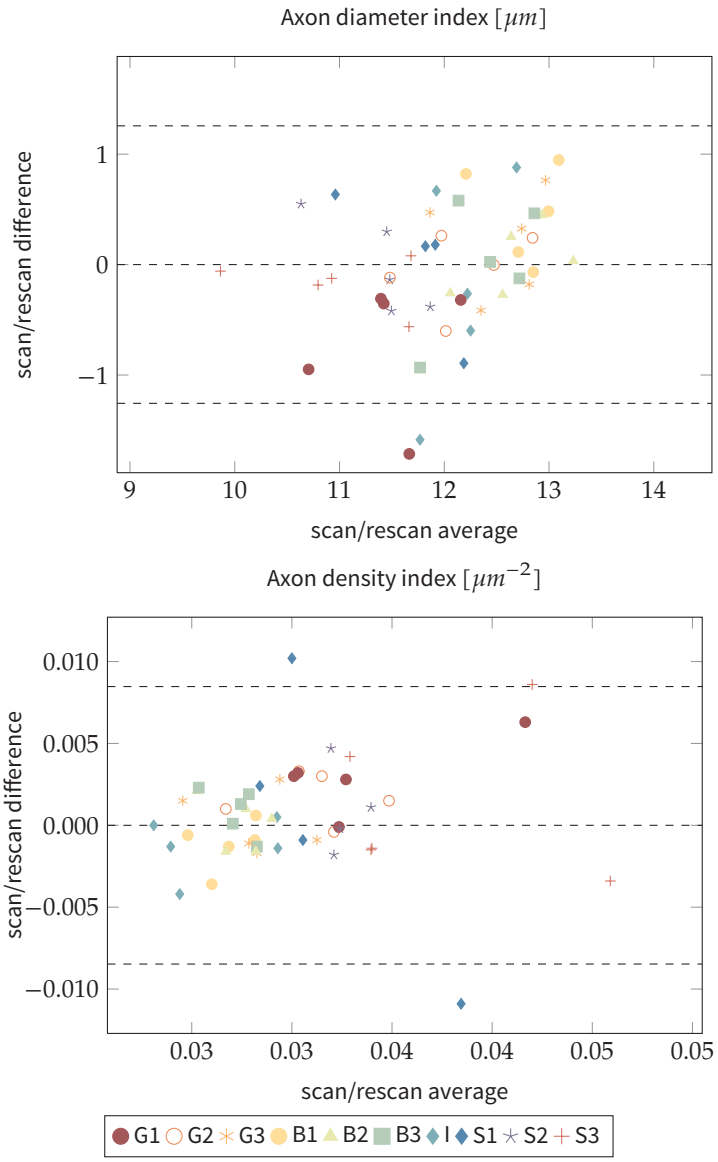

Figure 9.6: *Bland-Altman scan/rescan reproducibility analysis of a and ρ in all CC ROIs.*

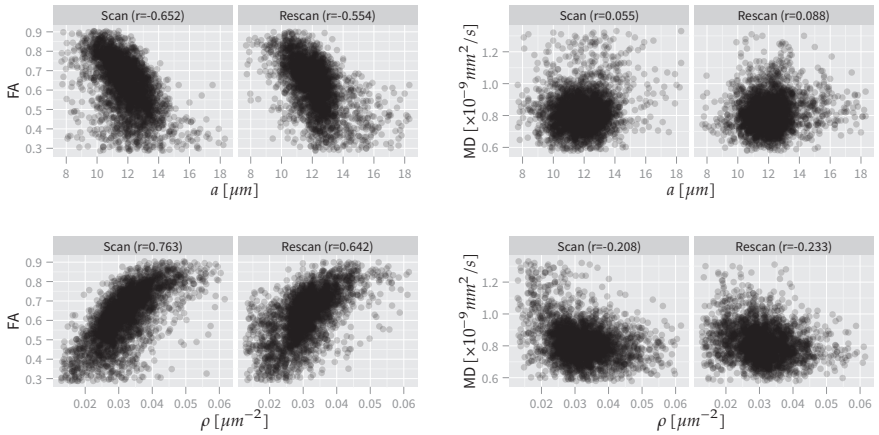

(a) FA

(b) MD

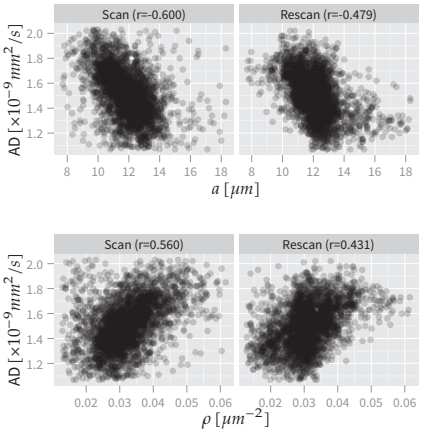

(c) AD

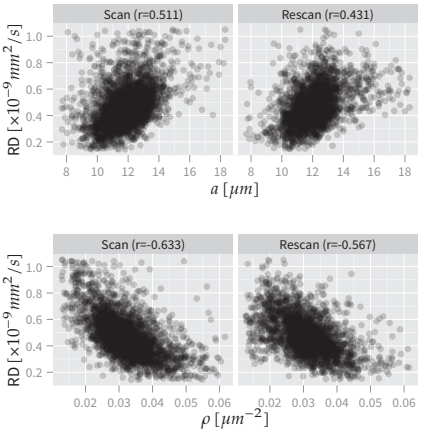

(d) RD

Figure 9.7: *Scatterplots of DTI metrics and a and ρ. The r value denotes the correspondenceding correlation coefficient.*

Axon diameter and axon density indices in the SC

Figure 9.8 shows the a and ρ maps acquired in one healthy volunteer. Gray matter areas are excluded here as they are clearly violating the single fibre assumption of our method. We clearly see the bilateral symmetry of the parameter maps, as expected from the basic anatomy of the spinal cord. The estimates of a and ρ indices are within a similar range of values measured in the CC. Furthermore, both a and ρ allow good discrimination between motor and sensory WM tracts. The largest a ($10.7 \pm 2\mu m$) and lowest ρ ($0.035 \pm 0.017 \mu m^{-2}$) are found in the lateral tract. The dorsal sensory tract shows the lowest a ($9.1 \pm 1.3 \mu m$) and highest ρ ($0.046 \pm 0.017 \mu m^{-2}$). The contrast between LT and DC is consistent over several slices in our dataset and agrees with our earlier findings in fixed monkey cervical cord. Figure 9.8 also illustrates clearly the challenges in SC imaging. The posterior halo of low a is the result of motion artefacts during the acquisition, which can be caused by swallowing or breathing. Cardiac motion also makes cardiac gating a necessity, which in turn limits the amount of data we can acquire within the 25 minute windows and consequently reduces the SNR in our data. However, the results here show first evidence that our ASF protocol can be used successfully in the SC application, despite the more challenging imaging environment.

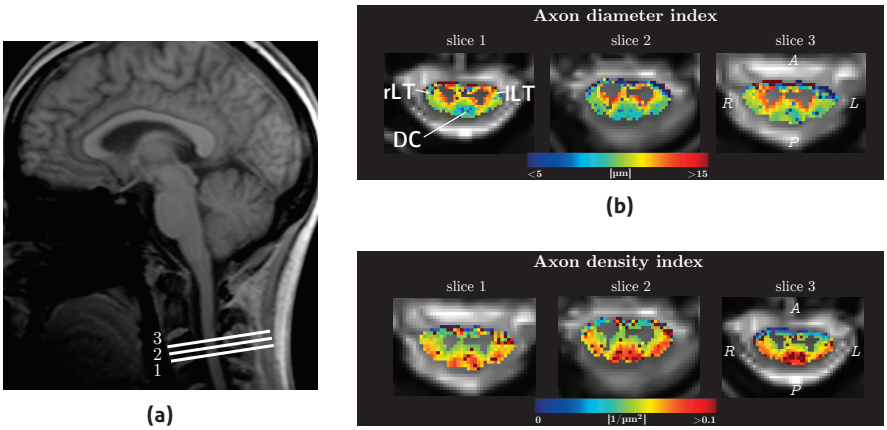

Figure 9.8: *(a) SC slice alignment and (b&c) maps of a and ρ in one healthy volunteer. Annotations on the first result slice denote the location of the dorsal column (DC) and left and right lateral tracts (LT).*

9.6 Discussion

This work presents a novel imaging and analysis pipeline for measuring axon diameter and density indices in the CC *in-vivo*, which expands on the ASF protocol optimisation that we introduced in the previous chapter. We combined small FOV imaging and careful optimisation of the MR protocols and post-processing techniques to gain both high spatial resolution while maximising SNR. We show here axon diameter and axon density maps of better quality than in previous studies. For the first time we present results of a larger subject

cohort of 5 subjects, allowing us to infer scan and rescan reproducibilty with more confidence. Our results show that a and ρ show very good reproducibility consistently over all investigated subjects. Furthermore, a first test of our protocol in healthy cervical cord *in-vivo* in humans produced compelling results that are in good agreement with our findings in excised monkey cervical cord.

9.6.1 Limitations & further work

Interpretation of a and ρ: The model we use here is a very simplistic approximation of the complex micro-anatomy of real biological tissue. The actual estimates of axon diameter and densities differ considerably from what is expected from histology or ex-vivo scans [4], which show much more prevalence of small calibre axons (1-3μm) in the CC. Most of this disparity can be explained by the limited gradient strength available on the clinical system. With limited gradient strength, small axons cause very little signal attenuation and become indistinguishable from each other [91, 164]. Our simulation experiments in Chapter 7 show a limit of sensitivity of of 2–4μm even in the very idealised situation of perfectly aligned single-radius cylinders. Consequently, the a and ρ indices must not be seen as accurate reflections of the complete axon diameter distribution as they are likely driven only by a small number of large axons in the WM. Furthermore, it does not consider the effect of dispersion[167] or undulation[110], which both have been shown to affect the observed diffusion pattern in axonal fibre bundles.

Other more complex models have been also been suggested, which add more tissue compartments, a model of dispersion fibre bundles, a distribution of axon diameters and/or permeable membranes. However, with the given limits both in scan time and gradient hardware, their practical value for *in-vivo* clinical applications is questionable. Recently, those more complex models in the CC WM tissue have been systematically studied with much more extensive datasets than we used here, by Panagiotaki et al. [118] in fixed rat CC and Ferizi et al. [54] in live human CC. Both studies suggest that a simple two compartment model similar to ours explains diffusion in coherent WM tissue reasonably well. For our purpose of clinical adoption, this model provides the best trade-off between explaining the diffusion in WM while keeping data requirements reasonably low. Furthermore, the shorter protocol we propose is an important step to enable more widespread adaptation of our imaging pipeline, which in turn will lead to better understanding of the interpretation of its parameters.

Furthermore, alternative acquisition methods such as oscillating gradients [35, 41] or multiple wave-vector acquisitions [11, 83, 84] promise more sensitivity to smaller axon diameters. Recently the protocol optimisation framework has been extended to support such non-rectangular gradient waveforms [43, 136]. The method we present here is easily combined with any other pulse sequences to provide better discrimination of small axon diameters.

T2 estimation: We chose here to estimate T2 directly from the b=0 weighted images. Using this approach, we are limited to estimating rather high TEs due to the nature of the single shot EPI technique used here. Furthermore, due to the sparsity of the samples of TE, we can only account for mono-exponential T2-decay. A more comprehensive T2 decay curve could potentially be estimated using the Carr-Purcell-Meiboom-Gill (CPMG) sequence [121]. However, this approach would add significant scan time to our protocol. Furthermore, such acquisition does not suffer from the same image distortions as the EPI DWI images and therefore requires further registration, which might confound the results. Nevertheless, a better T2 decay curve estimate might also be used to correct for T2 differences between intra- and extra-axonal compartments. Fitting a single T2 to all compartments could lead to errors in the f_{intra} estimates and might have an effect on our ρ parameter maps. While we focussed on a single-compartment T2 estimation to simplify fitting, our tissue model can easily incorporate different T2s for individual compartments.

Validation: We have validated our results here by comparison with previous reports of tissue parameter estimates by diffusion MRI and independent histopathology. While several systematic reports of the tissue microstructure in the CC are available, validation of our results is more complicated in the SC as its axonal morphology in primates is less well documented. Further work is required to provide a direct comparison between our MRI parameters and independent histology for a better interpretation of our estimated parameters in healthy tissue, but more importantly in the presence of pathological tissue alteration. Following our initial work on ASF, we are now in the process of setting a validation study of our protocol using post-mortem human spinal cord of healthy and MS tissue in collaboration with Dr DeLuca from the Nuffield Department of Neurosciences, University of Oxford.

Clinical application: The protocols we present here are designed with clinical adaptation in mind. Due to the short acquisition time, our 25 minute protocol can be easily incorporated into existing studies. A disadvantage of our method is that it does not offer whole brain coverage. However, the alternative OI method is also intrinsically limited by the tissue model to application in highly coherent WM structures. In fact, if only such structures are to be studied, our method provides much better spatial resolution and SNR in shorter acquisition time. Furthermore, many neurological diseases such as Alzheimers disease, Schizophrenia or MS have a severe impact on the CC and diagnosis. In those diseases, diagnosis and therapy monitoring might benefit from better tissue characterisation. Encouragingly, the first results in the SC we showed also promise for future application in the cord, e.g. to gain better biomarkers for diagnosis and therapeutic outcome in SCI. Wider application in other parts of the CNS might come from the more complex tissue models which incorporate fibre dispersion and fibre crossing [138, 166, 167, 169].

9.7 Conclusion

We have demonstrated that our microstructure estimates agree with reported post-mortem evaluation of the CC fibre density distribution. Further, we showed good inter- and intra-subject reproducibility. The scan time of the protocol is short enough to be easily incorporated into clinical studies. In future work, we are planning to use this approach in subjects with known altered microstructure of the CC.

10

Conclusions

The overarching aim of this dissertation was to develop imaging markers that can be helpful in the clinical assessment of spinal cord pathologies such as traumatic spinal cord injury (SCI) and Multiple Sclerosis (MS). In several studies we have explored both established methods such as estimation of the apparent diffusion coefficient (ADC) and DTI as well as more experimental approaches such as QSI and the ActiveImaging framework.

In Chapter 3 we have devised a new imaging protocol to visualize and quantify collateral nerves in the cord with DTI. While the size of the study was small, we developed a sound methodical framework for DTI acquisition and processing in the cord, which proved helpful for any analysis of SC data beyond the scope of the study itself. The observations in this study also lead to the development of a novel partial volume correction method for whole cord averages of whole-cord DTI metrics. We showed our PVA correction helps to reduce bias in average whole cord DTI metrics and improves inter-subject variability. The achievable resolution in SC DWI is low and PVA is a common problem for all SC DWI techniques. In addition we have presented an example of a successful application of our partial volume average (PVA) correction method for the analysis of DTI data acquired in chronic SCI patients.

In chapters 5&6 we turned towards QSI, which offers the theoretically the most complete description of the diffusion process in any tissue. However, in practice the setup and analysis of *in-vivo* QSI is very challenging, and only few QSI studies have been reported in *in-vivo* human SC so far. For the first time we presented here a systematic study of inter- and intra-subject variability of QSI measures over the whole cord area and specific white matter tracts in cervical cord. We demonstrate that variability and reproducibility of QSI metrics is very good, and, as shown in Chapter 6, can be improved even more when combined with modern scanner hardware and a carefully optimised SC imaging set-up. We were unable to reproduce the clear distinction between WM tracts in the cord as seen in *ex-vivo* high-field MRI experiments by Ong et al. [113]. However QSI metrics in different white matter tracts complemented conventional ADC estimates when distinguishing features of different white matter tracts. While we were not able to demonstrate a clear advantage of QSI in healthy SC over conventional analysis, QSI might be more sensitive to WM damage such as Wallerian degeneration, as shown by Farrell et al. [49] in a rat axotonomy model. Future work will explore the feasibility of QSI to such SC pathologies *in-vivo* under realistic clinical conditions, in a similar fashion to our study of healthy SC we presented here. The QSI protocols and analysis pipeline we presented in chapters 5 and 6 for two different scanners are currently in use at the two sites to study different spinal cord patient cohorts:

(1) patients with brachial plexus avulsion scanned at the Wellcome Centre for Neuroimaging, UCL, using the Siemens Trio 3T system (2) MS patients as part of a longitudinal study at Department of Neuroinflammation, UCL Institute of Neurology using the Philips 3T TX Achieva machine.

Finally, we presented in chapters 7–9 a new imaging method, that is specifically designed to provide direct estimates of axon diameter and density indices in structures with known single fibre orientation such as the SC. We thoroughly evaluated our method, going from using computer simulation via *ex-vivo* monkey spinal cord samples to application in live humans, first in the corpus callosum and finally the spinal cord. We demonstrate that our method produces very repeatable maps of axon diameter and axon density indices with very good SNR. However, the key achievement here is that our proposed protocol can be acquired in ≈30 minutes, which is crucial for future adoption into clinical studies and far shorter than similar microstructure imaging approaches such as AxCaliber[9]. Our method extends naturally to different models or imaging sequences. We intend to extend the algorithm constraints of strictly unidirectional fibre directions to incorporate some degree of dispersion for a more realistic representation of healthy and pathologic white matter. We are also planning to use our protocols to study *ex-vivo* healthy and MS human cord to better understand the role of our parameter estimates in the presence of tissue alteration. In the long term, our method must be evaluated in the context of a larger clinical study, e.g., of SCI to determine further its clinical benefit for SC disease diagnosis and management purposes.

A common theme that emerged from all the work we presented here is the importance of a holistic approach in optimising the imaging pipeline to the desired DWI method and vice versa. We have demonstrated the clear benefits of adapting the acquisition protocol to the specific DWI analysis (e.g. in Chapter 3 and Chapter 7). On the other hand we have also shown, e.g. in chapters 6 and 9 that a careful optimisation of the imaging parameters themselves, such as image quality and positioning are equally important for any successful DWI study. We believe that our contributions meet the initial goal of this thesis to improve existing acquisition protocols and analysis methods, and to devise new imaging biomarkers for the study of SC with diffusion MRI.

Part IV

Appendix

A

Degeneration of injured cervical cord is associated with remote changes in corticospinal tract integrity and upper limb impairment

OPEN ACCESS Freely available online

PLOS ONE

Degeneration of the Injured Cervical Cord Is Associated with Remote Changes in Corticospinal Tract Integrity and Upper Limb Impairment

Patrick Freund[1,2,3,4*☯], Torben Schneider[5☯], Zoltan Nagy[2], Chloe Hutton[2], Nikolaus Weiskopf[2], Karl Friston[2], Claudia A. Wheeler-Kingshott[5], Alan J. Thompson[1]

1 Department of Brain Repair and Rehabilitation, University College London Institute of Neurology, University College London, London, United Kingdom, **2** Wellcome Trust Centre for Neuroimaging, University College London Institute of Neurology, University College London, London, United Kingdom, **3** Spinal Cord Injury Centre, Royal National Orthopaedic Hospital, University College London, London, United Kingdom, **4** Swiss Paraplegic Research, Nottwil, Switzerland, **5** NMR Research Unit, Department of Neuroinflammation, University College London Institute of Neurology, University College London, London, United Kingdom

Abstract

Background: Traumatic spinal cord injury (SCI) leads to disruption of axons and macroscopic tissue loss. Using diffusion tensor imaging (DTI), we assessed degeneration of the corticospinal tract (CST) in the cervical cord above a traumatic lesion and explored its relationship with cervical atrophy, remote axonal changes within the cranial CST and upper limb function.

Methods: Nine cervical injured volunteers with bilateral motor and sensory impairment and ten controls were studied. DTI of the cervical cord and brain provided measurements of fractional anisotropy (FA), while anatomical MRI assessed cross-sectional spinal cord area (i.e. cord atrophy). Spinal and central regions of interest (ROI) included the bilateral CST in the cervical cord and brain. Regression analysis identified correlations between spinal FA and cranial FA in the CST and disability.

Results: In individuals with SCI, FA was significantly lower in both CSTs throughout the cervical cord and brain when compared with controls ($p \leq 0.05$). Reduced FA of the cervical cord in patients with SCI was associated with smaller cord area ($p = 0.002$) and a lower FA of the cranial CST at the internal capsule level ($p = 0.001$). Lower FA in the cervical CST also correlated with impaired upper limb function, independent of cord area ($p = 0.03$).

Conclusion: Axonal degeneration of the CST in the atrophic cervical cord, proximal to the site of injury, parallels cranial CST degeneration and is associated with disability. This DTI protocol can be used in longitudinal assessment of microstructural changes immediately following injury and may be utilised to predict progression and monitor interventions aimed at promoting spinal cord repair.

Citation: Freund P, Schneider T, Nagy Z, Hutton C, Weiskopf N, et al. (2012) Degeneration of the Injured Cervical Cord Is Associated with Remote Changes in Corticospinal Tract Integrity and Upper Limb Impairment. PLoS ONE 7(12): e51729. doi:10.1371/journal.pone.0051729

Editor: Bing Hou, Beijing Institute of Radiation Medicine, China

Received June 16, 2012; **Accepted** November 5, 2012; **Published** December 12, 2012

Funding: This study was supported by the Swiss National Science Foundation (Grant No: PBFR33-120920), Schweizerische Stiftung für medizinische und biologische Stipendien (Grant No: PASMP3-124194), the Swiss Paraplegic Research (Nottwil) and the Wellcome Trust. This work was undertaken at University College London Hospitals/University College London, which received a proportion of funding from the Department of Health's National Institute for Health Research Biomedical Research Centers funding scheme. The funders had no role in study design, data collection and analysis, decision to publish, or preparation of the manuscript.

Competing Interests: The authors have declared that no competing interests exist.

* E-mail: p.freund@ucl.ac.uk

☯ These authors contributed equally to this work.

Introduction

Trauma to the spinal cord leads to retrograde and anterograde degenerative changes of central pathways [1–3]. Thus, axonal information flow is impeded and motor neurons below the site of injury are often deprived of supraspinal input [4]. This persistent lack of descending input may hinder clinical recovery. Recently, we and others showed that, following injury, the axonal and myelin integrity of the cranial corticospinal tract (CST) are reduced in specific motor areas [1,2,5] and correlate directly with spinal atrophy and cortical motor reorganisation. Moreover, the extent of spinal atrophy relates directly to disability [1,6]. To explore these findings further we need to address the following questions: (1) How do the intrinsic changes within the atrophic spinal cord relate to central axonal changes in the cranial CST; (2) Does that degree of intrinsic spinal changes relate to manual dexterity independently of spinal atrophy [1].

Trauma induced microstructural tissue changes, although not visible on conventional MRI scans, alters free water diffusion [7] and this can be quantified by diffusion tensor imaging (DTI) [8]. In particular, fractional anisotropy (FA) has been reported as a marker of both axonal count [9] and myelin content [10]. We used this method in a cohort of SCI patients in the cervical cord as well as in the brain to investigate the degree of trauma-related

abnormalities within cranial and spinal parts of the CST. DTI of the brain was thoroughly investigated in a previous report [5]. To answer our questions about the anatomical and behavioural correlates of white matter integrity at the spinal level, we use regression analysis to investigate the relationships between (1) the cross-sectional spinal cord area (i.e. spinal atrophy) measured with anatomical MRI, (2) changes in FA in the cervical cord and cranial CST measured by DTI, (3) clinical assessment of upper limb function.

Subjects and Methods

Subjects

From the same SCI patient cohort as previously reported [1,5,11], we studied ten male subjects, (level of lesion C5 to C8, mean age 45.7 years, post injury 14.9 years) who had bilateral upper and lower limb impairment (mean ASIA motor score 21.95). SCI subjects had no head or brain lesion associated with the trauma, or any history of seizure, medical or mental illness. All participants were free of MRI contraindications.

We also recruited ten gender matched right-handed healthy subjects within the same age range (mean age = 38.8 yrs, SD = 15.5, range = 25−65; p = n.s.) without any history of neurological or psychiatric illness.

Prior to the study, all participants gave informed, written consent. The study was approved by the Joint Ethics Committee of the Institute of Neurology at University College London and the National Hospital of Neurology and Neurosurgery, UK (ref: 08/0243).

Clinical Assessment

All participants were assessed clinically using the 9-Hole Peg Test (9HPT) bilaterally [12]. Their maximum voluntary contraction (MVC) and performance on the Arm Action Research Test (ARAT) were tested with their dominant hand. The reciprocal of the average of two trials – for each hand of the 9HPT – and the average of two trials of the MVC were recorded. In three SCI subjects, the 9HPT was scored with the maximum time allowed for the 9HPT (300 sec) [13] as they were unable to perform with their non-dominant hand. To assess differences in motor performance between SCI subjects and controls, a two-sample t-test was used. A p-value$<$0.05 was considered significant.

Image Acquisition

T1-weighted scan of brain and spinal cord. An optimized 3D-MDEFT sequence was used to obtain T1-weighted (T1w) structural images of the whole brain, brainstem and cervical cord (down to C5) [14] on a 1.5 T whole-body Magnetom Sonata MRI scanner (Siemens Medical Systems, Erlangen, Germany). The scan parameters were: isotropic 1 mm^3 resolution, FoV 256×256 mm^2, matrix 256×256, 176 sagittal partitions, repetition time = 12.24 ms, echo time = 3.56 ms, inversion time = 530 ms, flip angle 23°, fat saturation, bandwidth 106 Hz/Pixel. The acquisition time was 13 min 43 sec.

Diffusion tensor imaging (DTI) of the cervical cord. DTI was performed using a single shot echo planar imaging (EPI) sequence using the twice refocused spin-echo method for diffusion encoding [15]. The cervical cord data set consisted of 68 images: 7 images with a low b-value of 100 $s*mm^{-2}$ and 61 directions with a high b-value of 1000 $s*mm^{-2}$. The diffusion gradient directions in both subsets were uniformly distributed over the sphere according to [16]. The image volumes consisted of 20 axial slices with thickness of 5 mm and an in–plane resolution of 1.5×1.5 mm^2, with no inter-slice gaps, acquisition matrix of 96×96, field of view of 144×144 mm^2, and bandwidth 1408 Hz/Pixel. The acquisition was triggered from the peripheral pulse trace for reducing artefacts associated with cardiac induced motion [17]. The echo time was 90 ms and the repetition time was 180 ms. Interleaved slice acquisition order was chosen to avoid cross talk between adjacent slices. Two acquisitions with opposite read-out gradient polarity were acquired to correct for EPI induced geometric distortions [18]. The total scan time was approximately 20 minutes, depending on heart rate.

The two datasets obtained in the cervical cord with opposite phase encoding directions were combined into a single dataset with reduced geometric distortions [18]. Spinal volumes in image space were then sinc interpolated from a 96×96 acquisition matrix to a 192×192 image matrix, resulting in an in-plane resolution of 0.75 mm^2. A diffusion tensor model was fitted to the interpolated data on a voxel-by-voxel basis using the open-source Camino software package (www.camino.org) (Cook et al., 2006). Before further processing, all images were checked for artefacts.

Diffusion tensor imaging (DTI) of the brain. To investigate the relationship between microstructural changes along the entire course of the CST (i.e. spinal cord and brain) we also acquired a brain DTI data set using a single shot echo planar imaging sequence as above [15]. Each data set consisted of 61 images with a b-value = 1000 $s*mm^{-2}$ and 7 images with a b-value = 100 $s*mm^{-2}$. Details of this sequence have been reported previously [19] and are therefore reported here only in brief: 2.3 mm isotropic resolution, FoV = 220×220 mm^2, matrix size = 96×96, 60 axial slices, no inter-slice gaps, interleaved slice acquisition order, slice-to-slice repetition time = 160 ms, echo time = 90 ms, flip angle = 90°, readout bandwidth = 2003 Hz/Pixel, two repetitions, with inverted read-out polarity as described for the spinal cord DTI acquisition. The total acquisition time was 19 minutes. On the combined distortion-corrected data set [18], the diffusion tensor model was fit at each voxel using the RESTORE method [20] as implemented in Camino.

Preprocessing for Voxel-based Quantification of DTI Data

Preprocessing steps from the VBM-DTI data set of the brain were described in detail previously [19] and are reported here in brief: i) *Segmentation*: a unified segmentation procedure [21] was used for bias correction and segmentation of the T1w image into GM, WM and cerebrospinal fluid (CSF). For each subject, this resulted in three images in T1w native image space, in which each voxel was assigned a probability of being GM, WM and CSF, respectively. ii) *Coregistration of FA and other DTI maps to WM*: For each subject the FA map was linearly coregistered to the corresponding WM probability map using 12 degrees of freedom and trilinear interpolation. This step exploited the similarity between the information in the WM probability map and the distortion corrected FA map to ensure that subject DTI data was in alignment with the corresponding T1w data. iii) *Creation of a WM mask in DTI space*: The WM probability map was resliced into DTI space using the inverse transformation from the previous step and binarized by thresholding at the same probability value$>$0.15 for consistency with the cervical cord DTI analysis. iv) *Application of WM mask to DTI maps*: The WM mask was applied to the registered FA map to create a subject-specific white-matter masked map of FA. v) *Non-linear registration of T1w image to MNI space*: A diffeomorphic non-linear image registration tool (DARTEL, [22]), was used to estimate the deformation fields required to warp the GM and WM probability maps from each subject T1w native image space into MNI space. vi) *Transformation of FA maps into MNI space*: The DARTEL deformation fields were applied to the corresponding FA maps and the white matter mask and

smoothed by a 10 mm FWHM Gaussian kernel to account for inter-individual anatomical variability. vii) *Tissue specific smoothing compensation*: The smoothed warped FA map was divided by the smoothed warped white matter mask to compensate for the reduction of FA caused by smoothing [23,24].

Image Analysis

We examined i) cross-sectional spinal cord area and FA differences in both spinal and cranial ROIs between SCI patients and controls; ii) the correlation between FA of the whole cervical cord and cervical atrophy; iii) the correlation between spinal FA and clinical outcomes and iv) the correlation between spinal FA and cranial FA changes of the CST.

Cross-sectional Spinal Cord Area Measurement

Previously, we reported the group difference of the *cross-sectional spinal cord area* using a standard semi-automated segmentation method on optimized 3D T1w scans [1,14] in a study cohort including the subset of the current participants (see [19]).

Region of Interests in the Cervical Cord – DTI Data

To assess regional differences in FA, in each participant two ROIs were manually drawn on the average low-b-value image in native space between C1 and C3 covering the left and right CST running in the lateral columns (Fig. 1) similar to those ROIs used in [25]. To obtain the intra-observer coefficient-of-variation (CoV) for the FA of the right and left CST, a second experiment was run by the same observer (PF), who was blind to the results of the first experiment, 1 week later, on five randomly chosen participants. The mean CoV of the left and right CST was below 5%. As the FA of both CST sides in SCI patients and controls did not differ significantly the mean FA was calculated and used in the analysis regarding the associations between cervical FA and cranial *FA*. In addition, a ROI covering the whole spinal cord was determined using an automatic region growing segmentation algorithm [26] applied to the FA map with a lower threshold of FA $\leq$0.15 as the stopping criterion. We then calculated the mean FA value within each ROIs of the spinal cord. Based on the cross-sectional spinal cord area segmentation, whole cord FA measures were corrected for partial volume effects as described in [27].

Regions of Interest (ROI) in the Brain – DTI Data

As we focused our investigations on degenerative axonal changes in the cranial CST we limited our search volume using a binary mask representing the left and right CST from the JHU white-matter tractography atlas [28]. The following bilateral ROIs containing the CST from the ICBM-DTI-81 white-matter labels atlas [29] were extracted and coregistered to the MNI template: pyramids, cerebral peduncle and posterior limb of the internal capsule.

Statistical Analysis of Imaging Data

The spinal cord DTI data set of one patient was affected by motion artefacts and another patient had an incomplete DTI brain data set. Therefore the final analysis comprised nine SCI patients and ten controls for the group comparison of spinal FA and eight SCI patients and ten controls for the interaction between spinal FA and cranial FA.

Cervical Cord DTI Data

We applied a two-sample t-test to investigate differences in FA of the left and right CST ROIs and the whole cervical cord ROI between SCI subjects and controls. Two multiple linear regression models were used to assess relationships between: (i) changes in the microstructure (using FA of the whole cervical cord ROI) and macrostructural changes (e.g. cord area change) and (ii) microstructural changes and clinical impairment (9HPT, ARAT, MVC) over and above any differences that could be attributed to cord area [1]. SPSS (SPSS Inc., Chicago, IL) was used for the multiple linear regression analysis and differences between mean FA of the ROIs between SCI subjects and controls. Results that survived $p<0.05$ are reported.

Brain DTI Data

In a previous study, we reported the main effect of DTI metrics in the cranial CST that included this subset of participants [19]. Here, we present a further analysis, in which we tested whether spinal FA of the CST was associated with cranial FA of the CST. We constructed a General Linear Model (GLM), comprising the FA of the cervical CST as well as group effect and age and total intra-cranial volume confounds. The GLM was fitted to the registered and smoothed subject specific FA values and the resulting parameters were used to calculate a t-statistic at each voxel within the central CST. The t-tests were one-tailed and associated *p*-values were corrected for multiple comparisons within each ROI (Family Wise Error (FWE) $p<0.05$) using Gaussian random field theory [30].

The resulting statistical parametric maps (SPMs) allowed us to test for the main effect of spinal FA on cranial FA of the CST [19] and the interaction between spinal FA and trauma. The interaction was used to identify voxels in the cranial CST where trauma-related changes in FA could be explained by spinal FA, relative to normal variability.

Results

Clinical Data and Cord Area

Nine chronic SCI subjects (mean period post SCI was 14.8 years (SD 7.2, range 7–30) had lesions of the cervical cord (C5–C8) due to a traumatic event (eight fractures and one disc prolapse). All patients experienced bilateral impairment of the upper and lower limbs as assessed by the American Spinal Cord Injury Association Impairment classification (Tabel 1). Specifically, SCI participants had lower grip strength [SCI: mean = 0.13 mV (SD 0.1) vs. Controls: 0.49 mV (SD 0.26), $p = 0.001$] and performed more slowly on the 9HPT with the dominant hand [SCI: mean = 98.28 sec (SD 84.93) vs. Controls: mean = 17.04 sec (SD 1.56), p = 0.007] and non-dominant hand [SCI: mean = 141.22 - sec (SD 121.98) vs. Controls: mean = 18.14 sec (SD 1.35), p = 0.005] when compared to controls (Table 1).

As reported previously, the cross-sectional spinal cord area was decreased by more than 30% [1].

Differences in FA between SCI Subjects and Controls

Compared to controls, SCI subjects showed lower mean FA in right CST ROI [SCI: 0.67 (SD 0.07) vs. Controls: 0.75 (SD 0.04), p = 0.008] (Fig. 2 A), left CST ROI [SCI: 0.63 (SD 0.08) vs. Controls: 0.76 (SD 0.05), $p<0.001$] (Fig. 2B) and in the whole cervical cord ROI [SCI: 0.52 (SD 0.06) vs. Controls: 0.63 (SD 0.04), $p<0.001$] (Fig. 2 C).

Associations between cervical FA and

(i) cervical atrophy. In SCI patients, the FA of the whole cervical cord ROI was positively correlated with cross-sectional spinal cord area (i.e. cord atrophy) (r = 0.80 p = 0.01), independently of age (Fig. 3 A).

(ii) upper limb function. Similarly, FA of the right CST ROI was positively correlated with the right 9HPT score

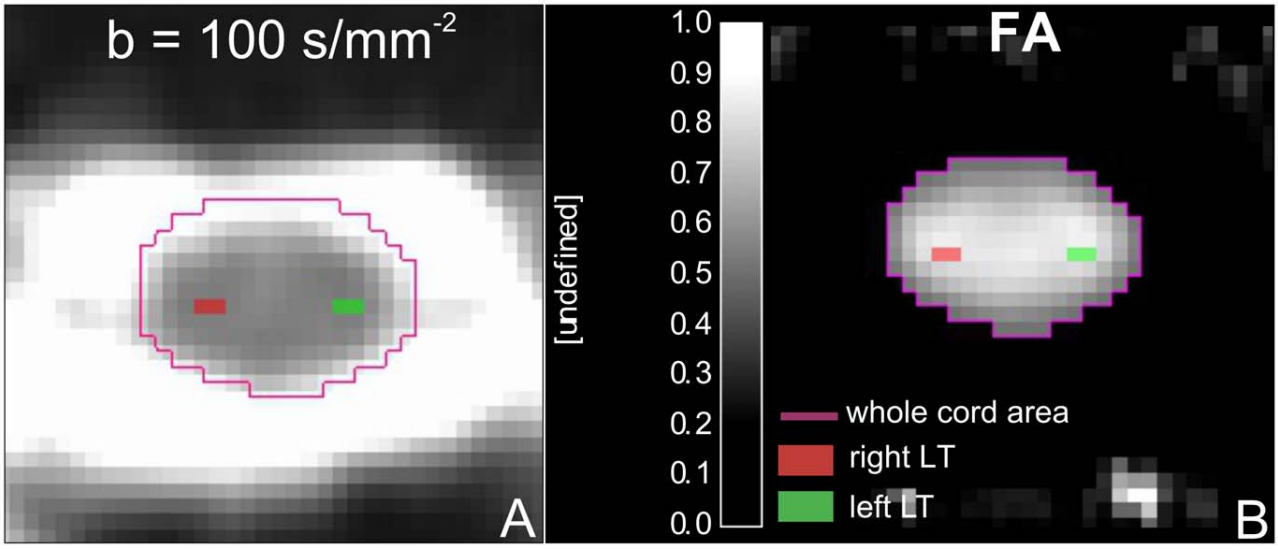

Figure 1. Axial FA image of the cervical cord (C1–C3) showing the locations of the two ROIs superimposed on the anatomoical location of the left and right corticospinal tracts. Note that ROIs were first drawn on the low diffusion weighted images (A) and then overlaid onto the diffusion maps (B).
doi:10.1371/journal.pone.0051729.g001

independently of cross-sectional cord area and age ($r = 0.72$, $p = 0.03$) (Fig. 3 B). In other words, changes in spinal microstructure – reflected by FA – is associated with the degree of manual dexterity impairment independently of spinal cord atrophy and age.

(iii) FA of cranial CST. We first confirmed a decrease in FA at multiple levels of the central CST in SCI subjects compared to controls (see [19]) – comprising the bilateral pyramids and the posterior knee of the internal capsule. Crucially, here we found a significant interaction ($x = 24$, $y = -15$, $z = 6$; $p = 0.001$, FWE corrected) between the main effect of group and spinal FA (Fig. 4). In other words, changes in spinal FA of the CST following trauma were associated with greater changes in the FA of the posterior knee of the internal capsule, relative to changes under normal inter-subject variability.

Discussion

This study establishes relationships between disruption of CST white matter – at a microstructural level, as demonstrated by fractional anisotropy, and spinal cord area – and disability. In addition we observed reductions of FA in the central nervous system, representing remote correlates of degeneration in the chronically injured cervical cord.

Table 1. Individual clinical and behavioural data for the SCI subjects with means.

Subject	Age	Aetiology of the injury	Time since injury (years)	Level of motor impairment/ ASIA	dh 9HPT	ndh 9HPT	MVC	ARAT
1	43	fracture	14	C6/D	68.0	54.35	0.22	36.0
2	29	fracture	9	C6/B	52.6	59.2	0.05	42.0
3	44	fracture	7	C7/C	56.75	118.4	0.25	57.0
4	35	fracture	14	C5/A	190.5	300.0	0.02	26.0
5	61	fracture	19	C6/A	68.3	76.5	0.05	26.5
6	40	disc prolapse	19	C5/C	283	300.0	0.01	26.0
7	53	fracture	7	C8/D	38.55	42.45	0.25	53.0
8	56	fracture	15	C5/D	105.0	300.0	0.11	25.0
9	50	fracture	30	C5/D	21.8	20.1	0.22	57.0
Mean	45.7		14.9		98.3	141.2	0.13	38.72
SD	9.7		6.8		84.94	121.98	0.1	13.13

ASIA = American Spinal Injury Association impairment scale; dh = dominant hand; ndh = non-dominant hand; 9HPT = Nine Hole Peg Test; MVC = maximum voluntary contraction, ARAT = Arm Research Arm Test; SD = standard deviation.
doi:10.1371/journal.pone.0051729.t001

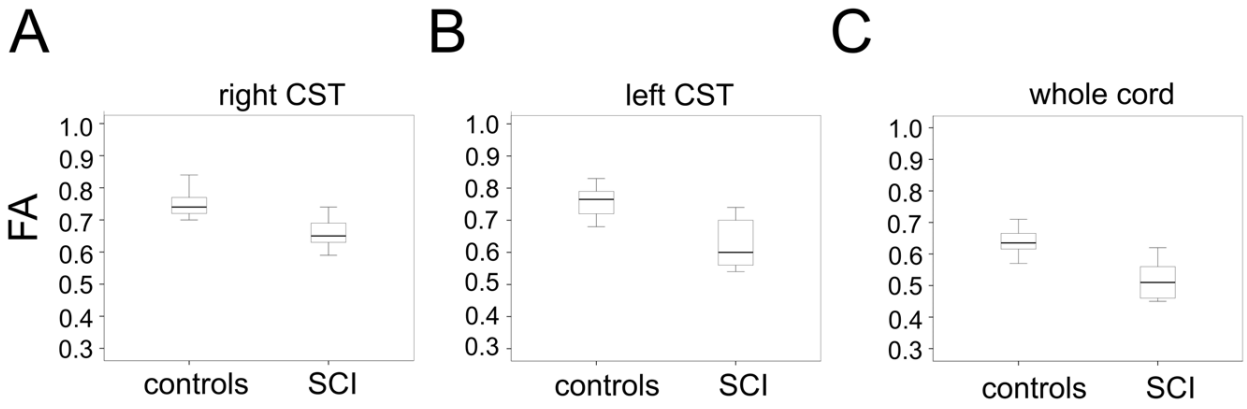

Figure 2. Box plots showing the statistically different mean FA in the region of interest in (A) the right corticospinal tract, (B) left corticospinal tract and (C) whole spinal cord area in controls and SCI patients.
doi:10.1371/journal.pone.0051729.g002

Axonal Degeneration in the Injured Cervical Cord

It is now well established that trauma to the spinal cord results in macrostructural changes leading to spinal and cortical atrophy [1,2,31]. The pathological processes underlying these changes are not fully resolved and may be the result of multiple microstructural changes such as axonal degeneration [7], progressive demyelination [32], loss of large diameter axons [33] death of oligodendrocytes [34] and/or damage to the spinal grey matter [35]. We found lower FA in the CST at cervical segments rostral to the traumatic impact and also a general reduction of FA in the cross-section of the cervical cord including white and grey matter, in agreement with previous reports [3,36]. These alterations of the axonal architecture suggest that multiple processes, such as axonal degeneration and demyelination, might occur at sites several segments rostral to trauma to the cervical cord.

(i) *Association* between Lower FA and Spinal Atrophy

Moving beyond the group differences, our aim was to determine the relationship between micro– and macrostructural effects of a traumatic SCI. Reduced cord area (i.e. spinal atrophy) predicts upper limb impairment following SCI [1,6] and relates to white matter changes of the cranial CST [19]. Here, we add to this finding by reporting a relationship between FA in the cervical cord and cord area at the identical anatomical level. The link between micro- and macrostructure may be helpful in understanding the time course of changes at different structural levels. In particularly, acute changes in FA may precede a decline in cord area [1,6] as the latter results from an accumulation of microstructural as well as macrostructural changes representing the endpoint of neurodegeneration. Future studies may investigate the rate of the underlying changes – that may help understand the underlying pathophysiology.

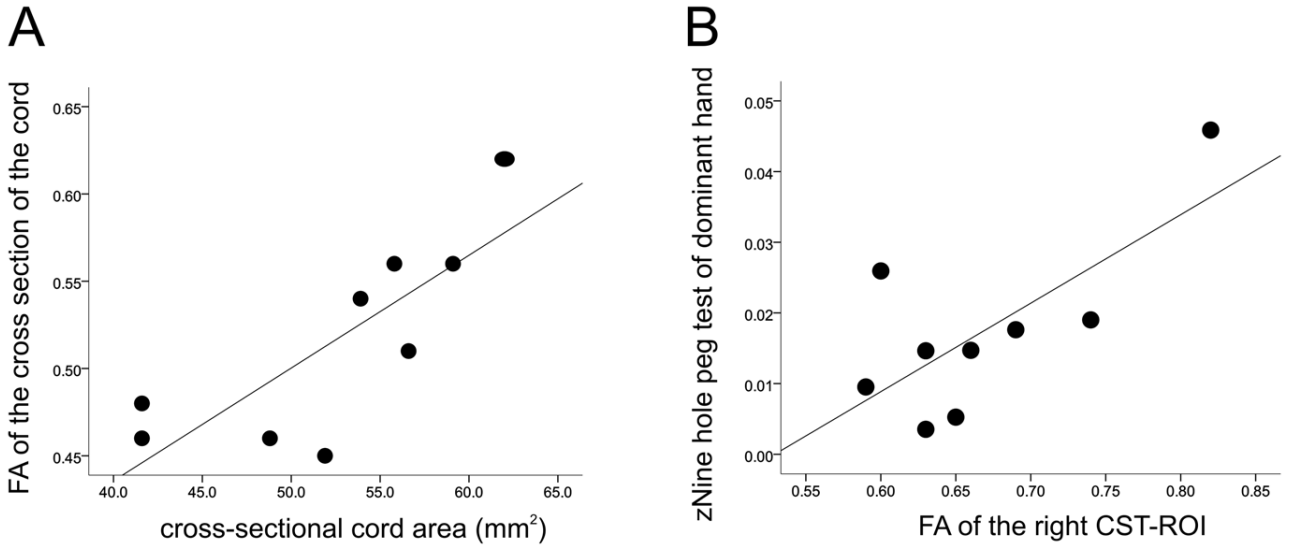

Figure 3. Scatter plots showing the correlations between spinal FA of the corticospinal tract and cord area and clinical measures in SCI subjects. (A) FA of the whole cervical cord ROI vs. cross sectional spinal cord area, (B) Spinal FA of the right CST-ROI vs. dominant 9HPT score. Note that greater values of the 9HPT score represent better outcome.
doi:10.1371/journal.pone.0051729.g003

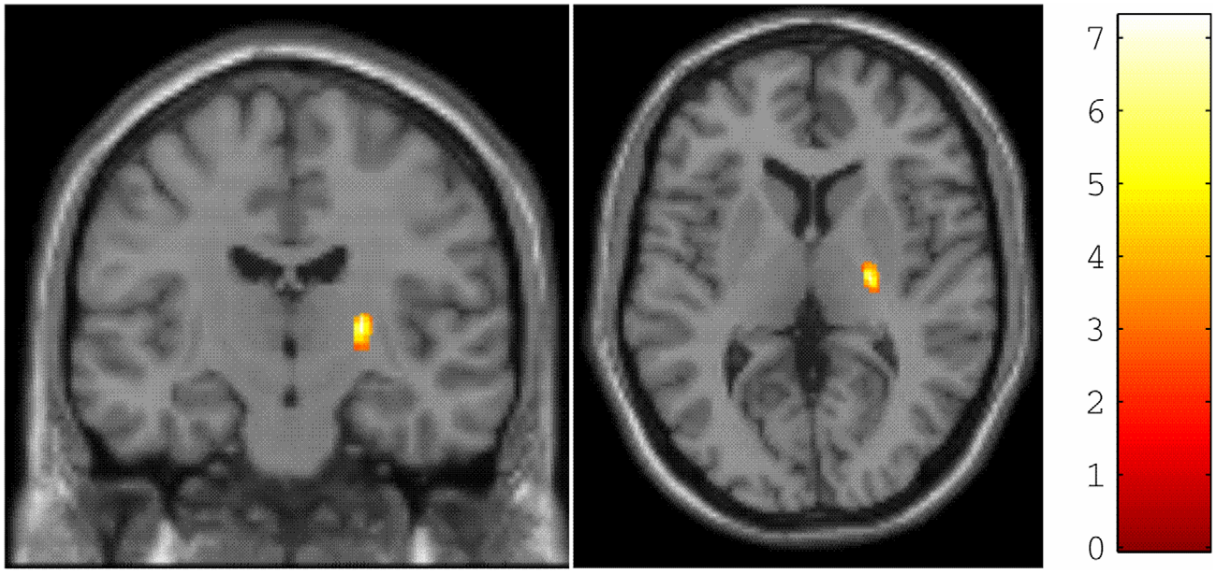

Figure 4. Statistical parametric maps (thresholded at p<0.01, uncorrected for display purposes only) showing the right internal capsule, in which changes in cranial FA of the corticospinal tract (CST) are more sensitive to spinal changes in FA of the mean CST compared with normal variability. The colour bar represents the t-value.
doi:10.1371/journal.pone.0051729.g004

(ii) *Association* between Axonal Degeneration and Upper Limb Function

Recent studies investigating structural spinal changes have demonstrated a close relationship between cervical microstructural changes and the ASIA motor scale [3,37]. The ASIA score quantifies gross motor and sensory changes – while it is anticipated that treatment strategies will induce only minimal functional changes [38]. Therefore, we assessed fine finger movement and showed that lower mean FA measured in ROIs that correspond to the left and right lateral CST predicts impaired manual dexterity – as assessed by the performance during the 9HPT – independently of cord atrophy [1]. This means that a reduced FA, reflecting microstructural tissue changes within ROIs of the CST, may be a complementary predictor of fine motor recovery, in addition to cross-sectional spinal cord area measurement.

(iii) *Association* between Changes in Microstructure of the CST at Spinal and Cranial Level

Previously, we found – in the same patient cohort – a significant relationship between macrostructural spinal changes (i.e. atrophy) and microstructural changes of the cranial CST [19]. Here, we provide a further mechanistic insight by demonstrating a relationship between axonal degeneration in the CST, a tract indispensable for voluntary control of manual dexterity [39], immediately rostral to the initial site of trauma and changes upstream in the CST at the level of the internal capsule. Based on animal literature [39], trauma induces retrograde axonal degeneration that, over time, leads to quantifiable changes in white matter tissue at multiple levels of the CST. Moreover, the association between reduced micro- and macrostructural integrity in the spinal cord and brain [19] supports our recent finding, in the same patient cohort, of changes of the electrophysiological properties of the CST reflected by increased motor threshold and prolonged cortical silent periods [5]. In other words, trauma induced retrograde axonal degeneration of the CST – as detected by DTI – may be a direct correlate of impaired corticospinal excitability, as reflected by increased motor thresholds [5,37].

Finally, it should be noted that measures of neural changes of the spinal cord and brain at the microstructural level can be influenced, in addition to trauma, by different degrees of activity, such as suppression (i.e. immobilization) or enhancement (i.e. training) throughout the patients clinical history. For example, in patients with immobilization of the hand (in writer's cramp) or upper limb (in cast treatment due to fracture) a relative decrease in grey matter occurred in the contralateral M1 along with a decrease in corticomotor excitability [40]. Subsequent training reversed the effects of immobilization, and resulted in a re-establishment in regional grey matter density and excitability of M1. Similar activity-dependent effects over time could have influenced, structural changes in these chronic SCI patients. Future studies will assess the influence of intensity (time spent in training, frequency, duration, repetitions, etc.) and nature of rehabilitation interventions (active versus passive movements, task orientation etc) as well as the overall levels of activity (post-traumatic immobilization versus mobilization into wheelchair or locomotion).

In conclusion, we have demonstrated that trauma induces a reduction in structural integrity in the CST throughout the cervical cord and brain. Crucially, the amount of degeneration is associated with clinical status in chronic SCI, independently of spinal atrophy. Thus, our clinically viable MRI protocol allows the assessment of long-distance fibre degeneration. Future longitudinal studies, in larger cohorts of SCI subjects, are necessary to investigate whether DTI metrics can serve as sensitive biomarkers but the results of this study – involving only a small group – provide promising initial results.

Acknowledgments

We thank all participants who generously spared their time for this study and the radiographers of the Wellcome Trust Centre for Neuroimaging for technical support. We are indebted to our three reviewers for guidance in

clarifying and elaborating this manuscript. Open access for this publication was kindly funded by the Wellcome Trust.

Author Contributions

Conceived and designed the experiments: TS ZN CH NW KF CK AT. Performed the experiments: PF TS ZN CH. Analyzed the data: PF TS ZN CH. Wrote the paper: PF TS ZN CH NW KF AT.

References

1. Freund P, Weiskopf N, Ward NS, Hutton C, Gall A, et al. (2011) Disability, atrophy and cortical reorganization following spinal cord injury. Brain 134: 1610–1622.
2. Wrigley PJ, Gustin SM, Macey PM, Nash PG, Gandevia SC, et al. (2009) Anatomical changes in human motor cortex and motor pathways following complete thoracic spinal cord injury. Cereb Cortex 19: 224–232.
3. Cohen-Adad J, El Mendili MM, Lehericy S, Pradat PF, Blancho S, et al. (2011) Demyelination and degeneration in the injured human spinal cord detected with diffusion and magnetization transfer MRI. Neuroimage 55: 1024–1033.
4. Dietz V, Curt A (2006) Neurological aspects of spinal-cord repair: promises and challenges. Lancet Neurol 5: 688–694.
5. Freund P, Wheeler-Kingshott CA, Nagy Z, Gorgoraptis N, Weiskopf N, et al. (2012) Axonal integrity predicts cortical reorganisation following cervical injury. J Neurol Neurosurg Psychiatry 83: 629–637.
6. Lundell H, Barthelemy D, Skimminge A, Dyrby TB, Biering-Sorensen F, et al. (2011) Independent spinal cord atrophy measures correlate to motor and sensory deficits in individuals with spinal cord injury. Spinal Cord 49: 70–75.
7. Pierpaoli C, Barnett A, Pajevic S, Chen R, Penix LR, et al. (2001) Water diffusion changes in Wallerian degeneration and their dependence on white matter architecture. Neuroimage 13: 1174–1185.
8. Basser PJ, Pierpaoli C (1996) Microstructural and physiological features of tissues elucidated by quantitative-diffusion-tensor MRI. J Magn Reson B 111: 209–219.
9. Gouw AA, Seewann A, Vrenken H, van der Flier WM, Rozemuller JM, et al. (2008) Heterogeneity of white matter hyperintensities in Alzheimer's disease: post-mortem quantitative MRI and neuropathology. Brain 131: 3286–3298.
10. Schmierer K, Wheeler-Kingshott CA, Boulby PA, Scaravilli F, Altmann DR, et al. (2007) Diffusion tensor imaging of post mortem multiple sclerosis brain. Neuroimage 35: 467–477.
11. Freund P, Rothwell J, Craggs M, Thompson AJ, Bestmann S (2011) Corticomotor representation to a human forearm muscle changes following cervical spinal cord injury. Eur J Neurosci 34: 1839–1846.
12. Goodkin DE, Hertsgaard D, Seminary J (1988) Upper extremity function in multiple sclerosis: improving assessment sensitivity with box-and-block and nine-hole peg tests. Arch Phys Med Rehabil 69: 850–854.
13. Hoogervorst EL, Kalkers NF, Uitdehaag BM, Polman CH (2002) A study validating changes in the multiple sclerosis functional composite. Arch Neurol 59: 113–116.
14. Freund PA, Dalton C, Wheeler-Kingshott CA, Glensman J, Bradbury D, et al. (2010) Method for simultaneous voxel-based morphometry of the brain and cervical spinal cord area measurements using 3D-MDEFT. J Magn Reson Imaging 32: 1242–1247.
15. Reese TG, Heid O, Weisskoff RM, Wedeen VJ (2003) Reduction of eddy-current-induced distortion in diffusion MRI using a twice-refocused spin echo. Magn Reson Med 49: 177–182.
16. Cook PA, Symms M, Boulby PA, Alexander DC (2007) Optimal acquisition orders of diffusion-weighted MRI measurements. J Magn Reson Imaging 25: 1051–1058.
17. Wheeler-Kingshott CA, Hickman SJ, Parker GJ, Ciccarelli O, Symms MR, et al. (2002) Investigating cervical spinal cord structure using axial diffusion tensor imaging. Neuroimage 16: 93–102.
18. Andersson JL, Skare S, Ashburner J (2003) How to correct susceptibility distortions in spin-echo echo-planar images: application to diffusion tensor imaging. Neuroimage 20: 870–888.
19. Freund P, Wheeler-Kingshott CA, Nagy Z, Gorgoraptis N, Weiskopf N, et al. (2012) Axonal integrity predicts cortical reorganisation following cervical injury. J Neurol Neurosurg Psychiatry doi:10.1136/jnnp-2011-301875.
20. Chang LC, Jones DK, Pierpaoli C (2005) RESTORE: robust estimation of tensors by outlier rejection. Magn Reson Med 53: 1088–1095.
21. Ashburner J, Friston KJ (2005) Unified segmentation. Neuroimage 26: 839–851.
22. Ashburner J (2007) A fast diffeomorphic image registration algorithm. Neuroimage 38: 95–113.
23. Lee JE, Chung MK, Lazar M, DuBray MB, Kim J, et al. (2009) A study of diffusion tensor imaging by tissue-specific, smoothing-compensated voxel-based analysis. Neuroimage 44: 870–883.
24. Draganski B, Ashburner J, Hutton C, Kherif F, Frackowiak RS, et al. (2011) Regional specificity of MRI contrast parameter changes in normal ageing revealed by voxel-based quantification (VBQ). Neuroimage Volume 55, 1423–1434.
25. Freund P, Wheeler-Kingshott C, Jackson J, Miller D, Thompson A, et al. (2010) Recovery after spinal cord relapse in multiple sclerosis is predicted by radial diffusivity. Mult Scler 16: 1193–1202.
26. Adams R, Bischof L (1994) Seeded region growing EEE Transactions on 16(6): 641–647.
27. Schneider T, Thomas DL, Kachramanoglou C, Ciccarelli O, Alexander DC, et al. (2011) Fuzzy partial volume correction of spinal cord DTI parameters. International Society for Magnetic Resonance in Medicine 19th Annual Scientific Meeting and Exhibition: 2011 Proceedings. (pp.4556–4556).
28. Wakana S, Caprihan A, Panzenboeck MM, Fallon JH, Perry M, et al. (2007) Reproducibility of quantitative tractography methods applied to cerebral white matter. Neuroimage 36: 630–644.
29. Mori S, Oishi K, Jiang H, Jiang L, Li X, et al. (2008) Stereotaxic white matter atlas based on diffusion tensor imaging in an ICBM template. Neuroimage 40: 570–582.
30. Friston KJ, Holmes AP, Worsley KJ, Poline JB, Frith CD, et al. (1995) Statistical parametric maps in functional imaging: A general linear approach. Hum Brain Mapp 2: 189–210.
31. Jurkiewicz MT, Crawley AP, Verrier MC, Fehlings MG, Mikulis DJ (2006) Somatosensory cortical atrophy after spinal cord injury: a voxel-based morphometry study. Neurology 66: 762–764.
32. Buss A, Pech K, Merkler D, Kakulas BA, Martin D, et al. (2005) Sequential loss of myelin proteins during Wallerian degeneration in the human spinal cord. Brain 128: 356–364.
33. Blight AR, DeCrescito V (1986) Morphometric analysis of experimental spinal cord injury in the cat: the relation of injury intensity to survival of myelinated axons. Neuroscience 19: 321–341.
34. Blight AR (1985) Delayed demyelination and macrophage invasion: a candidate for secondary cell damage in spinal cord injury. Cent Nerv Syst Trauma 2: 299–315.
35. Kakulas BA (1984) Pathology of spinal injuries. Cent Nerv Syst Trauma 1: 117–129.
36. Ellingson BM, Ulmer JL, Kurpad SN, Schmit BD (2008) Diffusion tensor MR imaging in chronic spinal cord injury. AJNR Am J Neuroradiol 29: 1976–1982.
37. Petersen JA, Wilm BJ, von MJ, Schubert M, Seifert B, et al. (2011) Chronic cervical spinal cord injury: DTMRI correlates with clinical and electrophysiological measures. J Neurotrauma doi:10.1089/neu.2011.2027.
38. Ellaway PH, Kuppuswamy A, Balasubramaniam AV, Maksimovic R, Gall A, et al. (2010) Development of quantitative and sensitive assessments of physiological and functional outcome during recovery from spinal cord injury: A Clinical Initiative. Brain Res Bull 2011 Mar 10;84(4–5): 343–57.
39. Lemon RN (2008) Descending pathways in motor control. Annu Rev Neurosci 31: 195–218.
40. Granert O, Peller M, Gaser C, Groppa S, Hallett M, et al. (2011) Manual activity shapes structure and function in contralateral human motor hand area. Neuroimage 54: 32–41.

Publications

Some ideas and figures have appeared previously in the following publications:

Journal papers

- Freund, P., Schneider, T., Nagy, Z., Hutton, C., Weiskopf, N., Friston, K., Wheeler-Kingshott, C. A. M. Thompson, A. (in press). Degeneration of the injured cervical cord is associated with remote changes in corticospinal tract integrity and upper limb impairment. *PLoS One*.

- Panagiotaki, E., Schneider, T., Siow, B., Hall, M. G., Lythgoe, M. F., & Alexander, D. C. (2012). Compartment models of the diffusion MR signal in brain white matter: a taxonomy and comparison. *NeuroImage, 59(3), 2241-2254*.

- Wheeler-Kingshott, C. A. M., Ciccarelli, O., Schneider, T., Alexander, D. C., & Cercignani, M. (2012). A new approach to structural integrity assessment based on axial and radial diffusivities. *Functional Neurology, 27(2), 85-90*.

- Zhang, H., Schneider, T., Wheeler-Kingshott, C. A., & Alexander, D. C. (2012). NODDI: Practical in vivo neurite orientation dispersion and density imaging of the human brain. *NeuroImage, 61(4), 1000-1016*.

Journal papers in preparation

- Ciccarelli, O., Thomas, D. L., De Vita, E., Wheeler-Kingshott, C. A. M., Schneider, T., Kachramanoglou, C., Toosy, A. T., & Thompson, A. J. Spinal cord spectroscopy, tractography and q-space MRI in a case of NMO spectrum disorder.

Conference papers

- Schneider, T., Wheeler-Kingshott, C. A. M., & Alexander, D. C. (2010). In-vivo estimates of axonal characteristics using optimized diffusion MRI protocols for single fibre orientation. *13th International Conference on Medical Image Computing and Computer-Assisted Intervention (MICCAI2010)*

Conference abstracts

- Schneider, T., Wheeler-Kingshott, C. A. M., & Alexander, D. C. (2012). Mapping the axon diameter index in the corpus callosum is clinically feasible. *In Proc. Intl. Soc. Mag. Reson. Med Vol. 20*. Melbourne, Australia.
  (selected for oral presentation)

- Schneider, T., Ciccarelli, O., Kachramanoglou, C., Thomas, D. L., & Wheeler-Kingshott, C. A. M. (2011). Reliability of tract-specific q-space imaging metrics in healthy spinal cord. In Proc. *Intl. Soc. Mag. Reson. Med Vol. 19 (pp. 680)*. Montreal, Canada.
  (selected for oral presentation)

- Schneider, T., Thomas, D. L., Kachramanoglou, C., Ciccarelli, O., Alexander, D. C., & Wheeler-Kingshott, C. (2011). Fuzzy partial volume correction of spinal cord DTI parameters. *In Proc. Intl. Soc. Mag. Reson. Med Vol. 19 (pp. 4556)*. Montreal, Canada.

- Schneider, T., Nagy, Z., Wheeler-Kingshott, C. A. M., Thomson, A. J., & Freund, P. (2011). Diffusion tensor imaging detects axonal degeneration and its extent is associated with disability in chronic spinal cord injury. *In Proc. Intl. Soc. Mag. Reson. Med Vol. 19 (pp. 2353)*. Montreal, Canada.

- Schneider, T., Alexander, D. C., & Wheeler-Kingshott, C. A. M. (2010). Optimized diffusion MRI protocols for estimating axon diameter with known fibre orientation. *In Proc. Intl. Soc. Mag. Reson. Med Vol. 18 (pp. 1561)*. Stockholm, Sweden.

- Schneider, T., Alexander, D. C., & Wheeler-Kingshott, C. A. M. (2009). Preliminary investigation of position dependency of radial diffusivity in the cervical spinal cord. *In Proc. Intl. Soc. Mag. Reson. Med Vol. 17 (pp. 3191)*. Honolulu, Hawaii.

Bibliography

[1] F. Aboitiz et al. "Individual differences in brain asymmetries and fiber composition in the human corpus callosum." In: *Brain Research* 598.1-2 (1992), pp. 154–161.

[2] A. L. Alexander et al. "Analysis of partial volume effects in diffusion-tensor MRI." In: *Magnetic Resonance in Medicine* 45.5 (2001), pp. 770–780.

[3] D. C. Alexander. "A general framework for experiment design in diffusion MRI and its application in measuring direct tissue-microstructure features." In: *Magnetic Resonance in Medicine* 60.2 (2008), pp. 439–448.

[4] D. C. Alexander et al. "Orientationally invariant indices of axon diameter and density from diffusion MRI." In: *NeuroImage* (2010).

[5] J. L. Andersson, S. Skare, and J. Ashburner. "How to correct susceptibility distortions in spin-echo echo-planar images: application to diffusion tensor imaging." In: *NeuroImage* 20.2 (2003), pp. 870–888.

[6] Y. Assaf and P. J. Basser. "Composite hindered and restricted model of diffusion (CHARMED) MR imaging of the human brain." In: *NeuroImage* 27.1 (2005), pp. 48–58.

[7] Y. Assaf and Y. Cohen. "Assignment of the water slow-diffusing component in the central nervous system using q-space diffusion MRS: Implications for fiber tract imaging." In: *Magnetic Resonance in Medicine* 43.2 (2000), pp. 191–199.

[8] Y. Assaf, A. Mayk, and Y. Cohen. "Displacement imaging of spinal cord using q-space diffusion-weighted MRI." In: *Magnetic Resonance in Medicine* 44.5 (2000), pp. 713–722.

[9] Y. Assaf et al. "AxCaliber: a method for measuring axon diameter distribution from diffusion MRI." In: *Magnetic Resonance in Medicine* 59.6 (2008), pp. 1347–1354.

[10] Y. Assaf et al. "High b-value q-space analyzed diffusion-weighted MRI: Application to multiple sclerosis." In: *Magnetic Resonance in Medicine* 47.1 (2002), pp. 115–126.

[11] A. V. Avram et al. "In vivo detection of microscopic anisotropy using quadruple pulsed-field gradient (qPFG) diffusion MRI on a clinical scanner." In: *NeuroImage* (2012).

[12] L. Avram, Y. Assaf, and Y. Cohen. "The effect of rotational angle and experimental parameters on the diffraction patterns and micro-structural information obtained from q-space diffusion NMR: implication for diffusion in white matter fibers." In: *Journal of Magnetic Resonance* 169.1 (2004), pp. 30–38.

[13] L. Avram et al. "Three-dimensional water diffusion in impermeable cylindrical tubes: theory versus experiments." In: *NMR Biomed.* 21.8 (2008), pp. 888–898.

[14] J. Balentine, G. WB, and B. M. "Pathology of experimental spinal cord trauma. I. The necrotic lesion as a function of vascular injury." In: *Laboratory investigation; A journal of technical methods and pathology* 39.3 (1978), p. 236.

[15] B. Balinov et al. "The NMR Self-Diffusion Method Applied to Restricted Diffusion. Simulation of Echo Attenuation from Molecules in Spheres and between Planes." In: *Journal of Magnetic Resonance, Series A* 104.1 (1993), pp. 17–25.

[16] D. Barazany, P. J. Basser, and Y. Assaf. "In vivo measurement of axon diameter distribution in the corpus callosum of rat brain." In: *Brain* (2009).

[17] A. Bar-Shir et al. "The effect of the diffusion time and pulse gradient duration ratio on the diffraction pattern and the structural information estimated from q-space diffusion MR: Experiments and simulations." In: *Journal of Magnetic Resonance* 194.2 (2008), pp. 230–236.

[18] P. J. Basser, J. Mattiello, and D. L. Le Bihan. "MR diffusion tensor spectroscopy and imaging." In: *Biophysical Journal* 66.1 (1994), pp. 259–267.

[19] P. J. Basser and C. Pierpaoli. "Microstructural and physiological features of tissues elucidated by quantitative-diffusion-tensor MRI." In: *Journal of Magnetic Resonance* 111.3 (1996), pp. 209–219.

[20] C. Beaulieu. "The basis of anisotropic water diffusion in the nervous system - a technical review." In: *NMR in Biomedicine* 15.7-8 (2002), pp. 435–455.

[21] M. Bernstein, K. King, and X. Zhou. *Handbook of MRI pulse sequences*. Academic Press, 2004.

[22] I. E. Biton et al. "Improved detectability of experimental allergic encephalomyelitis in excised swine spinal cords by high b-value q-space DWI." In: *Experimental Neurology* 195.2 (2005), pp. 437–446.

[23] A. R. Blight and V. Descresito. "Morphometric analysis of experimental spinal cord injury in the cat: The relation of injury intensity to survival of myelinated axons." In: *Neuroscience* 19.1 (1986), pp. 321–341.

[24] R. Brown. "On the existence of active molecules in organic and inorganic bodies." In: *Philosophical Magazine* 4 (1828), 162–173.

[25] M. D. Budde et al. "Axonal injury detected by in vivo diffusion tensor imaging correlates with neurological disability in a mouse model of multiple sclerosis." In: *NMR in Biomedicine* 21.6 (2008), pp. 589–97.

[26] R. P. Bunge et al. "Observations on the pathology of human spinal cord injury. A review and classification of 22 new cases with details from a case of chronic cord compression with extensive focal demyelination." In: *Advances in neurology* 59 (1993), p. 75.

[27] S. R. y Cajal. *Degeneration & regeneration of the nervous system*. Vol. 1. Oxford University Press, Humphrey Milford, 1928.

[28] P. T. Callaghan. "NMR imaging, NMR diffraction and applications of pulsed gradient spin echoes in porous media." In: *Magnetic Resonance Imaging* 14.7-8 (1996), pp. 701–709.

[29] P. Callaghan. *Principles of Nuclear Magnetic Resonance Microscopy*. Clarendon Press, 1991.

[30] M. Carpenter and M. Carpen. *Core text of Neuroanatomy*. Williams & Wilkins Baltimore, 1991.

[31] M. Chou et al. "FLAIR Diffusion-Tensor MR Tractography: Comparison of Fiber Tracking with Conventional Imaging." In: *American Journal of Neuroradiology* 26.3 (2005), pp. 591–597.

[32] C. A. Clark, M. Hedehus, and M. E. Moseley. "In vivo mapping of the fast and slow diffusion tensors in human brain." In: *Magnetic Resonance in Medicine* 47.4 (2002), pp. 623–628.

[33] Y. Cohen and Y. Assaf. "High b-value q-space analyzed diffusion-weighted MRS and MRI in neuronal tissues – a technical review." In: *NMR in Biomedicine* (2002).

[34] J. Cohen-Adad et al. "Demyelination and degeneration in the injured human spinal cord detected with diffusion and magnetization transfer MRI." In: *NeuroImage* 55.3 (2011), pp. 1024–33.

[35] D. C. Colvin et al. "New Insights into Tumor Microstructure Using Temporal Diffusion Spectroscopy." In: *Cancer Research* 68.14 (2008), pp. 5941–5947.

[36] P. A. Cook et al. "Optimal acquisition orders of diffusion-weighted MRI measurements." In: *Journal of Magnetic Resonance Imaging* 25.5 (2007), pp. 1051–1058.

[37] P. Cook et al. "Camino: open-source diffusion-MRI reconstruction and processing." In: *Proceedings 14th Scientific Meeting, International Society for Magnetic Resonance in Medicine*. 2006, p. 2759.

[38] D. G. Cory and A. Garroway. "Measurement of translational displacement probabilities by NMR: An indicator of compartmentation." In: *Magnetic Resonance in Medicine* 14.3 (1990), pp. 435–444.

[39] M. J. Crowe et al. "Apoptosis and delayed degeneration after spinal cord injury in rats and monkeys." In: *Nature medicine* 3.1 (1997), pp. 73–76.

[40] A. A. Deo et al. "In vivo serial diffusion tensor imaging of experimental spinal cord injury." In: *Journal of Neuroscience* (2006).

[41] M. D. Does, E. C. Parsons, and J. C. Gore. "Oscillating gradient measurements of water diffusion in normal and globally ischemic rat brain." en. In: *Magnetic Resonance in Medicine* 49.2 (2003), pp. 206–215.

[42] N. G. Dowell et al. "Contiguous-slice zonally oblique multislice (CO-ZOOM) diffusion tensor imaging: examples of in vivo spinal cord and optic nerve applications." In: *Journal of Magnetic Resonance Imaging* 29.2 (2009), pp. 454–460.

[43] I. Drobnjak, B. Siow, and D. C. Alexander. "Optimizing gradient waveforms for microstructure sensitivity in diffusion-weighted MR." In: *Journal of Magnetic Resonance* 206.1 (2010), pp. 41–51.

[44] T. B. Dyrby et al. "Dependence of Axon Diameter Index on Maximum Gradient Strength." In: *Magnetic Resonance in Medicine* (in press).

[45] T. B. Dyrby et al. "An ex vivo imaging pipeline for producing high-quality and high-resolution diffusion-weighted imaging datasets." In: *Human brain mapping* 32.4 (2010), pp. 544–563.

[46] B. M. Ellingson, J. L. Ulmer, and B. D. Schmit. "Optimal diffusion tensor indices for imaging the human spinal cord." In: *Biomedical Sciences Instrumentation* 43 (2007), pp. 128–133.

[47] B. M. Ellingson et al. "Diffusion tensor MR imaging in chronic spinal cord injury." In: *American Journal of Neuroradiology* 29.10 (2008), pp. 1976–1982.

[48] B. M. Ellingson, J. L. Ulmer, and B. D. Schmit. "Morphology and morphometry of human chronic spinal cord injury using diffusion tensor imaging and fuzzy logic." In: *Annals of Biomedical Engineering* 36.2 (2008), pp. 224–36.

[49] J. Farrell et al. "Q-space and conventional diffusion imaging of axon and myelin damage in the rat spinal cord after axotomy." In: *Magnetic Resonance in Medicine* 63.5 (2010), pp. 1323–1335.

[50] J. A. D. Farrell et al. "High b-value q-space diffusion-weighted MRI of the human cervical spinal cord in vivo: Feasibility and application to multiple sclerosis." In: *Magnetic Resonance in Medicine* 59.5 (2008), pp. 1079–1089.

[51] F. Fasano et al. "A highly sensitive radial diffusion measurement method for white matter tract investigation." In: *Magnetic Resonance Imaging* 27.4 (2009), pp. 519–530.

[52] D. Feinberg et al. "Inner volume MR imaging: technical concepts and their application." In: *Radiology* 156.3 (1985), pp. 743–747.

[53] S. Feng et al. "Monitoring of acute axonal injury in the swine spinal cord with EAE by diffusion tensor imaging." In: *Journal of Magnetic Resonance Imaging* 30.2 (2009), pp. 277–85.

[54] U. Ferizi et al. "White Matter Models of in Vivo Diffusion MRI Human Brain Data: A Statistical Ranking." In: *16th Conference on Medical Image Understanding and Analysis*. 2012.

[55] A. Fick. "Über Diffusion. Poggendorff's Annalen der Physik und Chemie, 94 (1855) 59–86." In: *Abstracted by the author as: On Liquid Diffusion. The London, Edinburgh, and Dublin Philosophical Magazine and Journal of Science* 10 (1855), 30–39.

[56] J. C. Ford et al. "MRI characterization of diffusion coefficients in a rat spinal cord injury model." In: *Magnetic resonance in medicine* 31.5 (2005), pp. 488–494.

[57] P. Freund et al. "Disability, atrophy and cortical reorganization following spinal cord injury." In: *Brain* 134.Pt 6 (2011), pp. 1610–1622.

[58] P. Freund et al. "Method for simultaneous voxel-based morphometry of the brain and cervical spinal cord area measurements using 3D-MDEFT." In: *Journal of Magnetic Resonance Imaging* 32.5 (2010), pp. 1242–1247.

[59] F. N. Golabchi et al. "Pixel-based comparison of spinal cord MR diffusion anisotropy with axon packing parameters." In: *Magnetic Resonance in Medicine* 63.6 (2010), pp. 1510–1519.

[60] B. S. Goodman et al. "MRI images at a 45-degree angle through the cervical neural foramina: a technique for improved visualization." In: *Pain Physician* 9.4 (2006), pp. 327–332.

[61] D. Graf von Keyserlingk and U. Schramm. "Diameter of axons and thickness of myelin sheaths of the pyramidal tract fibres in the adult human medullary pyramid." In: *Anatomischer Anzeiger* 157.2 (1984), pp. 97–111.

[62] M. Hall and D. Alexander. "Convergence and Parameter Choice for Monte-Carlo Simulations of Diffusion MRI." In: *IEEE Transactions on Medical Imaging* 28.9 (2009), pp. 1354–1364.

[63] K. D. Harkins et al. "Assessment of the effects of cellular tissue properties on ADC measurements by numerical simulation of water diffusion." In: *Magnetic Resonance in Medicine* 62.6 (2009), pp. 1414–1422.

[64] B. Harrison and W. McDonald. "Remyelination after transient experimental compression of the spinal cord." In: *Annals of neurology* 1.6 (2004), pp. 542–551.

[65] T. Hartkens et al. "VTK CISG Registration Toolkit." In: *BVM 2002* (2002), p. 409.

[66] L. Heimer. *The human brain and spinal cord: Functional neuroanatomy and dissection guide* . Springer-Verlag, 1995.

[67] S. M. Hesseltine et al. "Diffusion tensor imaging in Multiple Sclerosis: assessment of regional differences in the axial plane within normal-appearing cervical spinal cord." In: *American Journal of Neuroradiology* 27.6 (2006), pp. 1189–1193.

[68] M. A. Horsfield et al. "Rapid semi-automatic segmentation of the spinal cord from magnetic resonance images: application in Multiple Sclerosis." In: *NeuroImage* 50.2 (2010), pp. 446–455.

[69] P. J. Huber. *Robust Statistical Procedures*. SIAM, 1996.

[70] J. H. Jensen and J. A. Helpern. "MRI quantification of non-gaussian water diffusion by kurtosis analysis." In: *NMR in Biomedicine* 23.7 (2010), pp. 698–710.

[71] D. K. Jones. "The effect of gradient sampling schemes on measures derived from diffusion tensor MRI: a Monte Carlo study." In: *Magnetic Resonance in Medicine* 51.4 (2004), pp. 807–815.

[72] D. K. Jones and P. J. Basser. ""Squashing peanuts and smashing pumpkins": how noise distorts diffusion-weighted MR data." In: *Magnetic Resonance in Medicine* 52.5 (2004), pp. 979–993.

[73] C. Kachramanoglou et al. "Metabolic changes in the spinal cord after brachial plexus root re-implantation." In: *Neurorehabilitation and Neural Repair* (2012).

[74] K. Kalil and G. E. Schneider. "Retrograde cortical and axonal changes following lesions of the pyramidal tract." In: *Brain research* 89.1 (1975), pp. 15–27.

[75] J. Kärger and W. Heink. "The propagator representation of molecular transport in microporous crystallites." In: *Journal of Magnetic Resonance (1969)* 51.1 (1983), pp. 1–7.

[76] J. F. Kenney and E. S. Keeping. *Mathematics of Statistics*. Van Nostrand, 1957.

[77] D. von Keyserlingk and U. Schramm. "Diameter of axons and thickness of myelin sheaths of the pyramidal tract fibres in the adult human medullary pyramid." In: *Anatomischer Anzeiger* 157.2 (1984), pp. 97–111.

[78] J. H. Kim et al. "Diffusion tensor imaging at three hours after traumatic spinal cord injury predicts long-term locomotor recovery." In: *Journal of Neurotrauma* (2009).

[79] J. H. Kim et al. "Detecting axon damage in spinal cord from a mouse model of Multiple Sclerosis." In: *Neurobiology of Disease* 21.3 (2006), pp. 626–32.

[80] M. D. King et al. "Q-space imaging of the brain." In: *Magnetic Resonance in Medicine* 32.6 (1994), pp. 707–713.

[81] Y. Kinoshita et al. "Apparent diffusion coefficient on rat brain and nerves intoxicated with methylmercury." In: *Environmental research* 80.4 (1999), pp. 348–354.

[82] V. G. Kiselev and K. A. Il'yasov. "Is the "biexponential diffusion" biexponential?" In: *Magnetic Resonance in Medicine* 57.3 (2007), pp. 464–469.

[83] M. A. Koch and J. Finsterbusch. "Compartment size estimation with double wave vector diffusion-weighted imaging." en. In: *Magnetic Resonance in Medicine* 60.1 (2008), pp. 90–101.

[84] M. Komlosh et al. "Observation of microscopic diffusion anisotropy in the spinal cord using double-pulsed gradient spin echo MRI." en. In: *Magnetic Resonance in Medicine* 59.4 (2008), pp. 803–809.

[85] P. W. Kuchel, A. Coy, and P. Stilbs. "NMR "diffusion-diffraction" of water revealing alignment of erythrocytes in a magnetic field and their dimensions and membrane transport characteristics." In: *Magnetic Resonance in Medicine* 37.5 (1997), pp. 637–643.

[86] A. S. LaMantia and P. Rakic. "Axon overproduction and elimination in the corpus callosum of the developing rhesus monkey." In: *The Journal of Neuroscience* 10.7 (1990), pp. 2156–2175.

[87] A. S. LaMantia and P. Rakic. "Cytological and quantitative characteristics of four cerebral commissures in the rhesus monkey." In: *Journal of Comparative Neurology* 291.4 (1990), pp. 520–537.

[88] J. R. Landis and G. G. Koch. "The Measurement of Observer Agreement for Categorical Data." In: *Biometrics* 33.1 (1977), p. 159.

[89] B. A. Landman et al. "Diffusion Tensor Imaging at Low SNR: Nonmonotonic behaviors of tensor contrasts." In: *Magnetic Resonance Imaging* 26.6 (2008), p. 790.

[90] J. Lätt et al. "Effects of restricted diffusion in a biological phantom: a q-space diffusion MRI study of asparagus stems at a 3T clinical scanner." In: *Magnetic Resonance Materials in Physics, Biology and Medicine* 20.4 (2007), pp. 213–222.

[91] J. Lätt et al. "Accuracy of q-space related parameters in MRI: simulations and phantom measurements." In: *IEEE Transactions on Medical Imaging* 26.11 (2007), pp. 1437–1447.

[92] D. Le Bihan et al. "MR imaging of intravoxel incoherent motions: application to diffusion and perfusion in neurologic disorders." In: *Radiology* 161.2 (1986), p. 401.

[93] P. Linse and O. Soderman. "The Validity of the Short-Gradient-Pulse Approximation in NMR Studies of Restricted Diffusion. Simulations of Molecules Diffusing between Planes, in Cylinders and Spheres." In: *Journal of Magnetic Resonance, Series A* 116.1 (1995), pp. 77–86.

[94] S. Ljunggren. "A Simple Graphical Representation of Fourier-Based Imaging Methods." In: *Journal of Magnetic Resonance* 57.54 (1983), p. 338.

[95] H. Lundell et al. "Distribution of collateral fibers in the monkey cervical spinal cord detected with diffusion-weighted magnetic resonance imaging." In: *NeuroImage* 56.3 (2011), pp. 923–929.

[96] H. Lundell et al. "Independent spinal cord atrophy measures correlate to motor and sensory deficits in individuals with spinal cord injury." In: *Spinal Cord* 49.1 (2010), pp. 70–75.

[97] C. Malmborg et al. "Mapping the intracellular fraction of water by varying the gradient pulse length in q-space diffusion MRI." In: *Journal of Magnetic Resonance* 180.2 (2006), pp. 280–285.

[98] H. Mamata et al. "Collateral nerve fibers in human spinal cord: Visualization with magnetic resonance diffusion tensor imaging." In: *NeuroImage* 31.1 (2006), pp. 24–30.

[99] P. Mansfield. "Real-time echo-planar imaging by NMR." In: *British medical bulletin* 40.2 (1984), pp. 187–190.

[100] D. Marchiano. *Medical Encyclopedia MedlinePlus. ADAM Inc*. 2005.

[101] A. E. Mautes et al. "Vascular events after spinal cord injury: contribution to secondary pathogenesis." In: *Physical therapy* 80.7 (2000), pp. 673–687.

[102] D. McRobbie et al. *MRI from Picture to Proton*. Cambridge University Press, 2002.

[103] C. Metzler-Baddeley et al. "How and how not to correct for CSF-contamination in diffusion MRI." In: *NeuroImage* 59.2 (2012), pp. 1394–1403.

[104] P. P. Mitra. "Multiple wave-vector extensions of the NMR pulsed-field-gradient spin-echo diffusion measurement." In: *Phys Rev, B Condens Matter* 51.21 (1995), pp. 15074–15078.

[105] M. Modat et al. "Fast free-form deformation using graphics processing units." In: *Computer Methods and Programs in Biomedicine* 98.3 (2010), pp. 278–284.

[106] M. Moseley et al. "Diffusion-weighted MR imaging of acute stroke: correlation with T2-weighted and magnetic susceptibility-enhanced MR imaging in cats." In: *American Journal of Neuroradiology* 11.3 (1990), pp. 423–429.

[107] R. V. Mulkern, S. J. Haker, and S. E. Maier. "On high b diffusion imaging in the human brain: ruminations and experimental insights." In: *Magnetic Resonance Imaging* 27.8 (2009), pp. 1151–1162.

[108] M. Nilsson et al. "The role of tissue microstructure and water exchange in biophysical modelling of diffusion in white matter." In: *Magnetic Resonance Materials in Physics, Biology and Medicine* (2013), pp. 1–26.

[109] M. Nilsson et al. "On the effects of a varied diffusion time in vivo: is the diffusion in white matter restricted?" In: *Magnetic Resonance Imaging* (2009).

[110] M. Nilsson et al. "The importance of axonal undulation in diffusion MR measurements: a Monte Carlo simulation study." In: *NMR in Biomedicine* (2012).

[111] T. E. O'Brien and G. M. Funk. "A Gentle Introduction to Optimal Design for Regression Models." In: *American Statistician* 57.4 (2003), pp. 265–267.

[112] H. H. Ong et al. "Indirect measurement of regional axon diameter in excised mouse spinal cord with q-space imaging: simulation and experimental studies." In: *NeuroImage* 40.4 (2008), pp. 1619–1632.

[113] H. H. Ong and F. W. Wehrli. "Assessment of axon diameter distribution in mouse spinal cord with q-space imaging." In: *International Society for Magnetic Resonance in Medicine (ISMRM)*. Vol. 19. 2012.

[114] H. H. Ong and F. W. Wehrli. "Quantifying axon diameter and intracellular volume fraction in excised mouse spinal cord with q-space imaging." In: *NeuroImage* 51.4 (2010), pp. 1360–1366.

[115] S. Ourselin et al. "Reconstructing a 3D structure from serial histological sections." In: *Image and Vision Computing* 19.1,Äì2 (2001), pp. 25–31.

[116] W. Overall and J. Pauly. "An extensible, graphical environment for pulse sequence design and simulation." In: *Proceedings of the 15th Annual Meeting of ISMRM, Berlin*. 2007, p. 1652.

[117] R. Pallini, E. Fernandez, and A. Sbriccoli. "Retrograde degeneration of corticospinal axons following transection of the spinal cord in rats." In: *Journal of neurosurgery* 68.1 (1988), pp. 124–128.

[118] E. Panagiotaki et al. "Compartment models of the diffusion MR signal in brain white matter: A taxonomy and comparison." In: *NeuroImage* 59.3 (2012), pp. 2241–2254.

[119] N. G. Papadakis et al. "Study of the effect of CSF suppression on white matter diffusion anisotropy mapping of healthy human brain." In: *Magnetic Resonance in Medicine* 48.2 (2002), pp. 394–398.

[120] O. Pasternak et al. "Free water elimination and mapping from diffusion MRI." In: *Magnetic Resonance in Medicine* 62.3 (2009), pp. 717–730.

[121] G. S. Pell et al. "Optimized clinical T2 relaxometry with a standard CPMG sequence." en. In: *Journal of Magnetic Resonance Imaging* 23.2 (2006), pp. 248–252.

[122] A. Pfefferbaum and E. V. Sullivan. "Increased brain white matter diffusivity in normal adult aging: relationship to anisotropy and partial voluming." In: *Magnetic Resonance in Medicine* 49.5 (2003), pp. 953–961.

[123] C. Pierpaoli and P. J. Basser. "Toward a quantitative assessment of diffusion anisotropy." In: *Magnetic Resonance in Medicine* 36.6 (1996), pp. 893–906.

[124] C. Pierpaoli and D. K. Jones. "Removing CSF contamination in brain DT-MRIs by using a two-compartment tensor model." In: *Proceedings of the ISMRM 12th Annual Meeting*. 2004.

[125] W. Price. "Pulsed-field gradient nuclear magnetic resonance as a tool for studying translational diffusion: Part 1. Basic theory." In: *Concepts in Magnetic Resonance* 9.5 (1998), pp. 299–336.

[126] R Core Team. *R: A Language and Environment for Statistical Computing*. ISBN 3-900051-07-0. R Foundation for Statistical Computing. Vienna, Austria, 2012.

[127] T. Reese et al. "Reduction of eddy-current-induced distortion in diffusion MRI using a twice-refocused spin echo." In: *Magnetic Resonance in Medicine* 49.1 (2003), pp. 177–182.

[128] G. Rohde et al. "Comprehensive approach for correction of motion and distortion in diffusion-weighted MRI." In: *Magnetic Resonance in Medicine* 51.1 (2003), pp. 103–114.

[129] E. D. Schwartz and D. B. Hackney. "Diffusion-weighted MRI and the evaluation of spinal cord axonal integrity following injury and treatment." In: *Experimental Neurology* 184.2 (2003), pp. 570–589.

[130] E. D. Schwartz et al. "MRI diffusion coefficients in spinal cord correlate with axon morphometry." In: *Neuroreport* (2005).

[131] E. D. Schwartz et al. "Spinal cord diffusion tensor imaging and fiber tracking can identify white matter tract disruption and glial scar orientation following lateral funiculotomy." In: *Journal of Neurotrauma* 22.12 (2005), pp. 1388–1398.

[132] J. P. Serra. *Image analysis and mathematical morphology*. London; New York: Academic Press, 1982.

[133] T. M. Shepherd et al. "Postmortem interval alters the water relaxation and diffusion properties of rat nervous tissue—implications for MRI studies of human autopsy samples." In: *Neuroimage* 44.3 (2009), pp. 820–826.

[134] P. E. Shrout and J. L. Fleiss. "Intraclass correlations: Uses in assessing rater reliability." In: *Psychological Bulletin* 86.2 (1979), pp. 420–428.

[135] B. Siow et al. "Estimation of pore size in a microstructure phantom using the optimised gradient waveform diffusion weighted NMR sequence." In: *Journal of Magnetic Resonance* 214 (2012), pp. 51–60.

[136] B. Siow et al. "Optimised Oscillating Gradient Diffusion MRI for the Estimation of Axon Radius in an Ex Vivo Rat Brain." In: *Proceedings 20th Scientific Meeting, International Society for Magnetic Resonance in Medicine*. 2012.

[137] S. Song et al. "Dysmyelination Revealed through MRI as Increased Radial (but Unchanged Axial) Diffusion of Water." In: *NeuroImage* 17.3 (2002), pp. 1429–1436.

[138] S. Sotiropoulos, T. Behrens, and S. Jbabdi. "Ball and rackets: Inferring fiber fanning from diffusion-weighted MRI." In: *NeuroImage* (2012).

[139] G. J. Stanisz et al. "An analytical model of restricted diffusion in bovine optic nerve." In: *Magnetic Resonance in Medicine* 37.1 (1997), pp. 103–111.

[140] G. J. Stanisz et al. "T1, T2 relaxation and magnetization transfer in tissue at 3T." en. In: *Magnetic Resonance in Medicine* 54.3 (2005), 507–512.

[141] M. K. Stehling, R. Turner, P. Mansfield, et al. "Echo-planar imaging: magnetic resonance imaging in a fraction of a second." In: *Science* 254.5028 (1991), pp. 43–50.

[142] E. O. Stejskal and J. E. Tanner. "Spin Diffusion Measurements: Spin Echoes in the Presence of a Time-Dependent Field Gradient." In: *Journal of Chemical Physics* 42 (1965), p. 288.

[143] J. Stepišnik. "Time-dependent self-diffusion by NMR spin-echo." In: *Physica B: Condensed Matter* 183.4 (1993), pp. 343–350.

[144] A. Szafer et al. "Diffusion-weighted imaging in tissues: theoretical models." In: *NMR in Biomedicine* 8.7-8 (1995), pp. 289–296.

[145] A. W. Toga et al. "Mapping the Human Connectome." In: *Neurosurgery* 71.1 (2012), pp. 1–5.

[146] M. O. Totoiu and H. S. Keirstead. "Spinal cord injury is accompanied by chronic progressive demyelination." In: *The Journal of Comparative Neurology* 486.4 (2005), pp. 373–83.

[147] J. Tournier, S. Mori, and A. Leemans. "Diffusion tensor imaging and beyond." In: *Magnetic Resonance in Medicine* 65.6 (2011), pp. 1532–1556.

[148] A. Tristán-Vega et al. "Efficient and robust nonlocal means denoising of MR data based on salient features matching." In: *Computer Methods and Programs in Biomedicine* 105.2 (2012), pp. 131–144.

[149] D. Tuch et al. "High angular resolution diffusion imaging reveals intravoxel white matter fiber heterogeneity." In: *Magnetic Resonance in Medicine* 48.4 (2002), pp. 577–582.

[150] D. B. Twieg. "The k-trajectory formulation of the NMR imaging process with applications in analysis and synthesis of imaging methods." In: *Medical Physics* 10.5 (1983), pp. 610–621.

[151] P. Van Gelderen et al. "Evaluation of Restricted Diffusion in Cylinders. Phosphocreatine in Rabbit Leg Muscle." In: *Journal of Magnetic Resonance, Series B* 103.3 (1994), pp. 255–260.

[152] S. B. Vos et al. "Partial volume effect as a hidden covariate in DTI analyses." In: *NeuroImage* 55.4 (2011), pp. 1566–1576.

[153] J. Wang et al. *robust: Insightful Robust Library*. R package version 0.3-19. 2012.

[154] Y. Wang et al. "Quantification of increased cellularity during inflammatory demyelination." In: *Brain* 134.12 (2011), pp. 3590–3601.

[155] S. Warach et al. "Fast magnetic resonance diffusion-weighted imaging of acute human stroke." In: *Neurology* 42.9 (1992), pp. 1717–1717.

[156] C. Watson, G. Paxinos, and G. Kayalioglu. *The spinal cord: a Christopher and Dana Reeve Foundation text and atlas*. Academic Press, 2009.

[157] S. G. Waxman. "Demyelination in spinal cord injury." In: *Journal of the Neurological Sciences* 91.1-2 (1989), pp. 1–14.

[158] C. A. M. Wheeler-Kingshott et al. "A new approach to structural integrity assessment based on axial and radial diffusivities." In: *Functional Neurology* (in press).

[159] C. A. M. Wheeler-Kingshott et al. "ADC mapping of the human optic nerve: increased resolution, coverage, and reliability with CSF-suppressed ZOOM-EPI." In: *Magnetic Resonance in Medicine* 47.1 (2002), pp. 24–31.

[160] C. A. M. Wheeler-Kingshott et al. "Investigating Cervical Spinal Cord Structure Using Axial Diffusion Tensor Imaging." In: *NeuroImage* 16.1 (2002), pp. 93–102.

[161] B. Wilm et al. "Reduced field-of-view MRI using outer volume suppression for spinal cord diffusion imaging." In: *Magnetic Resonance in Medicine* 57.3 (2007), pp. 625–630.

[162] M. E. Wolak, D. J. Fairbairn, and Y. R. Paulsen. "Guidelines for Estimating Repeatability." In: *Methods in Ecology and Evolution* (2011).

[163] K. Yamada et al. "Detection of early neuronal damage in CADASIL patients by q-space MR imaging." In: *Neuroradiology* (2012), pp. 1–8.

[164] C.-H. Yeh et al. "The effect of finite diffusion gradient pulse duration on fibre orientation estimation in diffusion MRI." In: *NeuroImage* 51.2 (2010), pp. 743–751.

[165] I. Zelinka. *Evolutionary Algorithms and Chaotic Systems (Studies in Computational Intelligence)*. Springer, 2010.

[166] H. Zhang, T. Dyrby, and D. Alexander. "Axon diameter mapping in crossing fibers with diffusion MRI." In: *Medical Image Computing and Computer-Assisted Intervention* (2011), pp. 82–89.

[167] H. Zhang et al. "Axon diameter mapping in the presence of orientation dispersion with diffusion MRI." In: *NeuroImage* 56.3 (2011), pp. 1301–1315.

[168] H. Zhang et al. "A comparative study of axon diameter imaging techniques using diffusion MRI." In: International Society of Magnetic Resonance in Medicine. 2011.

[169] H. Zhang et al. "NODDI: Practical *in vivo* neurite orientation dispersion and density imaging of the human brain." In: *NeuroImage* (2012).

[170] J. Zhang et al. "Diffusion tensor magnetic resonance imaging of Wallerian degeneration in rat spinal cord after dorsal root axotomy." In: *The Journal of Neuroscience* 29.10 (2009), pp. 3160–71.